Modified Source-Type Flame Model and Vorticity Generated by the Flame and Bluff Bodies

by

Shiung-po Kao

Dissertation submitted to the Faculty of the

Virginia Polytechnic Institute and State University

in partial fulfillment of the requirements for the degree of

Doctor of Philosophy

in

Aerospace and Ocean Engineering

APPROVED:

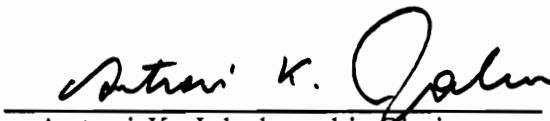

Antoni K. Jakubowski, Chairman

Walter F. O'Brien

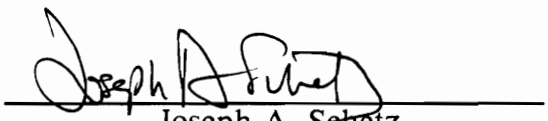

Joseph A. Schetz

Bernard Grossman

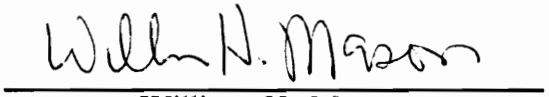

William H. Mason

May, 1991

Blacksburg, Virginia

Modified Source-Type Flame Model and Vorticity Generated by the Flame and Bluff Bodies

by

Shiung-po Kao

Antoni K. Jakubowski, Chairman

Aerospace and Ocean Engineering

(ABSTRACT)

A numerical model is developed to simulate the wrinkled laminar flame sheet flapping in weakly turbulent premixed combustion. The wrinkled laminar flame sheet is represented by a discrete distribution of volume sources called source disks. These source disks are utilized to produce the acceleration of combustion products behind the flame sheet. The laminar flame speed is allowed to vary according to flame stretch. A modified source model is proposed against the background of the existing source model's physically unrealistic symmetric expansion in both the upstream and the downstream directions. This flame model also includes flame-generated vorticity which is associated with the increasing entropy intrinsic to any system going through an irreversible process. The flame-generated vorticity is treated as discrete vortex disks. Vorticity created on the surface of the flame holder is computed with the vortex sheet method and diffuses into the surrounding flow in the form of vortex disks. The freestream turbulence is simulated by injecting vortex disks into an initially uniform freestream.

Flame-flow interactions are studied when a thin circular cylinder, a large circular cylinder, and a flat plate normal to freestream are used as flame holders. Results show that the modified source model gives more accurate prediction of flame angle than the existing source model does, the relative errors can be reduced by as much as four times. The modified source model also produces velocity profiles closer to those found in experiment, the deviations are cut by half at most sampling points in the flow. The vorticity shed from a thin circular cylinder flame stabilizer is found to only influence downstream regions very close to the cylinder. The eddy shedding behind a bluff body flame holder is suppressed in reacting flow simulations and the computed recirculating zone in a reacting flow is nearly half as long as that in a cold flow. When the relative size of the flame holder is one order of magnitude larger than the thickness of flame sheet, the vorticity shed by the flame holder can no longer be neglected. Flame wrinkling and flame extinction caused by vortical fluid motion behind the flame holder are found through numerical simulation.

Acknowledgements

This work can not have been accomplished without the advice and support so amply given by Dr. Jakubowski. To him goes my deepest gratitude. Thanks should be extended to Dr. Pindera who offered enlightening discussion several times. I am also grateful to my family who have endured hard times.

Table of Contents

List of Illustrations

List of Tables

INTRODUCTION

Premixed turbulent flames are found in many practical applications such as internal combustion engines, Bunsen-type burners, fuel-jet ejector burners, and airbreathing engines. In airbreathing engines, combustion flow fields frequently contain both diffusion flame regions and premixed or mostly premixed flame regions. The latter are typically associated with recirculation/ flame stabilization regions which can be obtained by placing solid obstacles in the stream (ramjet combustors, afterburners); by using backward-facing steps or cavities (dump combustors); or by directing the flow of one of the reactants opposed or normal to the main stream (gas turbine combustion chambers). Premixed flames have been studied since late 19th century when Mallard and Le Chartier noted the apparent differences between premixed laminar and premixed turbulent flames in 1883. They recorded that for the same reactant supply rate a laminar flame cone on a Bunsen burner was higher than a turbulent flame cone and the turbulent flame zone appeared to be thicker. Since a lower cone of the same base pre-

sents less frontal surface area relative to the supply flow, they deduced that a turbulent flame consumed more reactant in unit time than a laminar flame did. The above deduction also led to a notion that 'turbulent flame speed' is higher than the laminar flame speed of the same reactant mixture with the identical thermodynamic state and composition. We shall avoid using the term 'turbulent flame speed' because it is not a property of the reactant mixture as the laminar flame speed is, hence such a term may be misleading. Instead, the normal mass flux of reactants divided by density of reactants entering the turbulent flame front is called turbulent burning velocity. Damkohler(1940) tried to explain the effect of turbulence on burning velocity in premixed turbulent flames by proposing that in weakly turbulent flows the thick flame zone, called 'flame brush', is made up of a rapidly oscillating continuous wrinkled laminar flame sheet (Fig.1). Thus there is increased surface area A_3 for reaction per unit frontal area A_2 of the flame brush and hence a higher consumption rate of reactants. A conventional way to define turbulent burning velocity S_T is $S_T = U_\infty A_1/A_2 = U_\infty \sin\theta_f$, where θ_f is the flame angle. Schlieren photographic evidence for the existence of wrinkled laminar flame sheets in premixed turbulent combustion is abundant (Karlovitz, Denniston, Jr., and Wells 1951; Wohl et al. 1953; Fox and Weinberg 1962; Ballal and LeFebvre 1975; Tsuji 1979). In weakly turbulent flows where the r.m.s. velocity fluctuation is less than 5% , a continuous wrinkled sheet is found (e.g. Rajan, Smith, and Rambach 1984; Smith and Gouldin 1979; Dandekar and Gouldin 1982). In flows with stronger turbulence, the continuous wrinkled sheet is fragmented into numerous nearly semi-circlar curves.

More recently, conditional LDV sampling (Cheng and Ng 1983, Dandekar and Gouldin 1984, Driscoll and Gulati 1988, Namazian 1987, Suzuki et al. 1986, Yoshida 1986 etc.) of premixed flames in weakly turbulent flows showed bimodal velocity distribution with two distinct peaks corresponding to slow-moving reactants and faster-moving products. Such a result was expected, because a clearly defined oscillating flame boundary will situate the LDV probe volume intermittently in reactants or products. Bill, Jr., et al. (1982) made conditional sampling of density and also found bimodal distribution with peaks corresponding to the light, heated products and the heavier reactants. This very intermittency associated with thin flame sheet is also central to the well-known flame model developed by Bray, Moss, and Libby (e.g. Libby and Bray 1980). Ion probes were also used (e.g. Yoshida and Tsuji 1984) to identify the passage of a thin flame sheet by the brief surges in the ion current registered.

Gross and Esch (1954) were first to treat a planar laminar flame sheet as a surface of discontinuity represented by a source sheet when studying a 2-D premixed V flame stabilized by a thin rod in a steady flow. A V flame derives its name from the fact that the two flame brushes attatched to the thin rod are like the two arms of the letter V. The effect of a source sheet is to create enough extra volume to accommodate the expansion of combustion products due to heating. They were aware of the fact shown by Tsien (1951) that flame will produce vorticity whether the approach flow is irrotational or not. They chose to ignore such flame vorticity on the ground that no solution technique was available to solve the problem. Uberoi, Kuethe, and Menkes (1958) also made use of the source-sheet model to

study premixed Bunsen flames within confinements. They made qualitative analysis and reached the conclusion that there could be no solution to the problem unless the laminar flame speed is allowed to vary along the flame front. Again, there was no solution technique to account for variable laminar flame speed. Treating laminar flame speed as a constant, Uberoi later studied flames stabilized in a channel.

Karlovitz et al. (1951) and Markstein (1964) pioneered the study of variable laminar flame speed based on flame stretch rate and flame curvature respectively. Clavin and Williams (1982) brought these two approaches together and presented a description of variable laminar flame speed depending on stretch rate of the flame front. This significant advance made it possible to find a solution for a flame simulated by a source line (a source sheet viewed from its side in 2-D). Recent experimental work (Deshaies and Cambray 1990) has shown that Clavin's theoretical prediction is very accurate.

Tsien studied the problem of vorticity generation by flame and presented his results in terms of thermodynamic properties. Truesdell (1954), Lighthill (1958), and Emmons (1958) all worked on this problem. Finally, Hayes (1959) presented a relationship between vorticity produced by flame and kinematic quantities at the flame front. Thus, Hayes' results are suitable to be utilized in a flame model which calculates only the flow field and displacement of flame sheets but not thermodynamic propertities.

In order to make such a flame model work, one must be able to find the subsequent motion of the vorticity produced by flames. Rosenhead (1932) introduced a method for analyzing the motion of vortex sheets in which a vortex sheet is approximated by an array of point vortices. Takami (1964) and Moore (1971) have shown that point vortices can produce arbitrarily large errors. To improve on the convergence, Chorin and Bernard (1973) introduced circular vortices of finite core size and called them 'vortex blobs'. He also simulated the viscous diffusion effect by adding a random displacement to the convective motion of each vortex disk (we have changed 'blob' to disk for its circular shape), hence the name random vortex method. This method was applied (Chorin 1973) to study viscous flows past a circular cylinder in which vortex disks were generated near the surface of the cylinder. Later, vortex sheets were proposed to replace vortex disks near a solid boundary and flow over a flat plate was studied (Chorin 1978). Cheer (1983) studied flow past a circular cylinder with a method using both vortex disks and vortex sheets. Ghoniem, Chorin, and Oppenheim (1982) presented a numerical simulation of a 2-D reacting premixed flow past a backward-facing step inside a rectangular combustion chamber. In the above work, the expansion due to combustion was simulated by a source model. Recently, Sod (1987) showed a study of compressible turbulent flows using an expanded version of random vortex method. Convergence of random vortex method has been studied by many, among them are Hald (1979), Ghoniem and Cagnon (1987), and Ghoniem and Sethian (1988).

Pindera and Talbot (1986) employed the source model to simulate thermal expansion of combustion, Hayes' formulation to find the vorticity produced by the flame, and random vortex method to track the motion of flame-generated vorticity to simulate the 2-D V-shape premixed turbulent flame studied by Cheng (1984). Vorticity generated by the circular cylinder which served as flame holder was ignored in their simulation.

The flame-holder-generated vorticity had been speculated to exert influence on the flame-flow interaction (Bill, Jr., et al. 1982, Dandekar and Gouldin 1982). The studies of bluff-body flame holders(e.g., Williams et al. 1949, Ballal and Lefebvre 1979) showed that flame stabilization is dependent on the recirculation zone behind a bluff body. Roshko (1954, 1988) showed that the recirculation zones behind bluff bodies are related to vorticity generated on the surface of bluff bodies. Therefore, to obtain an improved simulation, the flame-holder-generated vorticity will have to be included. Furthermore, while the omission of boundary condition on the surface of the flame holder makes calculating the motion of vortices simpler, it also deletes the only solid boundary in the flow configuration. As we all know, boundary conditions are the entities which distinguish different problems governed by the same type of differential equations. Thus, we expect that it is indispensable to impose boundary conditions on the V-flame simulation or else the problem statement is not complete.

Another problem of the existing source-type flame model pointed out by Ashurst (1987) is that the predicted flame angle is at least twice as large as the measured

angle even for a relatively simple geometry like the open V flames (Cheng 1984). We expect that the discrepancy between the computed and the measured flame angles is due to an overestimate of the speed at which the local flame front moves upstream into the reactants. Such an overestimate may be caused by the symmetric discharge velocity on both sides of a source line in a 2-D plane. Since the hot products of a thin flame sheet do not actually expand symmetrically in both the upstream and the downstream directions, a symmetric source line will offer more deceleration to the approaching reactants than an actual flame will offer. For two laminar flame sheets with identical flame speeds, the sheet facing a slower approach flow will propagate more into the upstream direction and extend a larger flame angle. Based upon the above reasoning, we therefore propose an unsymmetric-strength source model which allocates less expansion on the upstream (reactant) side than on the downstream (product) side of a laminar flame sheet.

Our main objectives are:

1. Show that the existing source model for flame sheets (for example, Gross and Esch 1954; Ghoniem 1985; Ashurst 1987; Pindera and Talbot 1988) can be improved by modifying the source representation to account for differential expansions in front and behind a flame sheet. The proposed modification should result in a model which is physically more realistic than the existing one, especially the computed flame angle.

2. Develop a flame model including the vorticity generated by a circular cylinder which stabilizes the flame. Then find out whether a simulation including flame-holder vorticity yields better agreement with experiment than the previous open V flame simulations (e.g. Pindera and Talbot 1988) which showed discrepancies in both computed magnitudes and trends of velocity profiles near the axis of symmetry.

3. Make numerical observations of the flame-flow interaction in regions close to a circular cylinder flame holder. Attention is directed to the formation of large scale structures and their role in the initial wrinkling of flame sheets, especially when freestream turbulence is not simulated by the injection of random vortices.

4. Both cold and reacting flows past a flat plate normal to the free stream will be simulated numerically. Drag coefficient of the flat plate in cold flows will be calculated. Computations will be performed to identify the wrinkling and the extinction of laminar flame sheet in the near wake of the flat plate.

THEORY AND NUMERICAL FORMULATION

2.1 Outline

The main assumptions for the source-type flame model in this work are stated below.

1. The flow is two-dimensional.

2. The flow velocity is small compared with the speed of sound and thus is regarded as incompressible on both sides of the flame.

3. The flame acts as an interface moving at a specified normal speed S_L with respect to the reactants (Fig.1). The speed S_L is dependent upon local flame stretching.

4. The entire flow field is divided into two regions (Fig.1) : reactant region, upstream of the flame; and product region, downstream of the flame. The reactant and the product regions have , respectively, uniform density ρ_R, ρ_P and temperature T_R, T_P. We have $\rho_R > \rho_P$ and $T_R < T_P$ due to the heating and volume expansion from combustion.

5. The flame does not experience viscous effects.

Assumption 3 allows for a simplified problem by not treating the details of chemistry and thermodynamics within the reaction zone. Nevertheless, the inclusion of a variable laminar flame speed S_L carries the effects of chemistry and thermodynamics into the problem in an implicit manner. Assumption 5 is based on Matalon and Matkowsky's (1982) study of vorticity generated by flames and their findings that viscosity is negligible when the ratio of laminar flame thickness to the characteristic length scale of the approach flow is small. For the various flames considered in our study the above ratio is less than 10^{-3}.

Because of assumption 4, the region upstream of the flame and that downstream of the flame are both without discontinuity and any vector field (in this case, velocity $\vec{U}$) defined in these regions can be decomposed into three distinct parts (Batchelor 1967) as shown in Fig.2 when adapted to this current work :

a) irrotational and incompressible, $\vec{W}_1$

b) irrotational but compressible, $\vec{W}_2$ due to source disks

c) incompressible but rotational, $\vec{W}_3$ due to vortex disks

or

$$\vec{U} = \vec{W}_1 + \vec{W}_2 + \vec{W}_3.$$

Letting $\varepsilon(\vec{x})$ and $\vec{\omega}(\vec{x})$ represent respectively the volume expansion and the vorticity field, $\vec{U}$ is required to satisfy the conditions

$$\nabla \cdot \vec{U} = \varepsilon(\vec{x}),$$

$$\nabla \times \vec{U} = \vec{\omega}(\vec{x}). \tag{2.1}$$

The parts $\vec{W}_1$, $\vec{W}_2$, and $\vec{W}_3$ are identified as

$$\nabla\zeta = \vec{W}_1 \quad , \quad \nabla^2\zeta = 0 \quad ; \tag{2.2}$$

$$\nabla \cdot \vec{W}_2 = \varepsilon(\vec{x}) \quad , \quad \nabla \times \vec{W}_2 = 0 \quad ; \tag{2.3}$$

$$\nabla \times \vec{W}_3 = \vec{\omega}(\vec{x}) \quad , \quad \nabla \cdot \vec{W}_3 = 0 \quad ; \tag{2.4}$$

where $\nabla = (\frac{\partial}{\partial x}, \frac{\partial}{\partial y})$ and $\nabla^2 = \frac{\partial^2}{\partial x^2} + \frac{\partial^2}{\partial y^2}$. When combustion occurs at low Mach numbers, ε vanishes everywhere except at the flamefront and hence may be represented by a delta function $m\delta(\vec{x}_f - \vec{x})$ where m is the strength of a source line and will be determined by the amount of volume expansion due to combustion. As mentioned before, these sources of volume are employed to simulate the volume expansion associated with the temperature rise of combustion. The flow may be called 'slightly compressible' in the sense that the volume expansion

is manifested at the reaction zone only. The Laplace's equation (i.e. eq.(2.2)) is solved subject to appropriate boundary conditions; the resulting velocity $\vec{W}_1$ is taken to represent the noncombusting potential flow past a circular cylinder.

The velocity fields $\vec{W}_2$ and $\vec{W}_3$ are obtained by using the technique of transforming eqs. (2.3-4) into Poisson's equations. To this end, let ψ and $\vec{B}$ represent a scalar and a vector potential respectively such that

$$\nabla\psi = \vec{W}_2 \ , \tag{2.5}$$

$$\nabla \times \vec{B} = \vec{W}_3 \ . \tag{2.6}$$

Then eqs. (2.3) and (2.5) yield

$$\nabla^2\psi = m\delta(\vec{x}_f - \vec{x}) \ , \tag{2.7}$$

and from Eqs. (2.4) and (2.6), with the assumption that $\nabla \bullet \vec{B} = 0$ everywhere, one obtains

$$\nabla^2\vec{B} = -\vec{\omega} \ . \tag{2.8}$$

The restriction on the vector potential, $\nabla \bullet \vec{B} = 0$, can be shown to be equivalent to the requirement for $\vec{\omega} \bullet \hat{n}$ to vanish on the solid boundary of the flow. For simple geometries this boundary condition can be satisfied by techniques like the method of images in potential flow theory (e.g. Milne-Thomson 1968). For mod-

erately complex geometries, fast Poisson solvers can be utilized as discussed by Ghoniem (1987).

The Poisson eqs. (2.7-8) can be solved using the method of Green's functions. In a two-dimensional field the appropriate solutions are :

$$\vec{W}_2(\vec{x}_i) = \frac{1}{2\pi} \int_A \frac{\varepsilon(\vec{x}_j)\vec{r}}{r^2} \, dA(\vec{x}_j) \quad ,$$

$$\vec{W}_3(\vec{x}_i) = \frac{1}{2\pi} \int_A \frac{\vec{r} \times \vec{\omega}(\vec{x}_j)}{r^2} \, dA(\vec{x}_j) \quad ,$$

where $\vec{r} = \vec{x}_i - \vec{x}_j$ and A is the area over which $\varepsilon(\vec{x}_j)$ or $\vec{\omega}(\vec{x}_j)$ is defined. With the aid of the delta representation for the volume expansion term ε, the above equations are cast into the final forms

$$\vec{W}_2(\vec{x}_i) = \frac{1}{2\pi} \int_C \frac{m\vec{r}}{r^2} \, dl(\vec{x}_f) \quad , \tag{2.9}$$

$$\vec{W}_3(\vec{x}_i) = \frac{1}{2\pi} \int_A \frac{\omega}{r^2} [- (y_i - y_j)\hat{i} + (x_i - x_j)\hat{j}] \, dA(\vec{x}_j) \quad , \tag{2.10}$$

where C is a curve formed by all points $\vec{x}_f$, i.e. the flame front. Since the prerequisite for the above decomposition is the absence of discontinuity, it may seem improper to apply this decomposition to our problem where a surface of discon-

tinuity exists as a flame sheet. However, this decomposition is to be applied, respectively, to the two regions divided by the flame but not on the flame.

Equations (2.9) and (2.10) together with the solution for $\vec{W}_1$, completely describe the flow field for any given $m(\vec{x}_f)$ and $\omega(\vec{x})$.

As will be developed in the following sections, the volume expansion $m(\vec{x}_f)$ can be related to source disks which approximate straight segments of source line which, in turn, simulate the flame sheet; and $\omega(\vec{x})$ can be determined from the vorticity transport equation. The vorticity transport equation is treated by the random vortex method, details of this method will be given later. Since the vorticity transport equation is obtained by taking the curl of the momentum equation, away from the flame $\nabla \times \nabla P = 0$, and the pressure fields will not explicitly enter into the formulation of the problem.

With these restrictions in mind and the limitation that we only deal with wrinkled laminar flames, the three parts of the decomposed velocity field will be developed. $\vec{W}_1$ is a potential representation of the cold background flow, $\vec{W}_2$ is computed with a source-disk model, $\vec{W}_3$ with the random vortex method.

2.2 *The Background Flow*

In principle, the background flow is a potential flow which satisfies the no-flux boundary condition on solid boundaries in the flow field. Since the effects of a 2-D circular rod flame stabilizer will be studied, let us use this flow configuration to exemplify the principle. For a circular cylinder immersed in a 2-D uniform approach flow, the velocity components at any point outside or on the cylinder are

$$\vec{W}_1 = u_1 \hat{i} + v_1 \hat{j} \quad ,$$

$$u_1 = U_\infty (1 - \frac{R^2(x^2 - y^2)}{(x^2 + y^2)^2}) \quad ,$$

$$v_1 = - U_\infty (\frac{2xyR^2}{(x^2 + y^2)^2}) \quad . \tag{2.11}$$

where R is the radius of the cylinder, the x direction points to right, the y direction points downwards (Fig.3).

2.3 Flame Front Modeled by Source Disks

2.3.1 Background

Under the condition of fast chemical reaction, flames can be regarded as a thin region of intense chemical activity. Zeldovich and Frank-Kamenetskii (1938) first indicated that with an Arrhenius formulation for chemical reaction rate , rate $\propto$ exp(-E/kT), the reaction zone thickness tends to zero as the activation energy E tends to infinity. As reviewed by Bray (1980), such a thin zone is approximated by an infinitely thin surface in many flame models. Bray also mentioned other assumptions: the pressure fluctuations are neglected, the Mach number is small and hence the flow is incompressible, and combustion is characterized by a single-step irreversible chemical reaction taking place at a constant rate. His assumptions about pressure and Mach number are also enlisted in our flame model. The assumption of constant reaction rate is relaxed by allowing variable laminar flame speed in our model. It was accepted that (e.g. Bray 1980, Williams 1984, Borghi 1984) the existence of thin laminar flame sheets requires that the laminar flame speed be smaller than the r.m.s. turbulent velocity fluctuation and the Kolmogorov length scale be greater than the thickness of preheat zone. Both conditions are met by numerous V flames studied experimentally. More recently, Abdel-Gayed, Bradley, and Lung (1989) showed that continuous wrinkled laminar flame sheets could exist when r.m.s. turbulent velocity fluctu-

ation is less than or equal to 5 S_L. Thus the application of a flame model based on wrinkled laminar flame sheet may be broader than previously thought. Darrieus (1938) and Landau (1944) were first to treat thin flames as an interface separating two fluids of different densities and moving at a constant speed. They both found the flames unconditionally unstable to any perturbation. This behavior is called hydro-dynamic instability : its mechanism is explained very well by Emmons (1958). Briefly, wrinkled flame sheets (Fig.4) present troughs and crests to approach flow, and the fluid velocity increases at the troughs while decreases at the crests. If the flame speed is constant, at the troughs the flame will be convected downstream, while at the crests the flame will move upstream thus increasing the wrinkles and amplifying the instability.

Since stable flames do exist, Markstein (1964) reasoned that the laminar flame speed must vary along a flame front. He proposed to modify the flame speed by introducing dependence on the local flame curvature R_f in the form

$$S_L = S_U(1 + \frac{\Lambda}{R_f}) \quad , \quad \Lambda = \kappa d \quad ; \tag{2.12}$$

where S_U is the laminar flame speed, S_L is the laminar flame speed influenced by curvature, Λ is a characteristic length scale which depends on the preheat zone thickness d, and κ represents the effects of transport of energy and species. Once the sign of R_f is chosen, as shown in Fig. 4, the flame speed at the crest would decrease, while that at the trough would increase. Both of them tend to stabilize the flame.

Karlovitz et al. (1953), on the other hand, concluded that for combustion in the presence of velocity gradients the local value of S_L must reflect the effects of 'flame stretch' induced by the local velocity gradients. The stretch K was defined as the rate of change per unit local flame surface area, for the steady two-dimensional flame they considered

$$K = \frac{1}{A}\frac{dA}{dt} = \frac{\partial U_T}{\partial t} \quad , \tag{2.13}$$

where U_T is the component of $\vec{U}$ tangent to local flame front. The authors expressed this dependence in terms of velocity gradients with respect to stationary coordinates, and since their analysis was confined to flames nearly parallel to the flow , they did not make the connection between stretch and velocity gradients for general conditions.

Since the early eighties, Matalon and Matkowsky (1982) , Clavin and Joulin (1983) , and Chung and Law(1984) have combined the ideas of Markstein and Karlovitz. Chung and Law summarized the discussion with a vector derivation for K of a steady flame observed by a stationary observer,

$$K = \nabla_T \bullet U_T \quad , \tag{2.14}$$

where the term on the right denotes the tangential gradient of tangential velocity along the flame front. From the results of Matalon and Matkowsky, and Clavin and Joulin one may write

$$S_L = S_U(1 - \frac{\Lambda K}{S_U}) \quad . \tag{2.15}$$

The above equation has been verified most recently by Deshaies and Cambray (1990) with experiment. The parameter Λ, now denoted as the Markstein length scale was deduced to be

$$\Lambda = d[\frac{v}{v-1} \ln v + \frac{\beta(Le-1)}{2(v-1)} \int_0^{v-1} \frac{\ln(1+x)}{x} dx] \quad . \tag{2.16}$$

In the above equation, Le is the Lewis number and v is the density ratio of reactants to products, d is the thickness of flame sheet, and β is a function of activation energy and combustion product temperature. Since we assume $Le = 1$, eq. (2.16) becomes

$$\Lambda = d\frac{v}{v-1} \ln v \quad . \tag{2.17}$$

With experimental confirmation of the existence of wrinkled laminar flame sheets within weakly turbulent reacting flow and the theoretical means to account for the variation of laminar flame speed along the flame front, the next logical step in developing a flame model which simulates flame by a source line is to develop a mathematical model to describe the flow field induced by the source line.

For simplicity, suppose the flame sheet of length $\sum_{i=1}^{N} L_i$ is composed of a number of N straight line segments, each segment in turn is taken as made up of the

cross-section of a source sheet with uniform strength over the segment. Consider then a straight line segment of length L with output flux m. Referring to the geometry of Fig. 5, for any point P($\vec{x}_0$) and a source element of strength mdl/L lying at point Q(l) on the line segment when Q is at a distance r from P, the velocity at P is given by

$$\vec{W}_2(\vec{x}_0) = \frac{mdl}{2\pi rL}\left(\frac{\vec{r}}{r}\right) \quad . \tag{2.18}$$

The total velocity at point P is a sum of contributions from all the source segments, and hence

$$\vec{W}_2(\vec{x}_0) = \frac{1}{2\pi L}\int_0^L m\frac{(l)}{r}\left(\hat{t}\cos\theta + \hat{n}\sin\theta\right) dl \quad , \tag{2.19}$$

where $\hat{t}$ and $\hat{n}$ are local unit vectors in the tangential and normal directions respectively(Fig.5). When m is constant, the velocity components become

$$W_{2T} = \frac{m}{2\pi L}\ln\left(\frac{r_1}{r_2}\right) \quad , \tag{2.20}$$

$$W_{2N} = \frac{m}{2\pi L}\left(\theta_2 - \theta_1\right) \quad , \tag{2.21}$$

the parameters r_1, r_2, θ_1, and θ_2 being defined in Fig. 5.

When a source line is used to model a wrinkled flame sheet, the velocity field induced by this source line is expressed as eq. (2.9). To carry out the integration

of eq. (2.9) numerically this source line is discretized into a finite number of N straight flame segments of length L and strength m. But such a discretization alone can not render a numerical integration feasible. The reason is that at the ends of a source segment, $r_1 = 0$ and $r_2 = 0$, we will encounter difficulties with the logarithmic terms in eq. (2.21). When $r_1 = 0$, the natural log is not defined; when $r_2 = 0$ the argument for natural log is infinite. To overcome the above difficulties, each segment is then treated as a finite circular source 'disk' of radius σ_s and of strength m. Such a source disk may be viewed as the cross-section of a line source being spread over an area, thus a source disk is a function defined on a small but finite region while the cross-section of a line source is singular at a point. We will determine m, σ_s, and u_s later when we propose a new model for source strength.

It is usually assumed that the radial velocity inside the disk is constant. Then integral (2.9) can be approximated by the following sum (i.e., applying eq. 2.19 to all flame segments) to give the velocity $\vec{W}_1$ at any point (x_i, y_i) due to N source disks at (x_j, y_j)

$$\vec{W}_2(x_i, y_i) = \frac{1}{2\pi} \sum_{1}^{N} \frac{m_j}{\max(\sigma_{sj}, r_j)} (\hat{i} \cos\theta + \hat{j} \sin\theta) \quad , \tag{2.22}$$

where θ is measured from the X-axis and r_j is the distance from the center of a source disk. The denominator is so chosen as to treat any point within the source disk as if the point was on the circumference of the disk and the singularity of a

point source is removed. This discretization becomes exact in the limit $N \to \infty$, $L \to 0$, otherwise it gives errors of $O((L/r_j)^2)$, where r_j is the distance from the flamefront (i.e. the source disks).

To facilitate numerical calculation eq. (2.22) is rewritten in terms of velocity components u_2 and v_2

$$u_2(x_i, y_i) = \frac{1}{2\pi} \sum_{1}^{N} m_j \frac{x_i - x_j}{(\max(\sigma_{sj}, r_j))r_j} \quad ,$$

$$v_2(x_i, y_i) = \frac{1}{2\pi} \sum_{1}^{N} m_j \frac{y_i - y_j}{(\max(\sigma_{sj}, r_j))r_j} \quad . \tag{2.23}$$

The above expressions are only valid for flow regions without solid boundary.

When solid boundaries are present in the flow field, a system of images is needed to satisfy the condition that no fluid should flow through these boundaries. Let us consider the circular cylinder in Fig.(3). Milne-Thomson (1968) shows that when a point source of strength m is located at P(x, y) outside the cylinder, its image system comprises of two elements : one is a sink of $-m$ at the center of the cylinder; the other is a source m at the inverse point (x', y') whose coordinates are defined as

$$x' = \frac{R^2 x}{x^2 + y^2} \quad ,$$

$$y' = \frac{R^2 y}{x^2 + y^2} \quad . \tag{2.24}$$

Thus the velocity components at (x_i, y_i) induced by all source disks at (x_j, y_j) and their images are given by

$$u_2(x_i, y_i) = \frac{1}{2\pi} \sum_1^N m_j \left[\frac{x_i - x_j}{(\max(\sigma_{sj}, r_{ij}))r_{ij}} + \frac{x_i - x'_j}{(\max(\sigma_{sj}, r'_{ij}))r'_{ij}} - \frac{x_i}{r^2_i} \right] ,$$

$$v_2(x_i, y_i) = \frac{1}{2\pi} \sum_1^N m_j \left[\frac{y_i - y_j}{(\max(\sigma_{sj}, r_{ij}))r_{ij}} + \frac{y_i - y'_j}{(\max(\sigma_{sj}, r'_{ij}))r'_{ij}} - \frac{y_i}{r^2_i} \right] . \tag{2.25}$$

2.3.2 A Modified Source Model

The current method for determining source strength m is to evaluate eq. (2.21) at the flamefront where $\theta_1 = 0$ and $\theta_2 = \pi$

$$W_{2_N}|_{flame} = \frac{m}{2L} = u_s \quad ,$$

and impose the condition that the volume discharged by the source line must account for the volume expansion due to heating. A key assumption is that the discharge velocity u_s is constant along a segment of source line and symmetric on both sides of a line segment (Fig. 6). Since volume is inversely proportional to density we can write, for unit mass of reactants and products

$$V_P = \frac{\rho_R}{\rho_P} V_R \quad ,$$

where V is volume, ρ is density, subscripts P and R represents products and reactants respectively. The volume expansion is

$$V_P - V_R = (\frac{\rho_R}{\rho_P} - 1)V_R \quad .$$

Since the flame speed is constant along a given elemental flamefront, one can also write the volume rate of reactants consumed by flame as

$$V_R = LS_L \quad .$$

Taking $v = \rho_R/\rho_P$,

$$m = V_P - V_R = (v-1)LS_L \quad ,$$

$$\frac{m}{2L} = u_s = \frac{(v-1)S_L}{2} \quad ,$$

and the last step follows from the jump condition of conservation of mass. Gross and Esch (1954) used a similar formula for the strength of source. The form shown here was first presented by Ghoniem et al.(1982), however the present derivation is different. One implication of the existing source model is that the strength of a source line is symmetric on both sides of the line. When this existing source model is employed to simulate a flame sheet located in a steady flow, the approach flow will be decelerated by u_s on reaching the flame sheet and will be

accelerated by u_s on leaving the flame sheet. Although the net velocity jump across the flame sheet complies with the requirement of conservation of mass coupled with the lower density of hot combustion products, the real physics suggested by experience is far from the mathematical description of the existing source model. In many experiments (e.g. Cheng 1984, Driscoll and Gulati 1988, Gouldin and Dandekar 1984) the component of the approach flow normal to the flame sheet remains almost constant or is decelerated much less than what the existing source model predicts. Therefore, a re-allocation of total source strength on the two sides of a source line segment is necessary. Since the presence of a flame is indeed felt upstream as well as downstream, we exclude the choice of assigning all source strengths to the downstream side.

Based on the earlier assumption of ideal gas, one can express the specific volume expansion as

$$V_P - V_R = \frac{R_R T_R}{P_R} - \frac{R_P T_P}{P_P}$$

for a fluid element flowing through the flame sheet, T_P is the product temperature, T_R is the reactant temperature. R_R and R_P are gas constants for the reactants and the products respectively. R_R and R_P are different because chemical reaction brings changes in composition of this system of fixed mass. An approximation for low hydrocarbon fuel and air is to use the gas constant of air R_g for both reactants and products. With a fixed R_g and the fact that the pressure drop across a flame sheet $(P_R - P_P)/P_R$ is of $O(10^{-3})$, one can write

$$V_P - V_R = C_1(T_P - T_R)$$

and

$$V_P/V_R = T_P/T_R \quad ,$$

where C_1 is a constant. Thus, in in principle, the temperature profile across a laminar flame sheet can provide an estimate of specific volume expansion at different locations along the element's path as the fluid element approaches and travels through the flame sheet. The temperature at which the exothermic reaction begins to contribute more to the temperature rise than heat transfer does is designated T_i and is often taken to be the beginning of the reaction zone. Then the ratio $r_i = T_i/T_P$ indicates the ratio of the specific volume expansion taking place before the reaction zone to that taking place across the reaction zone. Therefore, $r_i(T_P/T_R - 1)S_L$ can be allocated to the upstream side of a source line as its strength of discharge. While the volume expansion $(1 - r_i)(T_P/T_R)S_L$ can be assigned to the downstream side of the source line. In the above manner, the discharge velocities u_{s1} and u_{s2} for upstream and downstream sides respectively are given as

$$u_{s1} = 2r_i u_s \quad ,$$

$$u_{s2} = 2(1 - r_i)u_s \quad .$$

Note that the total discharge still satisfies the requirement of volume expansion derived before, namely

$$2r_i u_s L + 2(1 - r_i)u_s L = 2u_s L \quad .$$

The concept of the modified source model is illustrated in Fig.7 and a value of $r_i = 0.25$ is given to present the concept in a specific sense. For a simpler geometry, the radius of a source disk in this modified model (Fig. 7) is given by $\sigma_s = L/\pi$ to satisfy

$$2u_s L = 2r_i u_s \pi\sigma_s + 2(1 - r_i)u_s \pi\sigma_s = 2\pi\sigma_s u_s \quad .$$

A practical difficulty in implementing the modified source model is that the exact value of T_i is often disputed and varies from flame to flame. The approach taken in this work is to compare the velocity profiles computed by using $r_i = 0.00$, 0.10 , 0.25 with the measured profiles and select the value which gives the best fit to experiment. The comparison described above will be presented in Results and Discussion. The application of this modified source model to the simulation of flame is dependent on whether the point where the source-induced velocity is calculated is upstream or downstream of the source disk concerned. For reasons to be explained later in 2.3.4, we will locate source disks at the midpoint of every flame segment, a scanning process is done to find the flame segment bounded by (x_{f_n}, y_{f_n}) and $(x_{f_{n+1}}, y_{f_{n+1}})$ such that $x_{f_n} \leq x \leq x_{f_{n+1}}$ for a given point (x, y). Then tests are run to determine whether (x, y) is located upstream or downstream of the above flame segment. For a continuous wrinkled flame

sheet which can be described by a single-valued function of x or y, a point located upstream of any flame segment is taken to be located upstream of the entire flame sheet. The current scheme is limited to wrinkled flame sheets which do not intersect twice both with a line normal to the x-axis and a line normal to the y-axis. The following rules are formulated for the simulation of a symmetric V flame.

For a point on the flame front, a source strength of $u_s L$ is used when calculating the source-induced velocity at this point. The two arrows (Fig. 7) parallel to the source segment show the above situation. A point on the flame front has the ambiguity of being on the upstream side and the downstream side at the same time. The users of the existing source model also have to tackle the above ambiguity when computing the tangential velocity at the flame front. The usual scheme is to take the average of the upstream and the downstream values. The current rule is formulated in the same light

$$(2r_i u_s + 2(1 - r_i)u_s)/2 = u_s \quad .$$

Any point in region 1 (Fig. 8) is considered upstream of flame sheet A and downstream of flame B. All points in region 2 are treated as downstream of both flame sheets. Every point in region 3 is dealt with as upstream of flame sheet B and downstream of flame sheet A.

With the above rules in mind, appropriate strength m_j can be replaced into eqs.(2.25).

2.3.3 Vorticity Generation by Flame

The logarithmicaly growing tangential velocity indicated by eq.(2.24) will generate considerable vorticity at the flame front. Tsien (1951) has shown that in general, the flow of combustion products is rotational even when the approach reactant flow is irrotational. He began his derivation with Crocco's theorem and reached a conclusion involving thermodynamic properties. Since then, many researchers have studied this subject. Truesdell (1952), Lighthill (1957), Uberoi (1958), and Emmons (1958) studied steady two-dimensional flows. The complete three-dimensional solution for unsteady flow was given by Hayes (1959). Hayes presented his results in terms of velocities which can be evaluated along the flamefront and hence easily fitted into the current flame model where kinematic quantities are calculated.

Consider a flame with a constant burning speed relative to the reactants. For steady flow the jump in vorticity across the flame is

$$\Delta\omega = \frac{v-1}{v}\frac{U_T}{S_L}\frac{\partial U_T}{\partial t} \quad . \tag{2.26}$$

It might seem contradictory to an earlier discussion on variable flame speed along the flamefront to employ a vorticity generation expression based on constant flame speed. The seeming contradiction just mentioned is one of the reasons why the flame sheet is broken into many straight flame segments in source-type flame models. To navigate around this contradiction, eq. (2.26) applies only to each

straight flame segment. While the flame speed varies from segment to segment, it remains constant on each segment. This is not the real mechanism but only an approximation. The approximation is improved as the number of flame segments is increased. Eq.(2.26) can be related to flame stretch through eq. (2.14)

$$K = \nabla_T \bullet U_T - \frac{V_N}{R_1} \quad .$$

For steady two-dimensional flow, $K = \dfrac{\partial U_T}{\partial t}$ ($V_N = 0$ since it is measured with respect to a lab-fixed system) and eq. (2.26) becomes

$$\Delta\omega = \frac{v-1}{vS_L} KU_T \quad , \tag{2.27}$$

where U_T is the tangential component of $\vec{U}$ evaluated at mid-point of a flame segment. For unit depth of a flame segment, area ratios can be represented by length ratios and we can write

$$K = \frac{1}{{}_nL} \frac{{}_{n+1}L - {}_nL}{\Delta t} \quad , \tag{2.28}$$

where the subscripts denote time steps. The above expressions can show some insight about the effects of modeling flame with segments of source line. Using eq. (2.21), one obtains the amount of stretch, due to discharge of source only, at point Q on a source line by taking W_{1_T} as U_T

$$K = \frac{v-1}{2\pi} \frac{S_L L}{l(L-l)} \quad , \tag{2.29}$$

and the related vorticity production is

$$\Delta\omega = \frac{(v-1)^3}{(2\pi)^2}\frac{S_L}{v}\frac{L}{l(L-l)}\ln\left(\frac{l}{L-l}\right) \quad . \tag{2.30}$$

Eqs.(2.29-30) show that since the 'source-induced' stretch is always positive, the sign of the resultant induced vorticity takes on the sign of the tangential velocity. In a right-handed system , positive vorticity induces counter-clockwise fluid motion. In the coordinate system defined in Fig. 3, positive vorticity requires clockwise fluid motion.

Eq.(2.26) also shows sudden jump in vorticity which violates the continuity assumption which allows $\vec{U}$ to be decomposed into $\vec{W}_1$, $\vec{W}_2$, and $\vec{W}_3$. To overcome this, a vortex disk must be added into the flow behind every flame segment. The entire flow region is thus divided into two subregions (e.g. the reactant and the product regions in Fig.1) both allowing the decomposition of $\vec{U}$. The circulation of this flame- generated vortex disk is

$$\Delta\Gamma_f = (\Delta\gamma)vS_L\Delta t = (v-1)U_T KL\Delta t \quad . \tag{2.31}$$

The area of a disk is given by

$$\Delta A = vS_L\Delta t \quad ,$$

which is equivalent to an area swept by flame segment's length L over a distance $vS_L\Delta t$, where vS_L is the normal velocity behind the flame. Assuming the disk to be circular, its radius is simply

$$\sigma = \left(\frac{\Delta A}{\pi}\right)^{1/2}.$$

These flame vortices are added to the product flow during every time step to become a part of all the vortices in the flow, and their subsequent motion is calculated with the random vortex method to be introduced in Sec. 2.4.

2.3.4 Flame Motion and Source Models

One of the fundamental assumptions of this and all source-type flame models is that flame motion is comprised of convection and propagation, where the latter reflects the conversion of reactants into products. The situation is often regarded as analogous to the Huygens' principle in optics (e.g. Gaydon and Wolfhard 1979). Although this idea was introduced rather early (Damkohler, 1940) in the study of turbulent premixed flames, there had not been any direct quantitative evidence to support it until Suzuki et al. (1986) presented their work. They used ion probes and LDA to measure simultaneously local flamefront movement and flow velocity at the same spot. By subtracting local flow velocity from the overall flame movement they showed that local flamefronts moved nearly at the laminar flame speed relative to local flow. However, care still needs to be taken when specifying the speed of the flame elements during the calculations. The real crux

of this problem is how to treat the source-induced flow velocity moving away from a flame segment against the approaching reactant flow when modeling flamefronts with source disks. For the existing source model, there have been two ways to account for the flame speed relative to the flow. Karasalo (1982) and Rotman (1986) put source disks behind flame segments and let the flame move at a speed S_L normal to the local flame front (Fig. 9a). The local reactant flow approaches the flame front at a normal speed $U_N - u_s$, ie. the free stream is retarded by source discharge u_s. For a stationary observer, the absolute flame speed normal to the flame front is $(U_N - u_s) - S_L$.

On the other hand, Sethian (1982) and Ashurst (1987) put the center of a source disk at the mid-point of a flame segment and specify that the flame move at a speed $S_L + u_s$ (Fig.9b). In the above configuration, the reactants approach at U_N while not being retarded by the source discharge. The absolute speed of flame becomes $U_N - (S_L + u_s)$.

The above two expressions for absolute flame speed are equal as far as algebraic results are concerned. However, the physical implications are different. The expression which Karasalo et al. and Rotman used means that a flame moves at speed S_L into reactants flowing at $U_N - u_s$ normal to the flame. The expression adopted by Sethian and Ashurst implies that the flame moves at the speed $S_L + u_s$ into reactants flowing at U_N normal to the flame. A conceptual difficulty is presented by the latter expression because this expression implies that the relative speed between the flame and the fluid is now $S_L + u_s$. The above speed is

inconsistent with the cardinal assumption in all source-type flame models (Ghoniem, Oppenheim, and Chorin 1982) that the flame propagates as a wave at S_L relative to the fluid. The problem can be demonstrated by the following brief derivation. If the flame moves at $S_L + u_s$ relative to the reactants, then the discharge velocity of a line source will become

$$u'_s = \frac{(v-1)(S_L + u_s)}{2} = \frac{[(v-1) + (v-1)^2]S_L}{2}$$

when the discharge velocity u_s of the previous time step is updated by u'_s. Since

$$\frac{u'_s}{u_s} = \frac{(v-1) + (v-1)^2}{(v-1)}$$

$$= v \quad .$$

One can easily see that the computed source strength at every time step is v times as large as that of the previous step. Because the expansion ratio v is always greater than unity, the computed source strength will increase indefinitely as the solution marches in time. What is mentioned above simply can not be true. Therefore the presently accepted view point that the two methods (Figs. 9a, 9b) are equivalent is not correct. Although both ways of accounting for flame speed relative to flow produce identical numerical results, we will point out that only the source-behind-flame configuration gives the correct physical interpretation. Because the source-at-midpoint configuration gives itself to easier formulation during programing, eq.(2.32) is treated as if the sources were at the midpoints of

flame segment. Yet, we should keep in mind that the correct physical interpretation is the configuration where source disks are located behind flame segments. When compared with our unsymmetric source model, both existing expressions overestimate the absolute flame speed by $2r_i u_s$. The implication of our model is that the flame moves at speed S_L, normal to the flame front, into reactants approaching at speed U_N computed with our model. The U_N computed with our model is higher than that computed with the existing model by $2r_i u_s$, hence our absolute flame speed is lower than the existing model by $2r_i u_s$ and a smaller flame angle is expected.

From the foregoing considerations, the flame speed $\vec{V}$ measured with respect to stationary coordinates can be in general represented by

$$\frac{\partial \vec{x}_f}{\partial t} = \vec{V} \tag{2.32}$$

$$= -(S_L + 2r_i u_s)\hat{n} + \vec{W}_1(\vec{x}_f) + \vec{W}_2(\vec{x}_f) + \vec{W}_3(\vec{x}_f) \quad .$$

To move the flame interface the 'surface tracking method' (Hyman 1984) was chosen since information of the flamefront geometry can be directly extracted. Thus, at the end of time step n, a flame at ${}_n\vec{x}_f$ is displaced to a new position, such that

$${}_{n+1}\vec{x}_f = {}_n\vec{x}_f + \int_{\Delta t} {}_n\vec{V}\, dt \quad . \tag{2.33}$$

Using a second-order Runge-Kutta method, the above integral is evaluated numerically. In order to find $\vec{V}$ to be used in eq.(2.33), one needs to know S_L, and $\vec{U}$. Now, S_L depends on stretch K as indicated by eq. (2.15). Furthermore, the vortical part of $\vec{U}$ (i.e., $\vec{W}_3$) is dependent upon vorticity distribution which also depends on stretch K. Since stretch is given by the rate of change of flame position, we reach the conclusion that we need information derived from (2.33) in order to solve (2.33) by numerical integration. Thus, the flame motion problem is implicit and an iterative solution is called for.

The algorithm to move the flame front is as follows.

1. Find ${}_n\vec{V}$ at all flame points. Then move flame points according to eq.(2.33) to find their new position.

2. Replace old and new flame positions into eq.(2.28) to calculate flame stretch K. With K, one goes on to find S_L and the strength of flame vortices $\Delta\Gamma_f$. Then release $\Delta\Gamma_f$ into the flow as vortex disks.

3. Use S_L and $\Delta\Gamma_f$ found in step 2, the process is brought back to step 1 and repeated untill a stable flame position is found. Experience shows that five iterations are sufficient.

The time step Δt used in the integration is automatically adjusted so that $(\Delta t)^2 \leq \frac{1}{const} \min(\frac{L}{U_T})^2$ where the minimum is determined by comparing all $(\frac{L}{U_T})^2$ computed at each flame segment. The above requirement is similar to the

Courant stability condition; in this case the value 10 was found for the constant from numerical experiments. Following the displacement of the flame points, a shape-preserving parametric (with respect to the arc length) cubic spline routine of Fritsch (1984) is used to reposition the flame points along the new flame front. When applying the spline fit, the input data are smoothed by using $\frac{1}{2}(\vec{x}_i + \vec{x}_{i+1})$ in place of any two successive points $\vec{x}_i$ and $\vec{x}_{i+1}$ for better accuracy as pointed out by Hyman(1984). The initial position of the flame sheet can be specified to be a simple straight line, for in the solution process the flame geometry will be adjusted to the flow conditions.

2.4 Random Vortex Method

2.4.1 Background

Chorin and Bernard (1973) presented the random vortex method to construct numerical solutions of the Navier-Stokes equations, and to model the development of unstable flow fields associated with the roll-up of velocity discontinuities in the form of vortex sheets. A brief outline of this method in two dimensions will follow.

The continuity and the momentum equations for 2-D incompressible flows are

$$\nabla \cdot \vec{U} = 0 \quad , \tag{2.34}$$

$$\frac{\partial \vec{U}}{\partial t} + \vec{U} \cdot \nabla \vec{U} = \frac{1}{Re} \nabla^2 \vec{U} - \nabla P \quad , \tag{2.35}$$

Re is the Reynolds number. On solid boundary

$$\vec{U} = 0 \quad , \tag{2.36}$$

at far upstream

$$\vec{U} = \vec{U}_\infty \quad . \tag{2.37}$$

In 2-D flows, the vorticity ω is a scalar

$$\omega = \frac{\partial v}{\partial x} - \frac{\partial u}{\partial y} \quad . \tag{2.38}$$

The vorticity transport equation is derived by taking the curl of eq.(2.35) and using eq.(2.34) and the identity $\nabla \times \nabla P = 0$, one obtains

$$\frac{\partial \omega}{\partial t} + \vec{U} \cdot \nabla \omega = \frac{1}{Re} \nabla^2 \omega \quad . \tag{2.39}$$

Knowing the vorticity field, the velocity can be evaluated by integrating eqs. (2.34) and (2.38), and the vorticity field can be advanced in time using eq. (2.39).

In random vortex method, distributed vorticity is lumped into a collection of discrete finite vortex elements. Then the vorticity transport process is simulated by

the motion of finite vortex elements. The vorticity transport equation is broken down into two independent parts representing convection and diffusion respectively. In doing so, it is assumed that the motion of vortex elements is made up of convective and diffusive mechanisms only and these two mechanisms are independent. The part standing for convective motion is

$$\frac{\partial \omega}{\partial t} + \vec{U} \cdot \nabla \omega = 0 \quad . \tag{2.40}$$

Each vortex element is convectively transported as a particle in the Lagrangian sense by a velocity field $\vec{U} = \vec{W}_1 + \vec{W}_2 + \vec{W}_3$. The other part is in the form of a diffusion equation

$$\frac{\partial \omega}{\partial t} = \frac{1}{Re} \nabla^2 \omega \quad . \tag{2.41}$$

The diffusion process is simulated with a random walk process according to the relationship between diffusion and random walk discussed by Einstein(1956). The above two equations are solved in tandem, thus a vortex element is first convected from its old location to an intermediate location and then displaced randomly to attain its new location.

Chorin initially tried to satisfy the boundary conditions (2.36) and (2.37) by generating vortex disks near the solid boundaries. Later (1978), he used short straight segments of vortex sheets within a thin numerical shear layer adjacent to the solid boundary. The numerical shear layer employed in vortex sheet method is of $O(Re^{-1/2})$ and has no direct physical meaning, but serves as an artifice so that

the production of vorticity, the transport of vortex sheets, and the transition between vortex sheets and vortex disks can be computed and tracked. The above transition occurs whenever a vortex sheet travels outside the numerical shear layer or a vortex disk goes inside the layer. By using vortex sheets in the numerical shear layer, the stability and convergence are improved.

The random vortex method is applied in this section to find the vortical part $\vec{W}_3$ of the decomposed velocity fheld $\vec{U}$ in the sequence of vortex induction, random walks, and boundary conditions.

2.4.2 Vortex Induction

The essence of the random vortex method is to lump a distribution of vorticity into a number of discrete vortex elements. Then the effects of vorticity is manifested by the combined Biot-Savart induction due to all vortex elements. Starting with the basic form of using 2-D vortex points as vortex elements, we can write the velocity components at point (x_i, y_i) induced by vortex points at (x_j, y_j) with circulation Γ_j as the following

$$\vec{W}_3 = u_{3_i}\hat{i} + v_{3_i}\hat{j} \quad ,$$

$$u_{3_i} = \frac{1}{2\pi}\sum \frac{y_j - y_i}{r_{ij}^2}\Gamma_j \quad ,$$

$$v_{3_i} = \frac{1}{2\pi} \sum \frac{x_j - x_i}{r_{ij}^2} \Gamma_j \quad ,$$

$$r_{ij} = ((x_j - x_i)^2 + (y_j - y_i)^2)^{1/2} \quad . \tag{2.42}$$

The sign conventions of u_{3_i} and v_{3_i} are opposite to those in a right-hand system in order to match the coordinate system depicted in Fig.3.

Since a vortex point has a singularity at its center where the induced velocity is infinite, the above formulation will result in numerical instability. Chorin and Bernard (1973) proposed to use a circular disk with a finite radius σ and a constant tangential velocity along the radius such that $2\pi u_e \sigma = \Gamma$. In other words, u_e is the tangential velocity at the edge of a vortex disk and it remains constant from the edge to the center of a vortex disk and this vortex is said to have a constant 'core function'. Very sophisticated core functions are available (Beale and Majda 1985)

, however, Ghoniem (1987) concluded that the simplest constant core function usually gave good solutions to backward facing step combustors and the shear layer between two parallel streams of different speeds.

When vortex disks of finite radii are used, the induced velocity is given by

$$u_{3_i} = \frac{1}{2\pi} \sum \frac{y_j - y_i}{(\max(\sigma_j, r_{ij}))r_{ij}} \quad , v_{3_i} = \frac{1}{2\pi} \sum \frac{x_j - x_i}{(\max(\sigma_j, r_{ij}))r_{ij}} \quad , \qquad (2.43)$$

where σ_j is the radius of vortex disk j, and r_{ij} is defined as in eq. (2.42).

The denominator is designed to treat any point within σ_j as if it was on the edge of vortex disk j.

For a flame model which does not consider the influence of vorticity produced by the flame holder, eqs. (2.11), (2.24), and (2.43) give $\vec{U}$ to be used in eqs. (2.32). Then the motion of source disks can be determined by numerically integrating eq.(2.33). To include the effects of the flame holder, one must treat the boundary conditions.

2.4.3 Random Walks

When there is no solid boundary in the flow field, eqs.(2.11),(2.24),and (2.43) also describe the convective motion of all vortices (i.e. vortex disks). However, convection is not the only transport mechanism for a vortex disk. The transport of vorticity due to diffusion is expressed by eq.(2.41). Note that the Green function of the 1-D form of (2.41) is

$$G(y,t) = \sqrt{Re/4\pi t}\ \exp(\frac{-Re}{4t}y^2) \quad . \tag{2.44}$$

This is identical to the probability density function of a Gaussian random variable η with a zero mean and a standard deviation σ_G

$$\mathbb{P}(\eta,t) = \sqrt{1/2\pi\sigma_G}\ \exp(-\frac{1}{2\sigma_G}\eta^2) \quad , \tag{2.45}$$

if $\sigma_G = \sqrt{2t/Re}$ and t is the time elapsed since the initial condition. In random vortex method, t should be replaced by the step size Δt and $\sigma_G = \sqrt{2\Delta t/Re}$. In two dimensions, the Green function of (2.41) is

$$G(x,y,\Delta t) = \frac{Re}{4\pi\Delta t}\exp(-\frac{Re}{4\Delta t}(x^2,y^2)) \quad , \tag{2.46}$$

which is equivalent to

$$G(x,y,\Delta t) = G(x,\Delta t)G(y,\Delta t) \quad , \tag{2.47}$$

where $G(x,\Delta t)$ and $G(y,\Delta t)$ have the same form as in (2.44). The corresponding probability density function is the product of two 1-D probability density functions

$$\mathbb{P}(\eta_x,\eta_y;\Delta t) = \mathbb{P}_1(\eta_x;\Delta t)\mathbb{P}_2(\eta_y;\Delta t) \quad .$$

Thus the solution to eq.(2.47) is simulated by a 2-D displacement of the vortex elements in two perpendicular directions using two sets of independent Gaussian

random numbers, each having zero mean and a standard deviation $(2\Delta t/Re)^{1/2}$. If no solid boundaries exist, the displacement due to the convective mechanism of transport is given by the Heun method

$$ {}_{n+1}x_i^0 = {}_nx_i + [{}_nU_x(x_i^0, y_i^0) + {}_nU_x(x_i, y_i)]\frac{1}{2}\Delta T \quad , $$

$$ {}_{n+1}y_i^0 = {}_ny_i + [{}_nU_y(x_i^0, y_i^0) + {}_nU_y(x_i, y_i)]\frac{1}{2}\Delta T \quad , $$

$$ x_i^0 = {}_nx_i + {}_nU_x(x_i, y_i)\Delta T \quad , $$

$$ y_i^0 = {}_ny_i + {}_nU_y(x_i, y_i)\Delta T \quad . $$

The final displacement is obtained by adding random walks to the above to yield

$$ {}_{n+1}x_i = {}_{n+1}x_i^0 + \eta_{x_i} \quad , $$

$$ {}_{n+1}y_i = {}_{n+1}y_i^0 + \eta_{y_i} \quad . \tag{2.48} $$

For V-flame problem without solid boundaries, U_x and U_y are given by

$$ U_x = U_\infty\left(1 - \frac{R^2(x^2 - y^2)}{(x^2 + y^2)^2}\right) + \frac{1}{2\pi}\sum_1^N m_j \frac{x_i - x_j}{(\max(\sigma_{sj}, r_j))r_{ij}} + \frac{1}{2\pi}\sum_1^{NV} \frac{\Gamma_j(y_j - y_i)}{(\max(\sigma_j, r_{ij}))r_{ij}} \quad , $$

$$U_y = -U_\infty\left(\frac{2xyR^2}{(x^2+y^2)^2}\right) + \frac{1}{2\pi}\sum_1^N m_j \frac{y_i - y_j}{(\max(\sigma_{sj}, r_j))r_{ij}} + \frac{1}{2\pi}\sum_1^{NV} \frac{\Gamma_j(x_j - x_i)}{(\max(\sigma_j, r_{ij}))r_{ij}} \quad , \quad (2.49)$$

where σ_{sj} denotes the radius of a source disk, σ_j the radius of a vortex disk, and NV is the number of flame vortices in the flow.

2.4.4 Boundary Conditions

When solid boundaries are present in a flow field, two boundary conditions should be satisfied on these boundaries. The first is that no fluid can flow through a solid boundary. This no-flux condition can be fulfilled by a system of images. Let us refer again to the circular cylinder in Fig. 3. Milne-Thomson (1968) gives that the image system of a vortex Γ at (x, y) outside the cylinder is made up of two vortices: a vortex Γ at the center of the cylinder; and a vortex $-\Gamma$ at the inverse point defined by eqs.(2.25). The vortex Γ and its inverse image $-\Gamma$ will cancel exactly their contributions to normal velocity on the surface. The image at the center is needed to preserve the total circulation around the cylinder.

With all images included, the induced velocity field due to a set of vortices becomes

$$u_{3_i} = \frac{1}{2\pi} \sum \Gamma_j \left[\frac{y_j - y_i}{(\max(\sigma_j, r_{ij}))r_{ij}} - \frac{y'_j - y_i}{(\max(\sigma_j, r'_{ij}))r_{ij}} - \frac{y_i}{(\max(\sigma_j, r_i))r_i} \right],$$

$$v_{3_i} = \frac{1}{2\pi} \sum \Gamma_j \left[\frac{x_j - x_i}{(\max(\sigma_j, r_{ij}))r_{ij}} - \frac{x'_j - x_i}{(\max(\sigma_j, r'_{ij}))r_{ij}} - \frac{x_i}{(\max(\sigma_j, r_i))r_i} \right],$$

$$r_i = (x_i^2 + y_i^2)^{1/2},$$

$$r'_{ij} = ((x'_j - x_i)^2 + (y'_j - y_i)^2)^{1/2},$$

where x' and y' are defined in (2.25); σ_j is the radius of vortex disk j; and r_{ij} is defined in (2.42). Those three terms within brackets represent, respectively, the inductions due to: vortex j; the inverse image of j; and the center image of j. The above equations describe a flow field which meets the normal boundary condition on the surface of a circular cylinder. When applied to the flow-past-circular cylinder problem, these equations can be simplified (Cheer 1983) as

$$u_{3_i} = \frac{1}{2\pi} \sum \Gamma_j \left[\frac{y_j - y_i}{(\max(\sigma_j, r_{ij}))r_{ij}} - \frac{y'_j - y_i}{(\max(\sigma_j, r'_{ij}))r'_{ij}} \right],$$

$$v_{3_i} = \frac{1}{2\pi} \sum \Gamma_j \left[\frac{x_j - x_i}{(\max(\sigma_j, r_{ij}))r_{ij}} - \frac{x'_j - x_i}{(\max(\sigma_j, r'_{ij}))r'_{ij}} \right]. \tag{2.50}$$

Next we will tackle the no-slip boundary condition.

We can apply eqs.(2.11), and (2.50) to find the total velocity $\vec{U}$ at any point on the surface of a circular cylinder. This velocity field will not meet the no-slip condition. To reduce the velocity to zero across the thin numerical shear layer adjacent to the surface, a number of vortex elements are introduced within this layer. These vortex elements are stacked at different distances from the surface like a deck of cards (Fig.10). When an observer goes from the top card to the bottom card, he will experience a velocity jump on crossing every card. The accumulated velocity jump is designed to bring the freestream to a halt on the solid boundary and thus satisfy the no-slip boundary condition. Vortex disks were used at first, they were later replaced by short linear segments of vortex sheets. Chorin (1978) presented a detailed explanation of the vortex sheet method, however, we can only go over the essential elements here.

If x is taken to be a direction tangent to the wall and y the one normal to it, the following conditions are known to prevail in the shear layer immediately adjacent to the wall (Schlichting 1968):

1. Boundary layer approximation

$$\frac{\partial v}{\partial x} \ll \frac{\partial u}{\partial y} \quad ; \tag{2.51}$$

2. Diffusion in the x direction is negligibly small in comparison with convection in this direction.

As a consequence of the boundary layer approximation (2.51), the vorticity ω at any point within the layer is given by

$$\omega = -\frac{\partial u}{\partial y} .$$

One can integrate from the edge of the shear layer at x_i to a point (x_i, y_i) between the edge and the wall and obtain

$$u_\delta(x_i) - u(x_i, y_i) = -\int_{y_i}^{\delta_s} \omega \, dy \quad , \tag{2.52}$$

where $u_\delta = U_T$ at $y = \delta_s$.

The integral in (2.52) can be transformed into a summation by partitioning the value of ω along y and defining the circulation per unit length of a vortex sheet as

$$\gamma_j = \lim_{\Delta y \to 0} \int_{y_j}^{y_j + \Delta y} \omega \, dy \quad , \tag{2.53}$$

for $y_i \leq y_j \leq \delta_s$. If the solid boundary is divided into equal segments of length h, then each vortex sheet also has length h and its circulation Γ_j is

$$\Gamma_j = h \, \gamma_j \quad , \tag{2.54}$$

and the velocity jump between the upper and lower surfaces of this vortex sheet is

$$\Delta u_j = \gamma_j \quad . \tag{2.55}$$

The physical significance of eq.(2.52) is to restrict the zone of influence of a vortex sheet to the vertically-hatched 'shadow' directly below it (Fig.11a). Thus a vortex sheet receives induction only from those sheets which are located above it and casting an overlapping projection on it. The intensity of influence is proportional to the amount of overlapping. Therefore the velocity of a vortex sheet centered at (x_i, y_i) with length h is induced by all influence-bearing sheets to be

$$u(x_i, y_i) = u_\delta(x_i) - \sum_{+} \gamma_j d_j \quad ,$$

$$d_j = 1 - |x_i - x_j|/h \quad ,$$

$$u_\delta(x_i) = U_\infty\left(1 - \frac{R^2(x_i^2 - y_i^2)}{(x_i^2 + y_i^2)^2}\right) + \frac{1}{2\pi}\sum \Gamma_i\left[\frac{y_i}{(\max(\sigma_i, r_i))r_i} - \frac{y'_i}{(\max(\sigma_i, r'_i))r'_i}\right] \quad ,$$

$$r'_i = (x'^2 + y'^2)^{1/2}, \tag{2.56}$$

where $\sum_{+}$ is done over all $y_j > y_i$, and σ_i is the radius of a vortex disk. The value of v is found through integrating

$$v = -\frac{\partial}{\partial x}\int_0^{y_i} u\,dy \tag{2.57}$$

by using $u(x_i, y_i)$ as evaluated from (2.56). For this integration, we introduce

$$I = \int_0^{y_i} u\,dy = u_\delta(x_i)y_i - \int_0^{y_i} y\,du$$

$$= u_\delta(x_i)y_i - \sum \gamma_j d_j y_j \tag{2.58}$$

where du is discretized to be $\Delta u = \gamma_j d_j$. In finite-difference form, eq.(2.57) becomes

$$v_i = -(I^+ - I^-)/h \quad ,$$

$$I^\pm = u_\delta(x_i \pm \frac{1}{2}h)y_i - \sum y_{\min}\gamma_j d_j^\pm \quad ,$$

$$d_j^\pm = 1 - |x_i \pm \frac{h}{2} - x_j|/h \quad , \tag{2.59}$$

where $y_{\min} = \min(y_i, y_j)$.

This vortex sheet method will be presented and illustrated by the flow-past-circular cylinder simulation in Appendix A. In the above mentioned simulation, vortex sheets are used inside the numerical shear layer and vortex disks outside

the layer. The reason for choosing this method is to simulate the vorticity generation on the surface of the circular rod used for flame holding.

2.5 *The Combined Flame-Cylinder Problem*

The essence of theory and algorithm for simulating a uniform approach flow past a circular cylinder is presented in Appendix A. Flame-generated vorticity, approach-flow vorticity, and source disks altogether determine the vorticity production in the numerical shear layer. The vorticity produced in the numerical shear layer will travel outside the layer and become mingled with the flame-generated and the approach-flow vorticity. All vorticity from different origins and source disks mutually influence each other's motion. In other words, the motion of any source disk is determined by all other source disks and vortex disks. The above described problem is called the 'combined flame-cylinder problem'.

The solution process for the combined flame-cylinder problem is to use full versions of eqs. (2.11),(2.26), and (2.50) to compute $\vec{U}$ and u_δ. $\vec{U}$ is then applied to compute vorticity generation by flame (eq. 2.31), flame motion (eq. 2.33), and vortex motion (eq. 2.48). The slip velocity u_δ is used to find the vorticity production on the surface of the cylinder and the motion of vortex sheets(A.1) within the numerical shear layer. However, there is a major obstacle to such a solution, very high cost.

The mutual interaction among vortices in the random vortex method is pairwise, thus the time required to compute such interaction is proportional to the square of the number of vortices. Let us refer to the flame motion problem with vorticity generation (both by flame and by cylinder) as the mean-flame problem. In the mean-flame problem N (the number of flame segments) vortices are added to the flow at every time step and the total number grows very rapidly. To overcome this difficulty, a grid system is designed to form finer cells near the flame and coarser cells far from the flame (Fig.12). On each cell, all vortices of the same sense of circulation are combined into one vortex disk in keeping with the following conservation laws :

$$\Gamma = \sum_i \Gamma_i \ ,$$

$$X = \frac{1}{\Gamma} \sum_i x_i \Gamma_i \ ,$$

$$Y = \frac{1}{\Gamma} \sum_i y_i \Gamma_i \ ,$$

$$D^2 = \frac{1}{\Gamma} \sum_i \Gamma_i [(x_i - X)^2 + (y_i - Y)^2] \ .$$

where Γ, (X,Y), and D are respectively the circulation, the position, and the diameter of the resultant vortex. The grid is of finite extent however, and any vortices falling outside of it are removed from the calculation. The mean-flame problem's algorithm also makes use of the symmetry of the flow, only the right half of a V flame is modeled. After such expediencies to save time, a mean-flame problem with about 200 vortices takes 15 minutes CPU time on IBM 3090 to reach a stable solution. When we deal with fluctuating flame front instead of mean-flame front, the required CPU time multiplies. The numerical simulation of fluctuating flame front shall be explained in the following section.

When the cylinder algorithm is combined with the flame algorithm, four issues stand out to further complicate the matter.

1. The step size Δt_c for a stable cylinder problem solution is $3 \sim 5$ % of Δt of the mean-flame problem. Thus, the cost is 20 fold if we do the combined problem with step size Δt_c to preserve the stability of the overall solution.

2. We need to take into account the additional image vortices inside the cylinder whether they are produced by the flame or the cylinder to meet the no-flux condition on the solid boundary. Hence the number of vortices involved is doubled and the cost is quadrupled even if the cylinder did not produce any vortex on its surface. Now, the cost is about 100 times that of the mean-flame problem.

3. The cylinder does generate vortices to satisfy no-slip condition, and we can not combine them on a grid system the same way as we can the flame vortices. The reason is that we must have a fine resolution of discrete vorticity distribution near the cylinder to ensure a proper vortex sheet production which gives stable simulations. Numerical trials show that 400 vortices near the cylinder are necessary for a stable simulation producing computed drag coefficient within 10% of the measured values, thus the cost increases again by a factor of 9 to become 900 times that of the mean-flame problem.

4. The symmetry of flow field can not be exploited in a region near the cylinder. This is also related to a realistic simulation of the cylinder problem in the context that large scale structures (Roshko 1976) such as recirculating eddies may be formed by the numerical process. Roshko(1953,1954) studied the turbulent wake of bluff bodies extensively and showed that when a splitter plate is placed on the center line of the wake, the vortex shedding was no longer observed. He hence concluded that the formation of recirculating eddies are dependent upon the mutual induction between vorticity shed from the upper and lower separation points. Therefore a numerical simulation of flow past a circular cylinder can not utilize the symmetry of the flow field lest the mutual induction is not modeled. Thus the cost doubles what found in (3) above. The final estimate is nearly 1800 times as much as a mean-flame simulation.

Our compromise is to treat, within a certain region $\mathbb{R}$, the flow-past-cylinder problem without such expediencies as symmetry or vortex combination on a grid. Eqs. (2.56) are employed to find slip velocity and vorticity generation on the surface of cylinder, eqs.(A.1) to move vortex sheets, and (2.48) and (A.2) to move vortex disks. The criterion for this region $\mathbb{R}$ is deduced from numerical experiments to be five radii downstream of the center of the cylinder for this is the minimum distance in which both shedding and forming of eddies can be observed. Thus, a major physical feature of the flow is simulated. Then, all the cylinder-generated vortices which travel beyond region $\mathbb{R}$ are assigned to the arrays of flame-generated vortices and treated accordingly. That is they are subject to combination on grid systems and are transported convectively according to eq.(2.48). Note that the cylinder algorithm uses the radius of cylinder as length scale while the flame algorithm uses the diameter of reactant supply pipe as length scale. Therefore when a cylinder vortex $(x_c, y_c, \sigma_c, \Gamma_c)$ is handed over to be listed among the flame vortices $(x_f, y_f, \sigma_f, \Gamma_f)$ we must do the following conversions :

$$x_f = x_c F_1$$

$$y_f = y_c F_1$$

$$\sigma_f = \sigma_c F_1$$

$$\Gamma_f = \Gamma_c F_1 F_2$$

where F_1 = cylinder length scale/ flame length scale, and F_2 = cylinder velocity scale/ flame velocity scale.

Now we will treat the difference in time step size. If the flame algorithm and the cylinder algorithm have the same time step size, then these two algorithms can be marched independently using the principle of fractional steps just as the convection and diffusion mechanisms are marched using fractional steps in random vortex method. Thus, the problem reduces to finding how many steps the cylinder algorithm should be marched so that the accumulated steps will cover the same nondimensional time as one step of the flame algorithm. To begin with, the largest integer NR in the ratio $\frac{\Delta t}{\Delta t_c}$ is found and the cylinder algorithm is marched NR times with step size Δt_c. Then, the cylinder algorithm is marched one more step with step size $\Delta t - \Delta t_c NR$. In this manner, the cylinder algorithm will catch up with the flame algorithm after the former marches $NR + 1$ steps described above. During each of the $NR + 1$ steps, all cylinder vortices are checked to see if they travel beyond the five radii criterion. Those which go beyond the criterion are handed over to join the flame vortices and subject to combination on a grid system to keep down the total number of vortices.

2.6 *Flat Plate Normal to Stream*

As mentioned before, the application of Random Vortex Method requires a potential solution of the flow of interest to produce a slip velocity. The amount of vorticity generated on the boundary is, in turn, determined by the slip velocity. The flow field of a uniform free stream over a flat plate normal to the stream can be obtained from that of a uniform free stream over a circular cylinder through a Joukowski transformation of the form

$$Z = \zeta - \frac{R^2}{\zeta} \quad , \tag{2.60}$$

where the cylinder is in ζ plane and the plate is in Z plane. Both ζ and Z are complex numbers.

The velocity components q_x and q_y in Z plane are related to u and v in ζ plane as follows

$$q_x - iq_y = \frac{u - iv}{\frac{dZ}{d\zeta}} \quad . \tag{2.61}$$

Therefore, in principle, the random vortex method can be applied to simulate the flow field of a uniform free stream past a flat plate normal to the stream in the Z plane. Another approach is to solve a modified problem in the ζ plane where a uniform free stream flows over a circular cylinder and then map the solutions

into the Z plane. However, the motion of vortices can not be correctly mapped by a direct application of eq.(2.60) alone. Routh had indicated that a vortex Γ at point ζ_1 in ζ plane moving along path s will be mapped into an vortex Γ at Z_1 in the Z plane, but the vortex at Z_1 will not trace the image of path s. To find the correct path the Z plane, one needs a correction term while solving for path s in the ζ plane. The necessary correction is given in Routh theorem (Milne-Thomson 1968) as follows.

$$F'(\zeta_1) = F(\zeta_1) + \frac{\Gamma}{4\pi} \ln \left| \frac{dZ}{d\zeta} \right|_{\zeta_1} . \tag{2.62}$$

F' is the corrected complex potential after a conformal mapping, F is the potential before a conformal mapping. $\left| \frac{dZ}{d\zeta} \right|_{\zeta_1}$ is the absolute value of $\frac{dZ}{d\zeta}$ at point ζ_1.

In order to apply the conformal mapping of eq.(2.60), one can proceed to treat the correction term in Routh theorem as follows. Let $\zeta = re^{i\theta}$, then

$$d\frac{Z}{d\zeta} = 1 + \frac{R^2}{\zeta^2}$$

$$= 1 + \frac{R^2}{r^2}(\cos 2\theta - i \sin 2\theta) .$$

Replace the above into eq.(2.62), one has

$$\frac{\Gamma}{4\pi} \ln \left| \frac{dZ}{d\zeta} \right| = -\frac{\Gamma}{8\pi} \ln(1 + \frac{2R^2}{r^2} \cos 2\theta + \frac{R^4}{r^4}) .$$

In polar coordinates, the contributions due to the correction term are

$$u_r = -\frac{\Gamma}{2\pi}\frac{R^2}{r^3}\frac{1+\dfrac{R^2}{r^2}}{1+\dfrac{2R^2}{r^2}\cos\ 2\theta+\dfrac{R^4}{r^4}}\ ,$$

$$u_\theta = -\frac{\Gamma}{2\pi}\frac{R^2}{r^3}\frac{\sin\ 2\theta}{1+\dfrac{2R^2}{r^2}\cos\ 2\theta+\dfrac{R^4}{r^4}}\ .$$

The above polar components can be transformed into rectangular components by

$$u = u_r \cos\theta - u_\theta \sin\theta\ ,$$

$$v = u_r \sin\theta + u_\theta \cos\theta\ .$$

RESULTS AND DISCUSSION

3.1 Nonreacting Flow Past a Circular Cylinder

The main thrust of this work is to study some of the fundamental fluid mechanical effects on laminar flame sheets due to vorticity shed from a circular rod flame stabilizer. Therefore a simulation of 2-D stream over a circular cylinder is necessary. The computation is nondimensionalized by using the freestream velocity and the radius of the cylinder as the velocity scale and the length scale respectively. The parameters for simulating the flow past a circular cylinder are so chosen as to yield computed drag coefficients within ten percent of the experimental values. The circumference of the cylinder is divided into 20 segments (Appendix A). The step size in time is 0.2, and the maximum strength of each vortex sheet is set to be 1. The first case attempted is a flow with a Reynolds' number of 300. A series of Eulerian descriptions of the flow field at fixed sampl-

ing points about the cylinder are shown in Fig. 13 at time T = 2, 5, 8, and 11 respectively. The same flow is also depicted in Fig. 14 by showing the velocity vectors at points where individual vortices are located. When the simulation begins, there is no existing vorticity in the flow. At the end of the first time step, vorticity generated on the surface of the cylinder is represented by a number of vortex sheets to satisfy no-slip condition on this solid boundary. The above vortex sheets and those generated in subsequent time steps will diffuse away from the surface and eventually move outside the numerical shear layer by the process of random walks normal to the surface. When a vortex sheet leaves the numerical shear layer, the vortex sheet is transformed into a vortex disk and its subsequent motion is computed with the random vortex method. At time T = 2, some vortex disks are present near both shoulders of the cylinder. At time T = 5, the existing vortices seem to gather themselves into two eddies and reverse flow can be seen to exist in the region between the eddies. At time T = 8, both eddies have grown in size while the bottom one appears to be larger than the top one. At time T = 11, the bottom eddy has departed from the cylinder and the top one is no longer discernible in the space above the bottom eddy. A new eddy is forming up in a region about one diameter downstream of the top shoulder. Note that the eddy which has departed and the new eddy in formation are reminiscent to the alternate shedding of a vortex street, i.e. they are of opposite senses of rotation. Since a stochastic process of random walk is involved in computing the motion of individual vortices, it is worthwhile to observe how stochasticity affects the general features of the simulated flow. Another flow simulation with identical numerical

parameters is presented in Fig. 15 and Fig.16, which show the flow at the fixed sampling points and at where the vortices are located, respectively. Note that in the above two figures the top eddy is more prominent at time T = 11. This is contrary to what happens in the first simulation (Figs. 13-14) and is due to the manifestation of the stochastic process of random walk. Therefore the random vortex method will, in general, not give exactly equal results despite of identical initial conditions. This characteristic also necessitates repeated simulations of the same flow to obtain ensemble averages of some quantitative predictions, e.g. drag coefficient.

The drag coefficient C_D is computed with eq. B.1 (Appendix B) in each flow simulation of 55 time steps. The reason for terminating the simulation after 55 steps is that the mean value of C_D , found by method described below, from step 26 to 40 and the mean value from step 41 to 55 differ by less than one percent. The flow simulation is repeated five times and the averaged results are shown in Fig. 17. During the first few steps the drag grows monotonically and rapidly due to the impulsive start of flow. Again, the random nature of this simulation causes the drag to fluctuate. The mean value of C_D oscillates only slightly from time = 4 until time = 11 when each simulation ends. The mean value of 1.47 differs by less than 7% from the measured value of 1.38 (Schlichting,1968). Although a good fit of C_D does not imply good fits of all details of the flow, the overall simulation should be reasonably realistic. Therefore algorithms based on the random vortex method and the vortex sheet method similar to the above simulation will

be utilized to find the fluid mechanical effects exerted on flame sheets by vorticity shed from a circular cylinder flame holder.

Two other sets of simulations are done with Reynolds' numbers of 1,000 (Figs. 18-19) and 10,000 (Figs. 20-21). The general features of the computed flow fields are all similar. However, the wake of Re = 10,000 flow seems to be narrower as a higher Reynolds' number implies a smaller viscous region of the overall flow. The drag coefficient for Re = 1,000 is shown in Fig.17 and the mean value is found to be 1.08 as compared with the experimental value of 1.04. When Re = 10,000, the computed mean value of C_D is 1.15 (Fig.17b) against the experimental value of 1.12.

3.2 Reacting Flow Simulations

3.2.1 Volume Expansion Due to Combustion

The simplest source-type flame model is the one which does not include the vorticity generated by the flame , nor the freestream turbulence, nor the vorticity shed from the flame holder. The complexity of the flame model is increased in levels by adding flame vorticity, turbulence, and flame holder vorticity one at a time. At each level, two versions will be presented, one for the existing source model and the other for the modified source model. The results of increasingly

complex models will be presented in the same order. Cheng's (1984) experiment (Fig.22) is chosen as a target of simulation because the velocity field was reported in more details. The input parameters for simulating Cheng's experiment are: volume expansion ratio $v = 6.7$, $S_L = 0.44\ m/s$, $U_\infty = 5.5\ m/s$, and $\delta = 0.001\ m$. The radius of the inner pipe and U_∞ are used as length and velocity scales to nondimensionalize the calculation. Measured U_x and U_y velocity profiles are presented in Figs. 23 and 24, respectively. Velocity profiles U_x and U_y computed with the existing source model for the simplest case (i.e., without accounting for flame vorticity) are shown in Figs. 25 and 26, respectively. The above sequence will be used for presenting all computed velocity profiles, that is, U_x first and then U_y. Dotted lines in Fig.25 indicate velocity jumps across the flame sheet. Therefore the locations of dotted lines in Fig.25 also indicate how the straight flame sheet is inclined relative to the X-axis. The most apparent feature of the computed profiles is that they bear little resemblance to the measured profiles in Fig.23. The flame angle deduced from the inclination of the flame sheet is 32 degrees while the measured angle is 14 degrees. The relative error is more than 110 %. When turbulent burning velocity is given as $S_T = U_\infty \sin \theta_f$, where θ_f is the flame angle, the computed S_T will have a relative error of about 120 %. Since S_T is frequently used in practical applications, a more accurate computed flame angle is highly desirable. Further, the flame angle is more easily measured in an experiment than detailed velocity profiles. Therefore it is easier to assess the relative merit of flame models by comparing computed flame angles with the measured angles. The inability of the existing source model to produce reasonably

accurate predictions of flame angles has been identified (Ashurst 1987) to be a major obstacle to developing the existing source model for any possible practical use. Often, as shown later, the existing source model produces superficially good-fitting velocity profiles. However, the large error in computed flame angle associated with the existing source model renders the computation almost irrelevant. That is when the computed profiles are adjusted according to the correct flame angle, the superficial similarity is readily exposed. The above-mentioned exercise will be presented later. Profiles of U_x and U_y computed with the modified source model are shown in Figs. 27 and 28. The above figures are obtained with a source discharge strength of $0.25u_s$ on the upstream side, the reason for this choice of source strength will be explained later in this section. In Fig.27 the marked reduction of the computed flame angle (20 degrees) is implied by velocity jumps located closer to the X-axis. The relative error is 43 %, which is about 2.5 times as small as the error given by the existing source model. Figs. 25 and 27 show that the computed U_x profiles (both the existing and the modified source models) assume higher values at position farther downstream from the flame holder. The cause of the above behavior can be found in eq.(2.23) which says that the contributions to U_x due to source disks far from the flame holder are negative at points near the flame holder. Eq.(2.23) has the same kind of effects on both the existing and the modified source models. Since the modified source model has a stronger strength in the region behind the flame than the existing model does, the effect of negative contributions to U_x is more pronounced and the

computed U_x profiles in Fig.27 consistently take on lower values than profiles at the same transverse (i.e., X) position in Fig.25.

Figs. 26 and 28 both show positive U_y before the flame and negative U_y behind the flame. The implication is that the fluid is pushed away from the X-axis before the flame while pushed toward the X-axis behind the flame. The negative magnitude of U_y is greatest at points close behind the flame where the hot products are accelerated. U_y gradually increases to zero when the X-axis is neared as the symmetry condition requires.

3.2.2 Vorticity Produced by Flame

When the flame vorticity is included, the computed velocity profiles are shown in Figs. 29, 30, 31 and 32. The first two are U_x and U_y computed with the existing source model respectively, the latter two with the modified model. Now, the calculated U_x profiles (Figs. 29,31) are shown in dotted lines and superposed with measured profiles shown in solid lines. The general trend of increasing U_x simulated behind the flame results in the significant improvement vs the no-flame-vorticity case. The modified source model discharges less strength to retard the freestream and gives approach U_x values closer to experimental data than the existing model. Figs. 30 and 32 display calculated U_y profiles. Both the existing and the modified source models can mimic the general trend of experimental curves where U_y is positive. Fig. 32 is computed with 25% source strength allo-

cated to the upstream side of a source disk; Fig. 33, 10%; Fig. 34, 0%. When compared with the experiment, both Figs.34 and 35 show too little lateral spacing between profiles. Therefore, for all subsequent computations 25% is selected to simplify the issue and to reduce computation cost. It is interesting to note that the inclusion of flame-generated vorticity does not wrinkle the straight flame sheet. This is a good feature of the source-type flame model. Otherwise, the flame model will contradict the empirical fact that a straight or smoothly curved flame sheet without wrinkles can be stabilized on a thin rod in a laminar reactant flow. The above fact is often utilized in determining the laminar flame speed of gaseous combustible mixtures.

3.2.3 Flame Vorticity and Freestream Turbulence

The turbulent supply flow of reactants is simulated by injecting vortices into the uniform flow at $x = -5\ cm$ and a random value of y between 0 and 5 cm. One vortex is injected at each time step and symmetry of the flow is assumed. A usual practice is to use vortices of uniform size. This study uses vortices with variable radii between 2.5 mm and 5 mm when each value within the range has an equal probability to appear. The integral scale of the supply flow was reported by Cheng to be 5 mm. The vortices have an identical strength which is found by numerical trials until the r.m.s. fluctuations of U_x and U_y are both in the range of 4% to 5% relative to U_∞ as in Cheng's experiment. Cheng measured turbulence fluctuations at $x =$ 10, 20, 30, 40, 50 and 60 mm above the flame stabilizer.

At each elevation, 20 points were sampled at 1 *mm* space in the Y-direction. The turbulence intensity was found to be nearly isotropic and decayed slightly. He reported a value of 5% at $x = 10\,mm$ and used the above value to characterize the flames he studied. The simulation of turbulence is not exact, but it is close enough to illustrate the basic influence of turbulence on a laminar flame sheet. Fig. 35 shows computed r.m.s. fluctuations of U_x and U_y at $x = 10, 20, 30, 40, 50,$ and $60\,mm$. The above figure shows that the turbulence intensity varies only slightly with x over the region of interest. Due to assumption of symmetry, U_x' is amplified by image vortices near the axis of symmetry but U_y' is canceled. Therefore the curves of U_x' all show the trend of increasing near the axis of symmetry while the curves of U_y' gradually decrease to zero on the axis of symmetry. To obtain the above figures, a vortex disk with a strength of $0.0046\,m^2/s$ is injected at every time step from step 1 and an ensemble average is taken over 200 steps starting from 401 to 600. Then the mean values of three ensembles are found and plotted. An example of ensemble averages and their mean values of U_x fluctuations at $x = 30\,mm$ is given in Fig. 36.

The velocity at each sampling point is also averaged over 200 steps from step 401 to 600 and presented in Figs. 37, 38, 39 and 40. Again, the first pair are results found with the existing source model. When computed turbulent U_x profiles (Fig.37) are compared with nonturbulent ones (Fig.29), the most apparent difference is that the velocity jumps in Fig. 37 are not as abrupt as those in Fig. 29. This is because a flapping wrinkled flame sheet will spread the effect of a velocity jump over some finite region and reduce the abruptness of a jump. A series of

instantaneous shapes of a wrinkled flame sheet are shown in Fig. 41 from step 401 to 600 every 25 steps. When all instantaneous shapes are superimposed in Fig. 42, the resultant shape is very similar to a turbulent flame brush. Fig. 42 shows the turbulent flame brushes simulated with both the existing and the modified source models. If the points half way between the front and rear edges of a turbulent flame brush are taken as the mean flame position, one can see that the modified source model still gives a smaller flame angle than the existing model does. The mean flame angles are 16 and 20 degrees respectively. As the complexity of our flame model increases, the modified source model consistently estimates the flame angle more accurately than the existing source model does. Additional computations are made to simulate flames studied by other workers. Dandekar and Gouldin (1984) reported V flames of air/methane and air/ethylene mixtures stabilized by a thin circular cylinder. The relevant parameters and calculated flame angles are listed in Table. 1. For all cases, the modified source model estimates flame angles closer to reality than the existing source model does. Also note that the above cases encompass V flames of different reactant mixtures and equivalence ratios. Therefore the improved accuracy of computed flame angles is not limited to Cheng's experiment. The Reynolds numbers of each flame are also listed, these are based on the radii of the suplly pipes.

Fig. 39 shows that the U_x profiles calculated with the modified source model are shifted left of the measured profiles. At $x = 60\,mm$, the first rise of U_x in measured profile appears near $y = 28\,mm$ but the first rise in the calculated profile appears near $y = 24\,mm$. A possible cause of the above behavior is that the

amplitude of flame flapping due to simulated turbulence is not as large as that of flapping due to turbulence in the real flow. One may also notice that the profiles in Fig. 37 are not shifted leftward as much as those in Fig. 39. The reason is simply that the existing source model extends a larger flame angle into the approach reactant flow and therefore, with equal magnitude of flapping, will cause the velocity profiles to rise at locations farther upstream.

All U_x profiles in Fig. 37 are translated horizontally toward left (Fig. 39a) such that the mean flame angle is equal to the measured angle. Now, the shortcomings of the existing source model are plain to see.

The computed turbulent U_y profiles are in Figs. 38 and 40 for the existing and the modified source models respectively. Neither model shows enough dispersion among the U_y curves before the flame when compared with the experiment. However, the modified source model does show (Fig. 38) more dispersion than the existing source model shows. The above observation is going to hold for all computations with increasing complexity of the flame model.

Axial velocity (U_x) profiles computed by both the existing and the modified source models exhibit very steep trends of increase near the x-axis. Since this behavior is similar and even maybe related to the increase of r.m.s. u' fluctuations (Fig. 35) near the x-axis due to the effects of image vortices, modifications to the numerical code were made to relax the assumption which at first simplified the programing task. In principle, the algorithm without symmetry of flow is the same as that

with symmetry. The essential difference is that the programming is much more complex when symmetry is not utilized and more caution and bookkeeping are needed. U_x profiles computed with the existing source model (Fig. 43) and with the modified source model(Fig. 45) both show much reduced rate of increase in U_x near the x-axis. At locations $5 \neg 10$ *mm* or more away from the x-axis there is not apparent influence due to the relaxation of the assumption of symmetry. U_y profiles computed with both source models do not show appreciable differences either. However, the averaged U_y values on the x-axis are not equal to zero like before when computed with symmetry. The deviations are small and usually on the order of 0.01 *m/s*. The implication is that while a turbulent flow is symmetric in the time mean sense it is not symmetric at any instant when a frozen picture of this turbulent flow is taken. In a turbulent flow transfer of vortices across the axis of symmetry takes place at all times. If the numerical code reflects any vortex which goes across the axis of symmetry, an important physical mechanism is lost to the simulation. In the present simulation a clockwise vortex in the right half plane will induce a positive velocity increment on the x-axis. When the above vortex goes across the x-axis, it will induce a negative velocity increment instead. By reflecting the above vortex back into the right half plane we not only introduce a positive velocity increment which shouldn't be but also introduce another positive increment due to the image vortex. Therefore the rate of increase of U_x near the x-axis becomes excessively high in this region.

All U_x profiles in Fig. 43 are translated leftwards horizontally (Fig. 45a) to correspond to the measured flame angle. Once again, it is shown that the existing

source model only achieves superficial closeness to experiment by overestimating the flame angle.

The U_y profiles computed without flow symmetry assumption are presented in Figs. 44 and 46 for the existing and the modified source models respectively. The modified source model (Fig. 46) still produces larger dispersion before the flame when compared with the existing source model (Fig. 44).

3.2.4 Flame Vorticity, Freestream Turbulence, and Flame-Holder Vorticity

The simulation of stream past a circular cylinder is now combined with the flame model which has included the flame vorticity and the freestream turbulence and the symmetry condition is relaxed. Since the freestream turbulence is included, the behavior of such a flow past a circular cylinder is expected to be different from that without freestream turbulence. The same parameters as in the previous section are employed to simulate 5% r.m.s. fluctuations in the coming flow. The Eulerian velocity field is shown at times 2,5,8, and 11 in Fig. 47. Although the eddy structures are not as clean-cut as in earlier figures, eddy structures and reduced U_x in the wake region are still identifiable. The undulating appearance is very interesting and will be mentioned with other context in the following section.

The vorticity production on the surface of the circular cylinder both in a nonturbulent and a 5% turbulent approach flow is compared in Fig. 48 and Fig. 49 for

the positive and the negative senses of rotation respectively. The turbulent background flow produces about 5% more vorticity in either sense of rotation. The absolute values of the positive and the negative vorticity production are nearly equal within each case. The instantaneous production of vorticity by the turbulent and the nonturbulent approach flows is superposed in Fig. 50. for both the clockwise and the counterclockwise vorticity. Again, it can be seen that the two production mechanisms are different but their general behavior is very similar.

The diameter of the flame holder in Cheng's experiment is 0.001 *m*. Calculated U_x and U_y profiles are shown in Figs. 51, 52, 53, and 54. The most apparent improvements are illustrated by the change of shape of U_x profiles (Figs. 51 and 53) at $x = 10$ and $20\,mm$ in regions near the X-axis. Although the amount of vorticity shed by the flame holder is about 1% of that generated by the flame sheet, its influence is considerable. Fig. 55 shows the position of all vortex disks shed by the flame holder in a region up to 10 diameters behind the cylinder. The lateral dispersion of vortex disks increases with increasing x in general. At 10 diameters behind the cylinder, the above dispersion is less than 1.5 diameters on either side of the X-axis. Since the induction due to a vortex is nearly inversely proportional to the square of distance (eq. 2.23), those vortex disks near the X-axis will exert a relatively stronger influence at a point on the axis than more powerful vortex disks can exert from positions far away. Fig. 55 also shows that vortex disks with different senses of rotation become intermingled as they move farther behind the cylinder. Eventually, their inductions will be cancelled mutually and the velocity profiles at stations far downstream should not be affected.

This can be confirmed by comparing Fig. 51 with Fig. 43 (the existing source model including and not including the flameholder vorticity) and by comparing Fig. 53 with Fig. 45 (the modified source model including and not including the flameholder vorticity) to see that the U_x profiles at $x = 40, 50$, and $60\,mm$ are almost identical whether the vorticity shed by the flame holder is included or not. There is no detectable change in flame angle despite the inclusion of vorticity shed by the flame holder.

Every U_x profile in Fig.51 is shifted leftwards (Fig.55a) so that the computed flame angle equals the measured flame angle. As found by similar exercises before, the existing source model does not simulate the velocity field as well as it first appears.

The present level of flame model including sources, vortices, turbulence, flameholder vorticity and relaxed symmetry condition is applied to two selected cases among those studied by Dandekar and Gouldin, namely flames 3 and 6 in Table 1. The computed profiles for flame 3 are plotted in Fig. 56 and those for flame 6 are in Fig. 57. The effects of the flame holder , though weak, are present in Fig. 56. The above two figures each consists of three curves: one measured in experiment, one computed with the modified source model, and one computed with the existing source model. The right-hand end-points of the curves are labeled A, B, and C respectively for the experiment, the modified source model, and the existing source model. Point A is the reported forward edge of flame brush where Dandekar and Gouldin began taking velocity data. Points B and C are the for-

ward edge of flame brushes computed with the modified and the existing source model, respectively. Because the existing source model over-estimates the flame angle, it also errs more in the location of the forward edge of the flame brush. In Fig.56, the existing source model deviates from the experiment by about four times as much as the modified source model. In Fig.57, the relative error of the existing source model is five times as large as that of the modified source model.

3.3 Circular Cylinder Flame Holder

A thin circular cylinder can influence velocity field within a short range downstream by producing vorticity on its surface and shedding the produced vorticity into the surrounding flow. But the flame sheets are usually considered not being influenced and the thin cylinder is ignored in previous flame simulations (e.g. Pindera and Talbot 1986) on the ground that the vorticity shed by the cylinder is about two orders of magnitude smaller than that produced by the flame sheets. Intuitively, the above can not be true for a larger cylinder. Consider a circular cylinder with 1 *cm* radius being used as a flame holder. Then the vorticity shed by the above cylinder needs to be computed. The method presented in Appendix A carries out nondimensional computations when simulating flow past a circular cylinder. Therefore, the size of a 2-D cylinder makes no difference as far as the numerical computation is concerned. However, the dimensional radius of discrete vortices shed by a larger cylinder will be different if the circumference of the cyl-

inder is still divided into the same number of segments. Suppose the circumference of a cylinder with 1 *cm* radius is divided into 20 segments, then each vortex sheet generated on the surface is 0.1π *cm* long. When the above vortex sheet turns into a vortex disk, the radius of the vortex disk is 0.05 *cm*. Thus, the above vortex has a dimension comparable to that of the thickness of a laminar flame sheet. Such small vortices should give adequate small-scale resolution in computations in which flame wrinkling due to large flow structures (e.g., recirculating eddies in the wake of a cylinder) is simulated numerically. To save computation cost the circle will still be divided into 20 segments for all subsequent computations. The relative magnitude of the cylinder algorithm step size and the flame algorithm step size is different from the case of a 1 *mm* diameter cylinder and the stability requirement is different too. After some trials, the length of each flame segment is set to be 0.004 *m*. Since those eddy structures observed in the cold flow simulations are on the order of the diameter of the cylinder, intuition suggests that a flame sheet must be at least twice as long as the diameter to reveal sufficiently the deformation of the flame sheet due to eddy structures behind the cylinder. The length of the flame sheets is chosen to be 0.048 *m*, and the sheets are divided into 12 segments each. A straight flame sheet is assumed to begin with. The flame sheets are attached on the surface of the cylinder at 100 and -100 degrees from the forward stagnation point. These locations are the average position of separation points. The separation points move to and fro about both shoulders of the cylinder as the simulation of stream past a circular cylinder shows. A fixed average position is assumed to simplify the problem. The shapes of flame sheets are

written out at every step from step 50 onwards to 70 when the simulation stops. Initially the simulation was done for 55 steps, but the expected flame extinction due to over-stretch of flame sheet was not obtained and the simulation was extended to 70 steps when several occurrences of flame extinction had been observed. During the first few steps, there is not enough vorticity shed by the cylinder to wrinkle the flame sheet much. Later on, as the amount of vorticity accumulates, the flame sheet is considerably wrinkled and the stretch rates of some flame segments can increase significantly. Because a variable laminar flame speed is computed for each and every flame segment in every time step by eq. (2.15), which is $S_L = S_U(1 - \frac{\Lambda K}{S_U})$ with Λ being the Markstein length scale and K the rate of flame stretch. Clearly, negative S_L will be encountered when K is sufficiently large. However, S_L must first reach zero before it can go from a positive number to a negative number. When $S_L = 0$, it simply means that no reactants are consumed by the flame or alternately, the flame is extinguished. Therefore, all negative laminar flame speeds obtained during a time step are set to zero and the corresponding flame segments are carried through the calculation as inert line segments until the stretch rates of the above segments are suitable for positive laminar flame speeds. The above manner of treating extinguished flame segments is a much simplified way to mimic the highly complex phenomenon of flame reignition by hot combustion products. It should be mentioned that when a flame segment is considered inert, the segment does not shed any flame vortices. The segments which have zero laminar flame speed are recorded in the output and such segments are deleted when plotting the flame sheets. According to the

output of one simulation, there are three steps which contain deleted flame segments between step 50 and 60 (Fig. 58). In order not to clutter the picture too much and for comparison only one continuous flame sheet is shown along with three broken flame sheets in Fig. 58. The broken flame sheets are reminiscent to flame extinction and fragmentation due to high rates of flame stretch observed in combustion experiments.

As mentioned at the end of Sec. 3.2, the flame vortices will not wrinkle a straight flame sheet. Therefore, it does not matter whether the flame sheets anchored near the shoulders of a circular cylinder are 5 *cm* or 200 *cm* long as far as the wrinkling effect due to flame vorticity is concerned. The presently adopted practice is to neglect the flameholder-generated vorticity when it is 2 orders of magnitude smaller than the flame-generated vorticity. The vorticity shed by the cylinder is on the order of $U_\infty d$ (Roshko 1953), where d is the diameter of the cylinder. The flame-generated vorticity is on the order of $U_\infty l$, where l is the length of one flame sheet. For a 2 *cm*-diameter cylinder and two 200 *cm* long flame sheets, the accepted practice says that the cylinder-generated vorticity can be neglected and there will be no flame wrinkles as those shown in Fig. 58. It is simply inconsistent with experience that a cylinder of 2 *cm* diameter will not produce wrinkles in flame sheets stabilized by the cylinder, even when the approaching reactant flow is laminar. The key to the puzzle is the size of recirculating eddies behind the cylinder. The size of recirculating eddies behind a circular cylinder is approximately the same as the diameter of the cylinder (Fig. 14). For a diameter of 1 *mm*, the eddy size is on the same order as the thickness of a laminar flame sheet.

Therefore the internal structure of a flame sheet will be affected by the above eddy, but the overall structure will not be. While in the case of a large cylinder of 2 *cm* diameter, the eddy size is one order of magnitude larger than the flame thickness and highly visible wrinkling effect is obtained through computation as expected. The smallness of flameholder vorticity relative to flame-generated vorticity is not a proper justification to neglect flameholder vorticity. Instead, the relative size of recirculating eddies compared with laminar flame thickness is the criterion to use. The combined Eulerian and Lagrangian pictures of the reacting flow are snapshot at time steps 50, 60, and 70 in Figs. 59, 60, and 61, in the same order. The thicker arrows are velocity vectors at fixed sampling points and the finer arrows are velocity vectors at the locations of the vortices. The above vortices are generated by the flame and one is shed from every flame segment , except those extinct ones, at each time step. There are some twenty odd new flame vortices entering the computation at each time step and their number quickly grows into thousands with quadruple increase in computation cost. In order to retain the necessary resolution, grid systems are not used. The flow field displays an undulating appearance, which is very similar to the wake of a circular cylinder in a turbulent approach flow (Fig. 47). Note that in the present reacting flow simulation the freestream turbulence is not included. Therefore, combustion appears to influence the wake of a circular cylinder in a way similar to that freestream turbulence influences the wake. The flame vortices, or the finer arrows in Figs. 59, 60, and 61, roughly mark the region occupied by the heated combustion products. One can see that the heated flow first converges and then

opens out. Such behaviors have long been noted in combustion experiment (Fig. 62). In regions between the outward fingers formed by the flame vortices the fresh reactants are caught in the undulating movement. However, the vortex-induced velocity is not significant. Therefore the entrainment of fresh reactants into the flame zone is not readily explained by the Biot-Savart induction only. Engulfment is also a possible mechanism (Townsend 1970) for the mixing process in a turbulent wake. The destruction of alternating eddy-shedding by combustion is numerically mimicked as observed in experiment by many researchers before.

It might appear that there is not enough influence from the source disks when one judges by the moderate amount of velocity deflection before the product zone. To clarify, numerical experiments were done by placing two stationery straight source lines at both shoulders of a circular cylinder, one line to each shoulder. Each source line is made up of 12 source disks while all disks are given equal strength typical of a flame segment with an expansion ratio of 6.7. To isolate the effect of the source disks, the cylinder is set not to shed any vorticity. The computed flow field is shown in Fig. 63a. The above figure shows that the velocity deflection is indeed moderate before the source lines. When the strength of each source disk is increased to five times as large as a typical flame source disk, the computed flow field (Fig. 63b) shows increasing velocity deflection but certainly not a fivefold increase. Therefore the moderate velocity deflection before the product zone is judged normal in the simulation of this flow configuration.

3.4 Flat Plate Flame Holder

3.4.1 Nonreacting Flows Normal to a Flat Plate

The flow field of a uniform stream over a flat plate normal to the stream is obtained by conformal mapping from that of a uniform stream over a circular cylinder. The diameter of the cylinder is 2 *cm* as in the previous section. Variations in the algorithm are as follows. The generation of vortex sheets is done in the cylinder plane as well as the convective motion of vortex sheets near the surface of the cylinder. Then the cylinder is mapped into a flat plate together with all vortex sheets residing near the surface. Random walks of vortex sheets are implemented in the plate plane. After random walks are completed, all sheets are checked to see if any one ends up outside the numerical shear layer around the plate. Those sheets which are outside the layer are converted to vortex disks. Now, all vortex disks must be mapped back into the cylinder plane in order to find the convective motion of each vortex. Then, random walks of each vortex disk is found in the plate plane and any vortex disk which reenters the numerical shear layer is converted to a vortex sheet. The emphasis is that random walks must be found in the physical plane where the flow of interest is, i.e., the plate plane. Three sets of flow simulations are done for Re = 2,000, 10,000 and 50,000. Figs. 64 and 65 show the velocity fields for Re = 2,000 at fixed sampling points and at each vortex. The velocity fields of the case Re = 10,000 are in Figs. 66 and

67. Figs. 68 and 69 portray the velocity fields when Re = 50,000. The clear presence of recirculating eddies is similar to flow past a circular cylinder. However, there is one apparent difference. The eddies behind a circular cylinder usually occupy a region laterally wider than the diameter of the cylinder. But the eddies behind a flat plate take up a region narrower than the height of the flat plate and the boundary of the above region tapers clearly toward the downstream direction. The possible reason for this tapering is the strong negative pressure behind the plate as discussed by Goldstein (1938) and Hoerner (1972) in regard to the drag coefficient of a flat plate normal to stream. The C_D of a flat plate computed with the random vortex method is plotted in Fig. 70 for Re = 2,000, 10,000, and 50,000. The reference C_D for Re = 1,000 and 10,000 is taken from Hoerner(1972) to be 1.98, which is stated to be valid between Re = 10,000 and 100,000. The same value is also used as a reference for the case Re = 2,000. At Re = 50,000 the calculated C_D over the last 15 steps is 2.04 and that over the 15 steps before is 2.06. For Re = 10,000, the average values are 2.05 and 2.08. When Re = 2,000 , average C_D's of 2.01 and 1.97 are found. Again the proximity of computed C_D to measured ones indicates a reasonable overall approximation.

3.4.2 Reacting Flow Past a Flat Plate

Once more, flame sheets are anchored at the average separation point slightly behind the shoulders of a circular cylinder as in the previous section. After a conformal mapping the point where the flame sheet is anchored is near the edge

and on the down stream side of the flat plate. The flame sheet can not be anchored exactly on the edge because the mapped velocity on the edge is infinitive. The input parameters are the same as those mentioned in the second section of this chapter. Namely, expansion ratio $v = 6.7$, $S_L = 0.44\ m/s$, $U_\infty = 5.5\ m/s$, and $\delta = 0.001\ m$. Then the computation in the circle plane is mapped into the plate plane. Flame over-stretch and extinction are treated the same way as before. The wrinkled and broken flame sheets attatched to a flat plate are depicted in Fig. 71. Note that the flame sheet at step 61 has a point closer to the axis than other flame sheets at later time steps. This illustrates the flapping motion of flame sheets very clearly.

The velocity vectors at individual vortices are plotted in Figs. 72, 73, and 74 for steps 50, 60, and 70 of this simulation. The constriction of hot product flow behind the plate is very much pronounced. The combustion removes the easily visible eddies found in cold flow simulations and creates undulating motion as in the case for a circular cylinder flame holder.

CONCLUSIONS

A new source-type flame model has been developed to treat continuous laminar flame sheets in both turbulent and non-turbulent flows. The flame model includes the following effects :

1. Volume expansion due to heat released by combustion.

2. Vorticity generated by combustion.

3. Turbulence in the reactant supply flow.

4. Vorticity generated by the flame holder.

When the volume expansion due to combustion is represented by a modified source model proposed in this work, the accuracy of computed flame angles is improved for all cases tested. The test cases comprise an assortment of different reactant mixtures : four ethylene-air V flames, and two methane-air V flames of

different equivalence ratios. By replacing the existing source with the the modified source model, the relative error in predicted flame angle of V flames is reduced from 80% to 20% . Such an improvement is significant because the very large error associated with the existing source model for a relatively simple flame geometry poses difficulty to the validity of source-type flame model. As the results obtained with different reactant mixtures indicate, the improved accuracy of computed flame angle may be a general feature of the modified source model as far as V flames are concerned.

Turbulence simulated by injecting vortex disks of equal strength into the flow at every time step can cause wrinkles in an initially straight flame sheet. It is also found that a close approximation of r.m.s. velocity fluctuations does not necessarily create flapping motion comparable to actual flapping of flame in experiment. However, the wrinkling effects of simulated turbulence on laminar flame sheets are basically correct.

When axial velocity (U_x) profiles computed with the existing source model are shifted so that the computed mean flame angle matches the measured flame angle, it can be shown that the existing source model can only produce superficially fitting U_x profiles, which on appearance agree with experiment. However, the error in computed flame angle is quite large. The above observation holds for all levels of complexity of the flame model.

The relaxation of symmetric flow assumption removes the unrealistic reflection of vortex disks off the axis of symmetry and superfluous contributions from image vortices to the magnitude of U_x. The computed U_x profiles in regions near the axis of symmetry can be improved to better follow the trend of experimental data. For regions far from the axis of symmetry, no apparent improvement has been found.

The vorticity generated by a thin circular rod of 1 mm diameter is approximated by the random vortex method with vortex sheets near the surface of the rod. The vorticity shed from the rod is shown to influence velocity field near the axis of symmetry within 20 diameters downstream of the rod. Despite the smallness of rod-generated vorticity relative to the flame-generated vorticity, the former vorticity can not be ignored because of its proximity to the axis. The experimental results indicate a larger zone influenced by the flame holder than the computation shows. A possible reason is that many expediencies were employed to reduce computation cost.

Flames are wrinkled and stretched by the vortical flow field near a bluff body as shown by simulations of flame sheets near a large circular cylinder and those near a flat plate normal to stream. Flame extinction is found in both flow geometries at portions of flame sheets where the local laminar flame speed is reduced zero or less. The wrinkles appear to travel downstream along the flame sheets.

The existing practice of neglecting vorticity shed by a flameholder when the above vorticity is about two orders of magnitude smaller than the flame-generated vorticity has been found to be inappropriate. A better criterion is whether the size of the recirculating eddies behind the flameholder is on the same order or less than the laminar flame thickness. When the eddies are small relative to the flame thickness, the flameholder-generated vorticity can be neglected without affecting the solution of the flame movement.

The easily visible recirculating eddies found in non-reacting flows over a circular cylinder or a flat plate normal to stream are less clear-cut in computed reacting flows. This is consistent with experimental observations (Williams, Hottel, and Scurlock, 1944). However, a recirculating zone still exists behind the flameholder as observed in many combustion experiments. Furthermore, the computed recirculating zone in reacting flows is shorter than that in nonreacting flows. This, too, has been reported by combustion experimentalists (Lewis and von Elbe 1949).

The wake formed by hot combustion products is found, by numerical simulation, to pinch close to the flameholder (compared with the non-reacting flow) as well as found in experiment. The computed motion of the hot products takes on an undulating or a wiggling shape, which is also observed in experiment (Goix, Paranthoen, and Trinite, 1990).

The reacting flows computed in this work are for Reynolds numbers at the lower end of practical applications in airbreathing propulsion. When applying the random vortex method to flows of higher Reynolds numbers, the size of each vortex must be reduced and the number of vortices in the flow should be increased greatly to simulate the wide range of scales in a high Reynolds number flow. The main obstacle is prohibitively high cost. Subsequently, very little work has been done with high Reynolds number flows to clarify the convergence behavior (Ghoniem and Sethian 1988). As the capability of computers increases, attempts can be made to study flows of increasingly higher Reynolds numbers.

It is a significant limitation to simulate turbulence, which is a 3-D phenomena, with 2-D circular vortex disks. Chorin (1980) presented a method using vortex tubes to simulate 3-D turbulence. To this day, the above method has only seen very limited utilization. Osher and Sethian (1988) proposed a method to treat the propagation of a 3-D surface with curvature-dependent speed. In principle, an assault on 3-D turbulent combustion with a source-type flame model and random vortex method is a possibility.

References

1. Abdel-Gayed, R.G., Bradley, D., and Lung, F.K.K., "Combustion Regimes and the Straining of Turbulent Premixed Flames", *Combust. & Flame*, Vol. 72, 1989, pp. 213-218.

2. Andrews, G.E. and Bradley, D. "Determination of Burning Velocities : A Critical Review", *Combust. and Flame*, Vol. 18, 1972, pp. 133-153.

3. Ashurst, WM. T., "Vortex Simulation of Unsteady Wrinkled Laminar Flames", *Combust. Sci. & Tech.*, 1987, Vol. 52, pp. 325-351.

4. Ballal, D.R. and LeFebvre, A.H., "The Structure and Propagation of Turbulent Flames", *Proc. Roy. Soc. London*, A 344, 1975, pp. 217-234.

5. Batchelor, G.K., *An Introduction to Fluid Mechanics*, Cambridge U. Press, 1967.

6. Beale, J.T., and Majda, A., "High Order Accurate Vortex Methods with Expicit Velocity Kernels", *J. Comp. Phys.*, Vol. 58, pp. 188-208.

7. Bill, Jr., R.G., Namer, I., Talbot, L., and Robben, F., "Density Fluctuations of Flames in Grid-Induced Turbulence", *Combust. and Flame*, Vol. 64, 1982, pp. 277-285.

8. Borghi, R., "On the Structure and Morphology of Turbulent Premixed Flames", *Recent Advances in Aeronautical Science*, (C. Bruno and Casci, Eds.), Pergamon, 1984.

9. Bray, K.N.C., in "Turbulent Reacting Flow", (P.A. Libby and F.A. Williams, Eds.), *Topics in Applied Physics*, 4, Springer-Verlag , 1980.

10. Cheer, A.Y., "Numerical Study of Incompressible Slightly Viscous Flow Past Blunt Bodies and Airfoils", *SIAM J. Sci. Stat. Comput.* , Vol. 4, No. 4, 1983, pp. 685-705.

11. Cheng, R.K. and Ng, T.T., "Velocity Statistics in Premixed Turbulent Flames", *Combust. and Flame*, Vol. 52, 1983, pp. 185-202.

12. Cheng, R.K., "Conditional Sampling of Turbulence Intensities and Reynolds' Stress in Premixed Turbulent Flames", *Combust. Sci. Tech.*, Vol. 41, 1984, pp. 109-142.

13. Chorin, A.J. and Bernard, P.S., "Discretization of a Vortex Sheet with an Example of Roll-Up", *J. Comp. Phys.*, Vol. 13, No. 3, 1973, pp. 423-429.

14. Chorin, A.J., "Numerical Study of Slightly Viscous Flow", *J. Fluid Mech.*, Vol. 57, 1973, pp. 785-796.

15. Chorin, A.J., "Vortex Sheet Approximation of Boundary Layers", *J. Comp. Phys.*, Vol. 27, 1978, pp. 428-442.

16. Chorin, A.J., "Vortex Models and Boundary Layer Instability", *SIAM J. Sci. Stat. Comput.*, Vol. 1, 1980, pp. 1-21.

17. Chung, S.H. and Law, C.K., "An Invariant Derivation of Flame Stretch" , *Combust. and Flame*, Vol. 55, 1984, pp. 123-125.

18. Cimbala, J.M., Nagib, H.M., and Roshko, A., "Large Structures in the Far wake of Two-Dimensional Bluff Bodies", *J. Fluid Mech.*, Vol. 190, 1988, pp. 265-298.

19. Clavin, P. and Williams, F.A., "Effects of Molecular Diffusion and of Thermal Expansion on the Structure and Dynamics of Premixed Flames in Turbulent Flows of Large Scale and Low Density", *J. Fluid Mech.* , Vol. 116, 1982, pp. 251-282.

20. Clavin, P. and Joulin, G., "Premixed Flames in Large Scale and High Intensity Turbulent Flow", *Le J. De Phys.* - Letters, Vol. 44, 1983, L1-L12.

21. Damkohler, G., *Zt. f. Elektroch.*, Vol. 46, 1940, pp. 601-626 (NACA TM 1112, 1947).

22. Dandekar, K.V., and Gouldin, F.C., "Temperature and Velocity Measurements in Premixed Turbulent Flames", *AIAA J.*, Vol. 20, No. 5, 1982, pp.652-659.

23. Darrieus, G., "Propagation of Flame Front", Sixth International Congress of Appl. Mech., Paris, 1946.

24. Deshaies, B. and Cambray, P., "The Velocity of a Premixed Flame as a Function of the Flame Stretch : An Experimental Study", *Combust. and Flame*, Vol. 82, 1990, pp. 361-375.

25. Driscoll, J.F. and Gulati, A., "Measurement of Various Terms in the Turbulent Kinetic Energy Balance within a Flame and Comparison with Theory", *Combust. and Flame*, Vol. 72, 1988, pp. 131-152.

26. Einstein, A., *Investigation on the Theory of the Brownian MOvement*, Dover, 1956.

27. Emmons, H.W., *Fundamentals of Gas Dynamics*, Princeton U. Press, 1958.

28. Fox, M.D. and Weinberg, F.J., "An Experimental Study of Burner-Stabil ized Turbulent Flames in Premixed Reactants", *Proc. Roy. Soc. London*, A 268, 1968, pp. 222-239.

29. Fritsch, F.N. and Carlson, R.E., "Monotone Piecewise Cubic Interpolat ion", *SIAM J. Numer. Anal.*, Vol. 17, 1980, pp. 238-246.

30. Ghoniem, A.F., Chorin, A.J., and Oppenheim, A.K., 1982, "Numerical Modeling of Turbulent Flow in a Combustion Tunnel", *Phil. Trans. Roy. Soc. Lond.*, A 304, 1982, pp. 303-325.

31. Ghoniem, A.F., "Effects of Large Scale Structures on Turbulent Flame Propagation", *Combust. and Flame*, Vol. 64, 1986, pp. 321-336.

32. Ghoniem, A.F. and Cagnon, Y., "Vortex Simulation of Laminar Recirculating Flow", *J. Comp. Phys.*, Vol. 68, No. 2, 1987, pp. 346-377.

33. Ghoniem, A.F. and Givi, P., "Vortex Scalar Element Calculation of a Diffusion Flame Stabilized on a Plane Mixing Layer", NASA TM 100133, 1987.

34. Ghoniem, A.F., and Sethian, J.A., "Validation Study of Vortex Methods ", *J. Comp. Phys.*, Vol. 74, No. 2, 1988, pp. 283-317.

35. Goix, P., Paranthoen, P., and Trinite, M., "A Tomographic Study of Measurements in a V-Shaped H_2-Air Flame and a Lagrangian Interpretation of the Turbulent Flame Brush Evolution", *Combust. and Flame*, Vol. 81, 1990, pp. 229-241.

36. Goldstein, S. (ed.), *Modern Developments in Fluid Dynamics* , Oxford: The Clarendon Press, 1938.

37. Gouldin, F.C. and Dandekar, K.V., "Time-Resolved Density Measurements in Premixed Turbulent Flames", *AIAA J.*, Vol. 22, No. 5, 1984, pp. 655-663.

38. Graham, J.M.R., "The Forces on Sharp-Edged Cylinders in Oscillatory Flow at Low Keulegan-Carpenter Numbers", *J. Fluid Mech.*, Vol. 97, Part 1, 1980, pp. 331-346.

39. Gross, R. A. and Esch, R., "Low-Speed Combustion Aerodynamics", *Jet Propulsion*, Vol. 25, 1954, pp. 95-101.

40. Gulati, A. and Driscoll, J.F., "Velocity-Density Correlations and Favre Averages Measured in a Premixed Turbulent Flame", *Combust. Sci. and Tech.*, Vol. 48, 1986, pp. 285-307.

41. Gunther, R., "Turbulence Properties of Flames and Their Measurement", *Prog. Energy Combust. Sci.*, Vol. 9, 1983, pp. 105-154.

42. Gaydon, A.G. and Wolfhard, H.G., *Flames ,Their Structure, Radiation, and Temperature*, 4th ed., Wiley, 1979.

43. Hald, O.H., "The Convergence of Vortex Methods for Eulers Equation", *SIAM J. Numer. Anal.*, Vol. 16, No. 5, 1979, pp. 726-755.

44. Hayes, W.D., "The Vorticity Jump Across a Gasdynamic Discontinuity", *J. Fluid Mech.*, Vol. 2, 1959, pp. 595-600.

45. Hoerner, S.F., *Fluid Dynamic Drag: Practical Information on Aerodynamic Drag and Hydrodynamic Resintance*, Hoerner Fluid, 1972.

46. Hyman, J.M., "Numerical Methods for Tracking Surfaces", *Physica D*, Vol. 12, 1984, pp. 396-407.

47. Karasalo, I. and Namer, I., "Numerical Study of a Flame in a Karman Vortex Street", *Combust. and Flame*, Vol. 47, 1982, pp. 255-267.

48. Karlovitz, B., Denniston, Jr., D.W., and Wells, F.E., "Investigation of Turbulent Flames", *J. Chem. Phys.*, Vol. 19, 1951, No. 5, pp. 541-547.

49. Karlovitz, B. , Denniston, Jr.,D.W., Knapschaefer, D.H., and Wells, F.E., "Studies on Turbulent Flames : A. Flame Propagation Across Velocity Gradients, B. Turbulence Measurement in Flames", Fourth Symposium (Int'l) on Combustion, The Combust. Inst., 1953, pp. 613- 620.

50. Knuth, D.E., *The Art of Computer Programming*, Addison-Wesley, 1973.

51. Landau, F.D. and Lifshitz, E.F., *Fluid Mechanics*, Pergamon, 1975.

52. Lewis, B. and von Elbe, G., *Combustion, Flames and Explosion of Gases*, 2nd ed., Academic Press, 1967.

53. Libby, P.A. and Bray, K.N.C., "Implications of the Laminar Flamelet Model in Premixed Turbulent Combustion", *Combust. and Falme* , Vol. 39, 1980, pp. 33-41.

54. Libby, P.A., Linan, A., Williams, F.A., "Strained Premixed Laminar Flame with Nonunity Lewis Number", AIAA 22nd Aerospace Science Meeting, Reno, 1984.

55. Lighthill, M.J., "Dynamics of a Dissociating Gas Part I Equilibrium Flow", *J. Fluid Mech.*, Vol. 2, 1957, pp. 1-32.

56. Lin, C.C.,"On the Motion of Vortices in Two Dimensions", University of Toronto Studies, Applied Math. Series, No. 5, 1943.

57. Markstein, G.H., *Nonsteady Flame Propagation*, Pergamon, 1964.

58. Matalon, M. and Matkowsky, B.J., "Flames as Gasdynamic Discontinuitie s", *J. Fluid Mech.* Vol. 124, 1982, pp. 239-259.

59. Milne-Thomson, L.M., *Theoretical Hydrodynamics*, The MacMillan Press, 1968.

60. Moore, D.W., "The Discrete Vortex Approximation of a Vortex", Calif. Inst. of Tech. Rep. AFSOR-1064-69.

61. Namanzian, M., Sherpherd, I.G., and Talbot, L., "Characterization of the Density Fluctuations in Turbulent V-Shaped Premixed Flames", *Combust. and Flame*, Vol. 64, 1986, pp. 299-308.

62. Osher, S. and Sethian, J., "Front Propagating with Curvature-Dependent Speed : Algorithms Based on Hamilton-Jacobi Formulation", *J. of Comput. Phys.* , Vol. 79, 1988, pp. 12-49.

63. Pindera, M.Z., and Talbot, L., "Flame Induced Vorticity : Effects of Stretch", Twenty-first Symposium (Int'l) on Combustion, The Combust. Inst., 1986, pp.1357-1366.

64. Pindera, M.Z., and Talbot, L., "Some Fluid Dynamic Considerations in the Modelling of Flames", *Combust. and Flame*, Vol. 73, 1988, pp. 111-125.

65. Rajan, S., Smith, J.R., and Rambach, G.D., "Internal Structure of a Turbulent Premixed Flame Using Rayleigh Scattering", *Combust. and Flame*, Vol. 57, 1984, pp. 95-107.

66. Rosenhead, L., "The Formation of Vortices from a Surface of Discontinuity", *Proc. Roy. Soc. London*, A 134, 1932, pp. 170-192.

67. Roshko, A., "On the Development of Turbulent Wakes from Vortex Streets", NACA TN 2913, 1953.

68. Roshko, A., "On the Drag and Shedding Frequency of Bluff Cylinders", NACA TN 3169, 1954.

69. Roshko, A., "Structure of Turbulent Shear Flows : A New Look", *AIAA J.*, Vol. 14, No. 10, 1976, pp. 1349-1357.

70. Rotman, D. and Oppenheim, A.K., "Aerothermodynamic Properties of Stretched Flames in Enclosures", Twenty-first Symposium (Int'l) on Combustion, The Cobbust. Inst., 1986, pp. 1303-1312.

71. Schlichting, H., *Boundary Layer Theory*, 7th ed., McGraw-Hill, 1979.

72. Smith, J.R. and Gouldin, F.C., "Turbulence Effects on Flame Speed and Flame Structure", *AIAA J.*, Vol. 17, No. 11,1979, pp. 1243- 1250.

73. Sod, G.A., "A Random Vortex Method for Compressible Turbulent Flows", *Num. Meth. in Laminar and Turbulent Flows*, Vol. 5, C. Taylor, W.G. Habashi, M.M. Hafez, Eds., Pineridge Press, 1987, pp. 2075-2087.

74. Suzuki, T. and Hirano, T., "Dynamic Characteristics of Flame Fronts in a Turbulent Premixed Flame Zone", Twentieth Symposium (Int'l) on Combustion, The Combust. Inst., 1984, pp. 437-444.

75. Suzuki, T., Kudo, N., Kawamata, M., and Hirano, T., "Simultaneous Measurements of Gas Flow and Flame Front Movement in a Turbulent Premixed Flame zone", Twenty-first Symposium (Int'l) on Combustion, The Combust. Inst., 1986, pp. 1385-1391.

76. Takami, H., "A Numerical Experimentation with Discrete Vortex Approxi mation with Reference to the Rolling Up of a Vortex Sheet", Dept. of Aeron. & Astron., Stanford U., SUDAER 202.

77. Townsend, A.A., "Entrainment and the Structure of Turbulent Flow", *J. Fluid Mech.*, Vol. 41, Part 1, 1970, pp. 13-46.

78. Truesdell, C.J., "On Curved Shocks in Steady Plane Flow of an Ideal Fluid", *J. of the Aeron. Sci.*, Vol. 19, 1952, pp. 826-828.

79. Tsien, H.S., "Influence of Flame Front on the Flow Field", *J. Appl. Mech.*, Vol. 18, 1951, pp. 188-194.

80. Yoshida, A. and Tsuji, H., "Mechanism of Flame Wrinkling in Turbulent Premixed Flames", Twentieth Symposium (Int'l) on Combustion, The Combustion Inst., 1984, pp. 445-451.

81. Uberoi, M.S. , Kuethe, A.M. ,and Menkes, H.R., "Flow Field of a Bunsen Flame", *Phys. of Fluids*, Vol. 1, No. 2, 1958, pp. 150-158.

82. Williams, G.C., Hottel, H.C., and Scurlock, A.C., "Flame Stabiliza tion and Propagation in High Velocity Gas Streams", Third Symposium on Combustion Flame and Explosion Phenomena, 1949, pp. 21-40.

83. Wohl, K., Shore, L., von Rosenberg, H., and Well, C.W., "The Burning Velocity of Turbulent Flames", Fourth Symposium (Int'l) on Combustion, The Combust. Inst., 1953, pp. 620-635.

84. Yoshida, A., "Characteristic Time-Scale Distributions and Mean and Most Probable Length Scales of Flamelets in Turbulent Premixed Flame", Twenty-first Symposium (Int'l) on Combustion, The Combustion Inst., 1986, pp. 1393-1401.

85. Zeldovich, Ya.B. and Frank-Kamenetskii, D.A., Acta Physiochim, Vol. 2 , p. 348.

Table 1. Turbulent flame angles computed with the existing and the modified source models

Flames	1	2	3	4	5	6
Flame Shape	V	V	V	V	V	V
Measured Angle	12 deg.	13 deg.	14 deg.	11 deg.	14 deg.	11 deg.
Modified Source with Turbulence	14 deg.	13 deg.	15 deg.	12 deg.	16 deg.	12 deg.
Existing Source with Turbulence	21 deg.	19 deg.	20 deg.	18 deg.	20 deg.	18 deg.
Reactant Mixture	Methane-air 0.8	Methane-air 1.0	Ethylene-air 0.75	Ethylene-air 0.7	Ethylene-air 0.7	Ethylene-air 0.65
Laminar Flame Speed	0.31 m/s	0.44 m/s	0.48 m/s	0.44 m/s	0.44 m/s	0.41 m/s
Freestream Velocity	3.8 m/s	6.9 m/s	6.3m m/s	6.9 m/s	5.5 m/s	6.3 m/s
Expansion Ratio	6.5	7.4	7.3	6.7	6.7	6.3
Reynolds Number	9000	14000	15000	18000	14000	16000

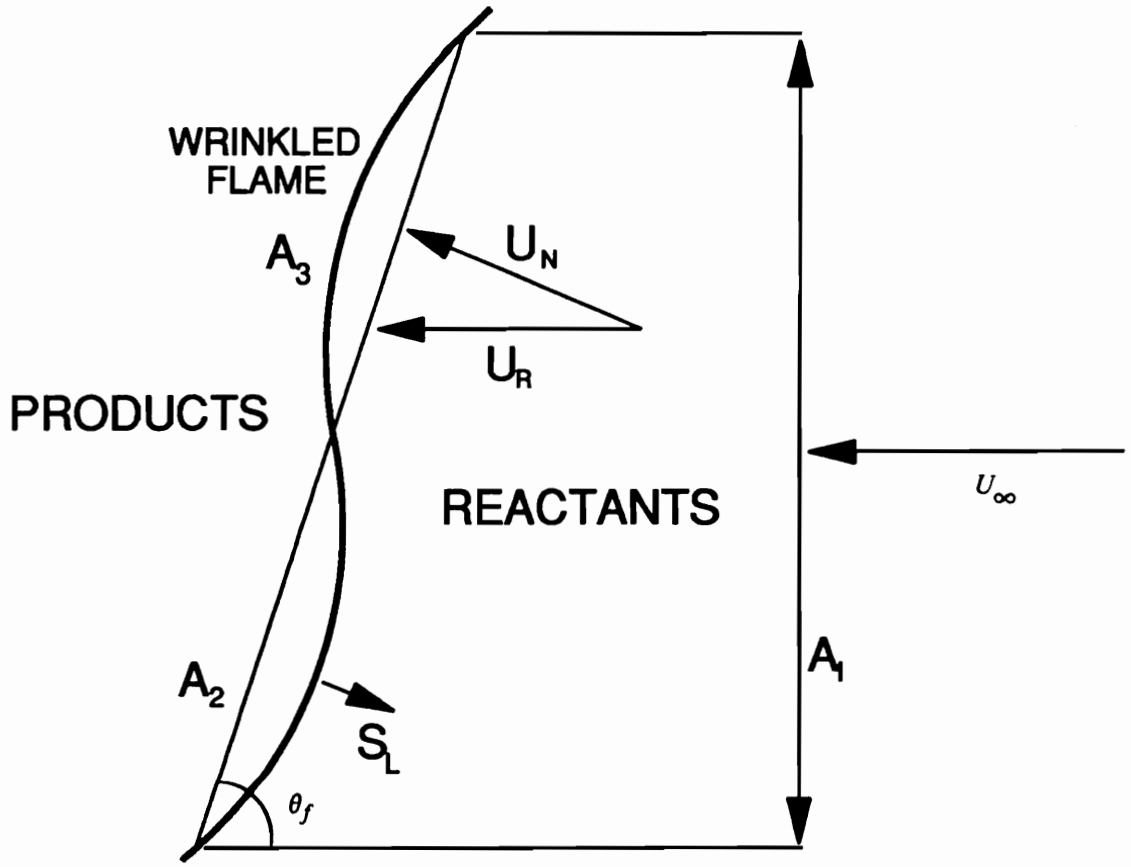

Figure 1. Wrinkled flame sheet increases surface area for reaction: Flame sheet is considered as an interface moving at stretch-dependent laminar flame speed S_L relative to the reactants.

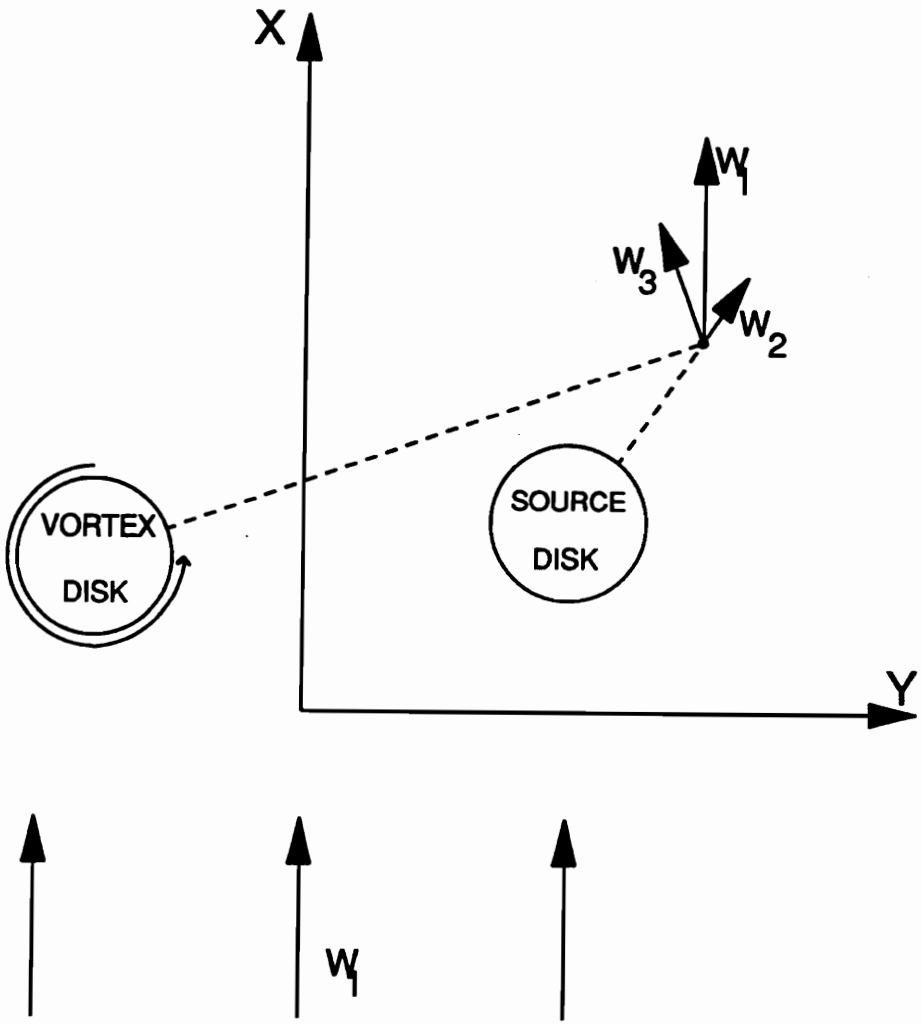

Figure 2. Decompose a vector field into three constituent parts: For the flame model used in this work: W_1 is a potential velocity field, W_2 is the velocity due to a source disk, W_3 is the induction due to a vortex disk.

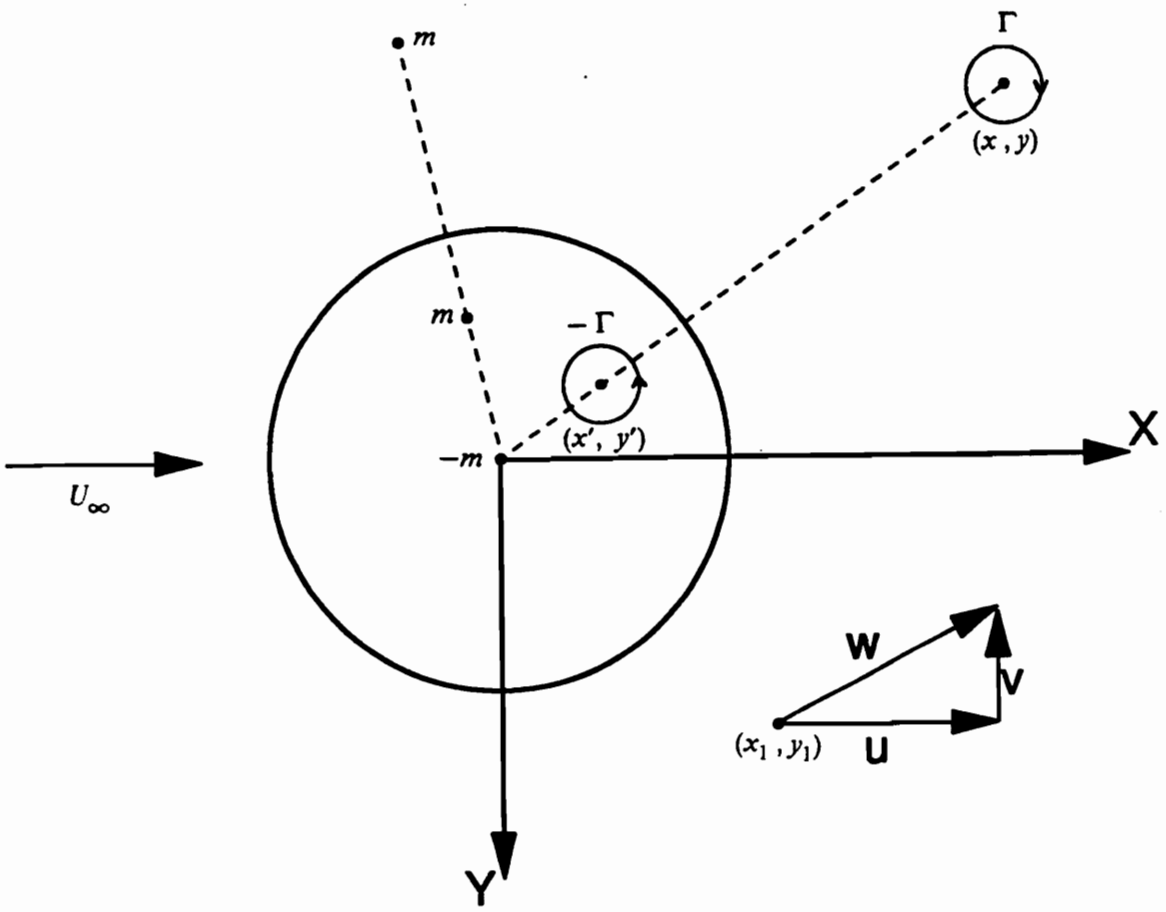

Figure 3. 2-D cylinder in a 2-D uniform freestream: Also included is the image vortex $-\Gamma$ of the vortex Γ. $(x_i' , y_i')$is the inverse point of (x_i , y_i). Image system will be mentioned in Sec. 2.4.4. The image system of a source m is also shown. The image m is at the inverse point and $-m$ is at the center.

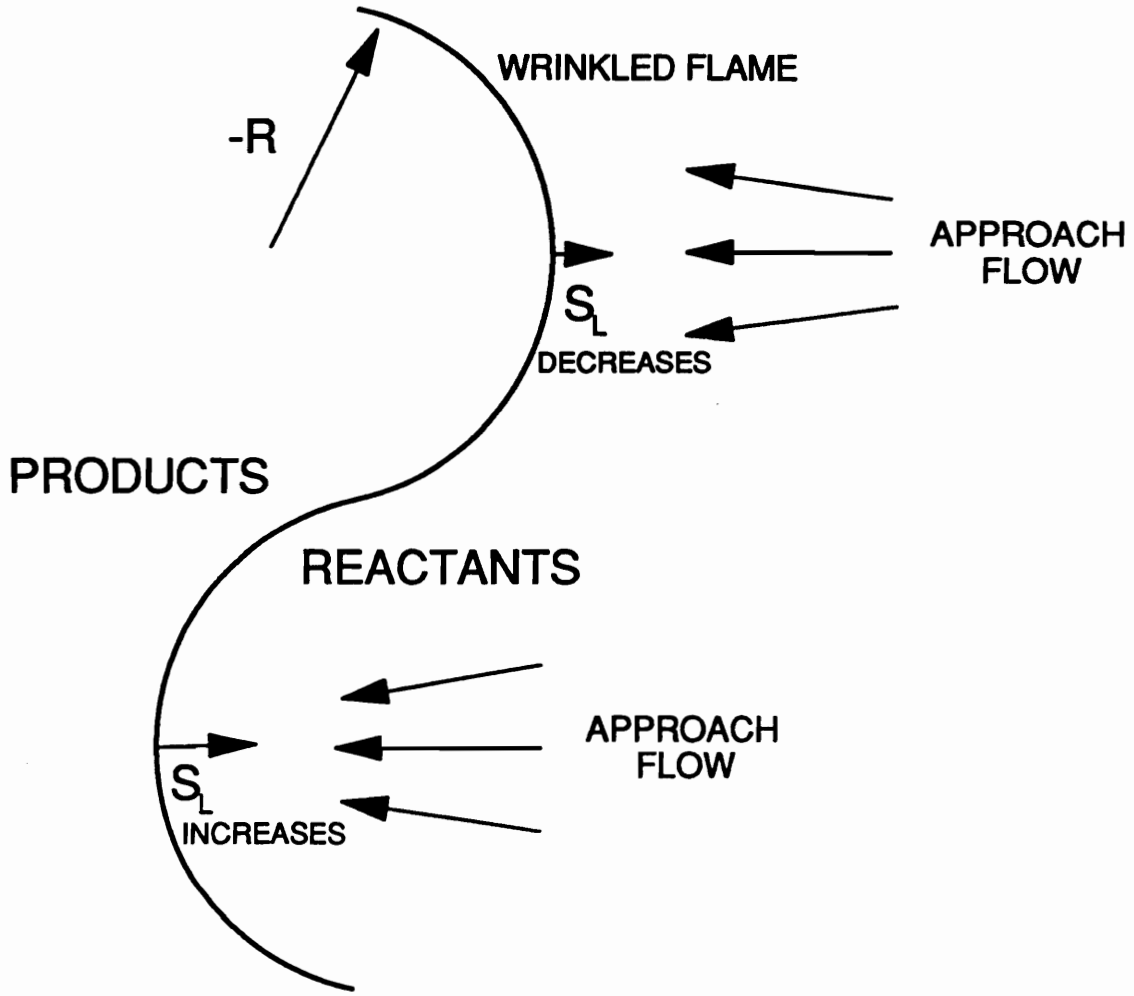

Figure 4. Variation of laminar flame speed due to stretch

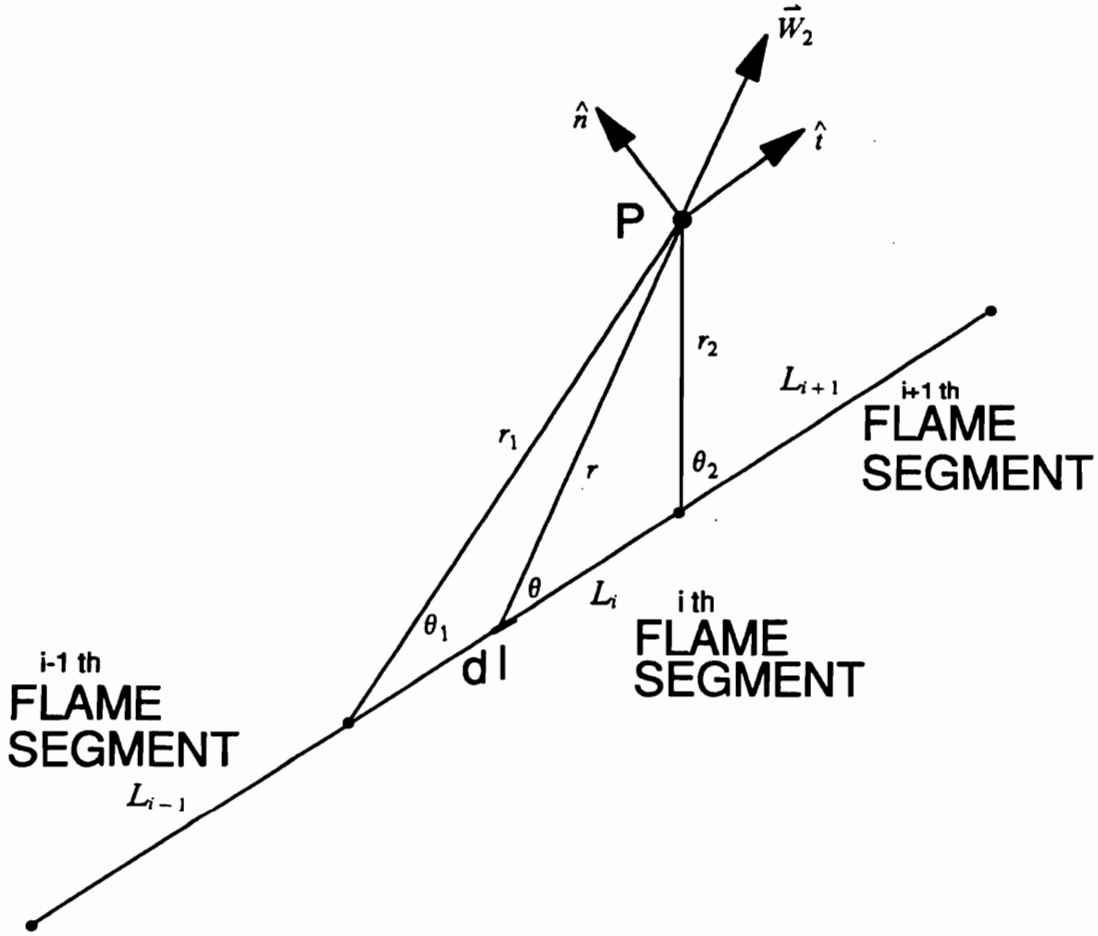

Figure 5. Velocity field established by a segment of a source line

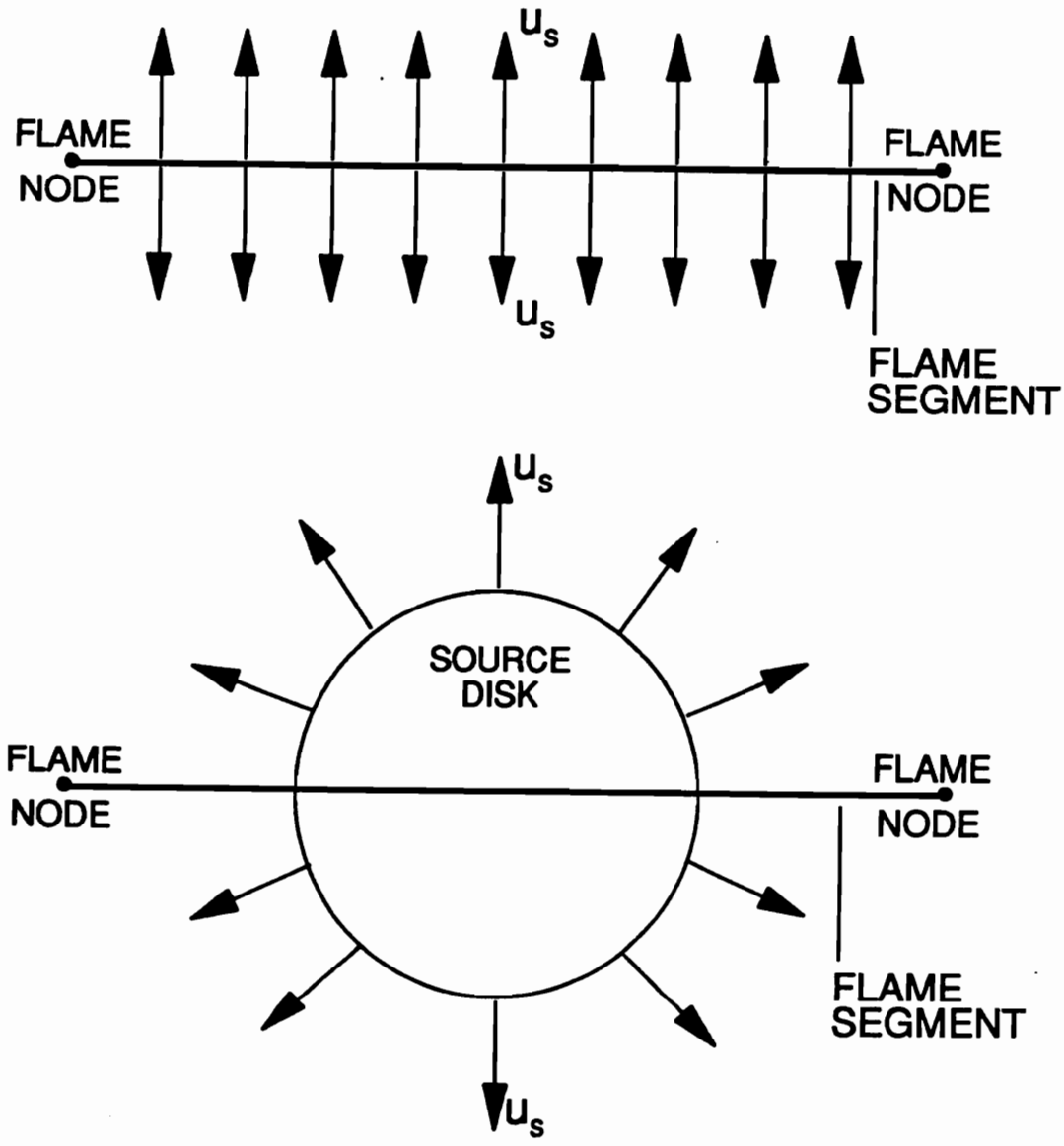

Figure 6. The existing source model: The flame segment discharges symmetrically into both the upstream and downstream sides. The flame segment is approximated by a source disk in the lower part of this figure.

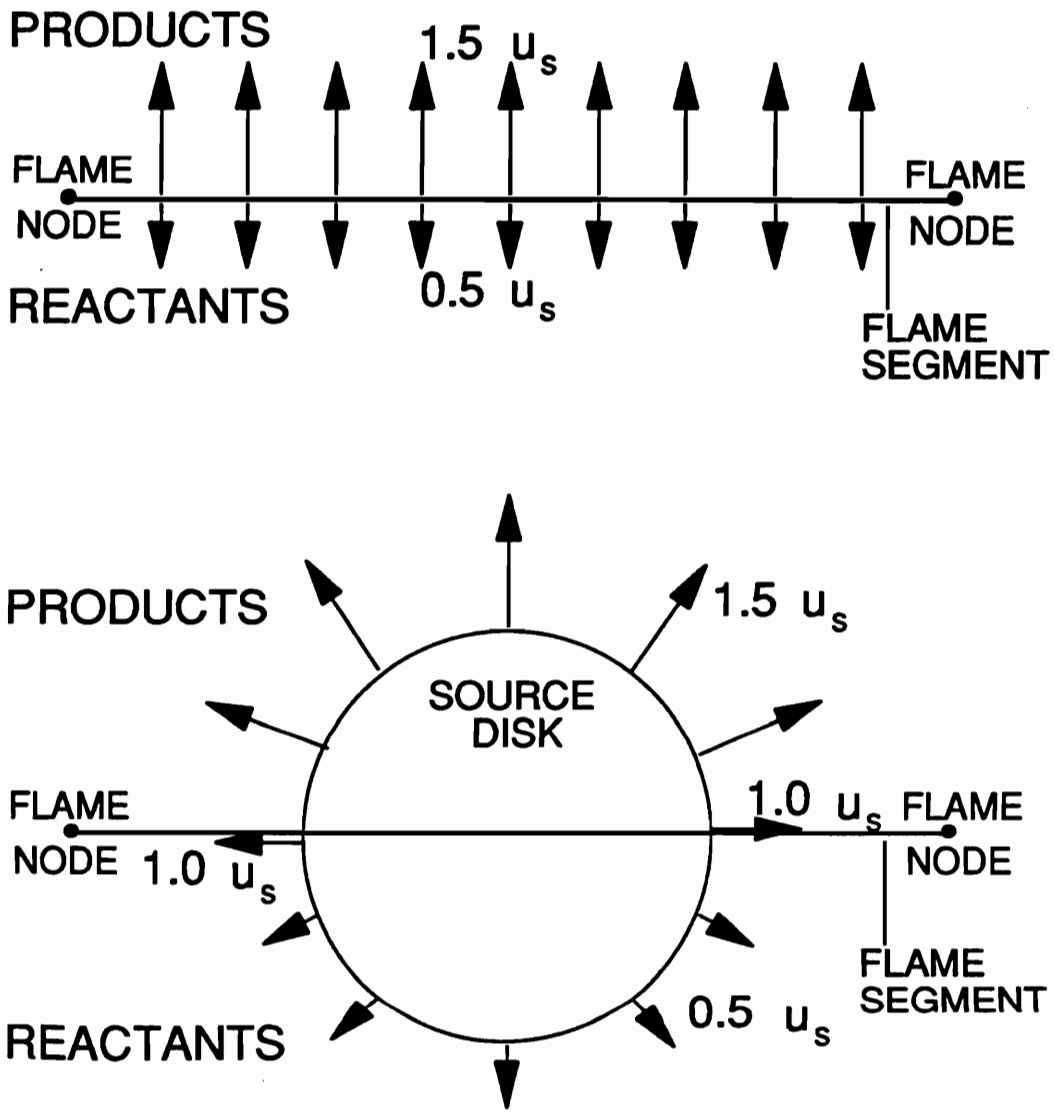

Figure 7. The modified source model: The flame segment discharges differentially into the upstream and downstream sides. For points located on the flame sheet, a strength of $1.0u_s$ is used as the average between the upstream and the downstream strengths.

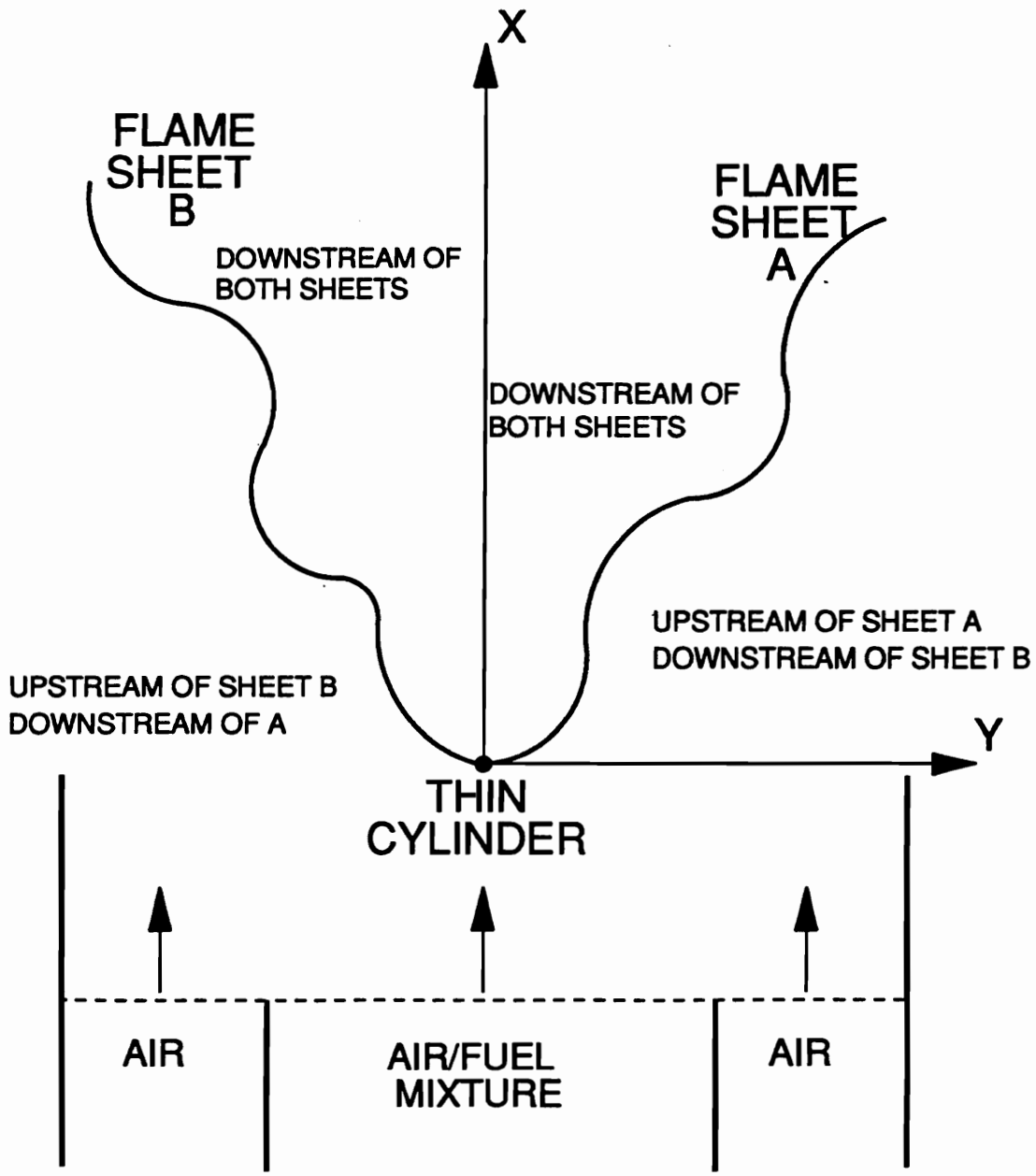

Figure 8. Rules to determine the relative position of a region w.r.t. flame sheets: Source strength on the downstream (products) side is greater than that on the upstream (reactants) side

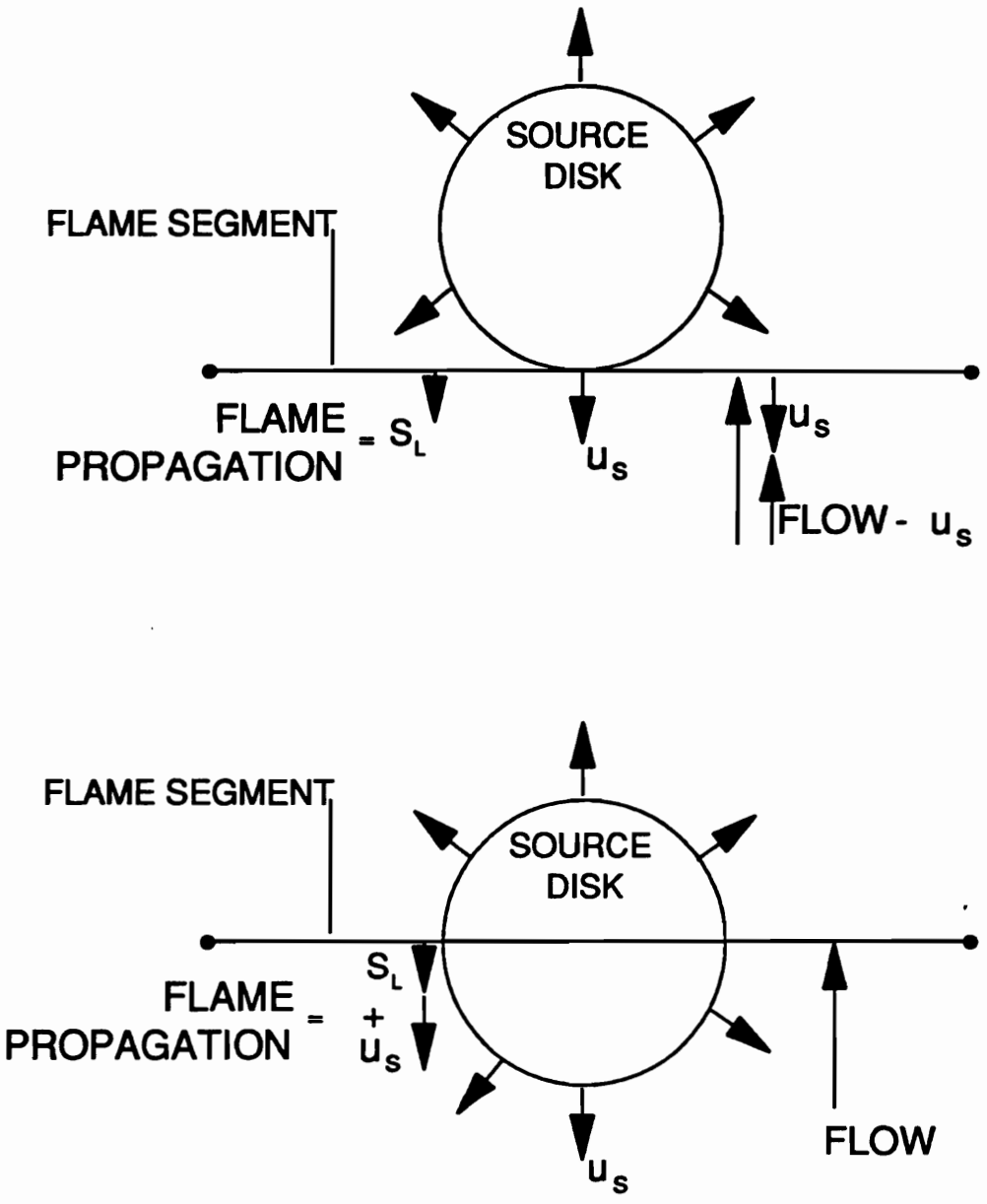

Figure 9. Two methods of accounting for flame speed: Methods (a) and (b) produce identical numerical results. Method (a) is physically more sensible than (b), while (b) is easier for programming. u_s

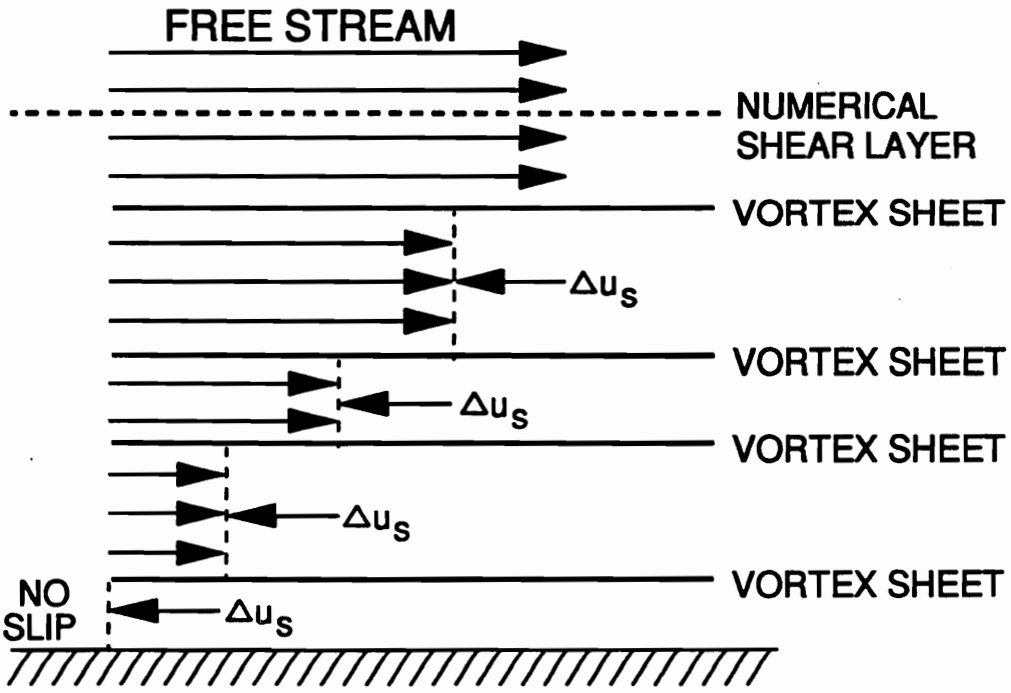

Figure 10. Vortex sheets stacked like cards across the numerical shear layer: A velocity jump of $-\Delta u$ is experienced when going from the top side to the under side of a vortex sheet. The accumulated velocity jumps are designed to bring the velocity at solid surface to zero.

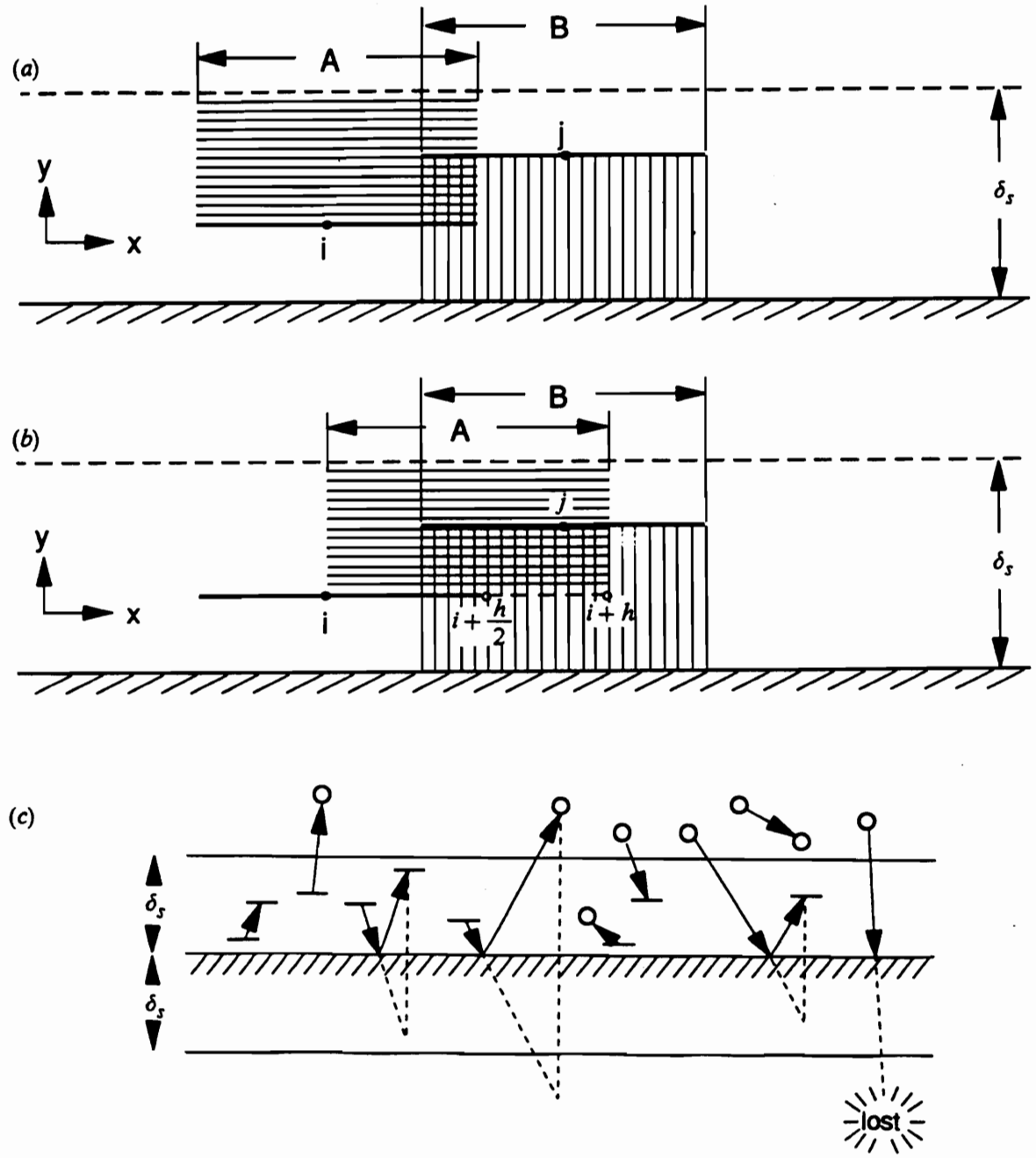

Figure 11. The zones of interdependence: (a) Cross hatching is sheet *j's* zone of influence over sheet *i* when computing velocity at the midpoint of *i*. (b) Cross hatching is sheet *j's* zone of influence over sheet *i* when computing velocity at the end-point $i+\frac{h}{2}$ of sheet *i*. (c) The rules for transition between vortex sheets and vortex disks.

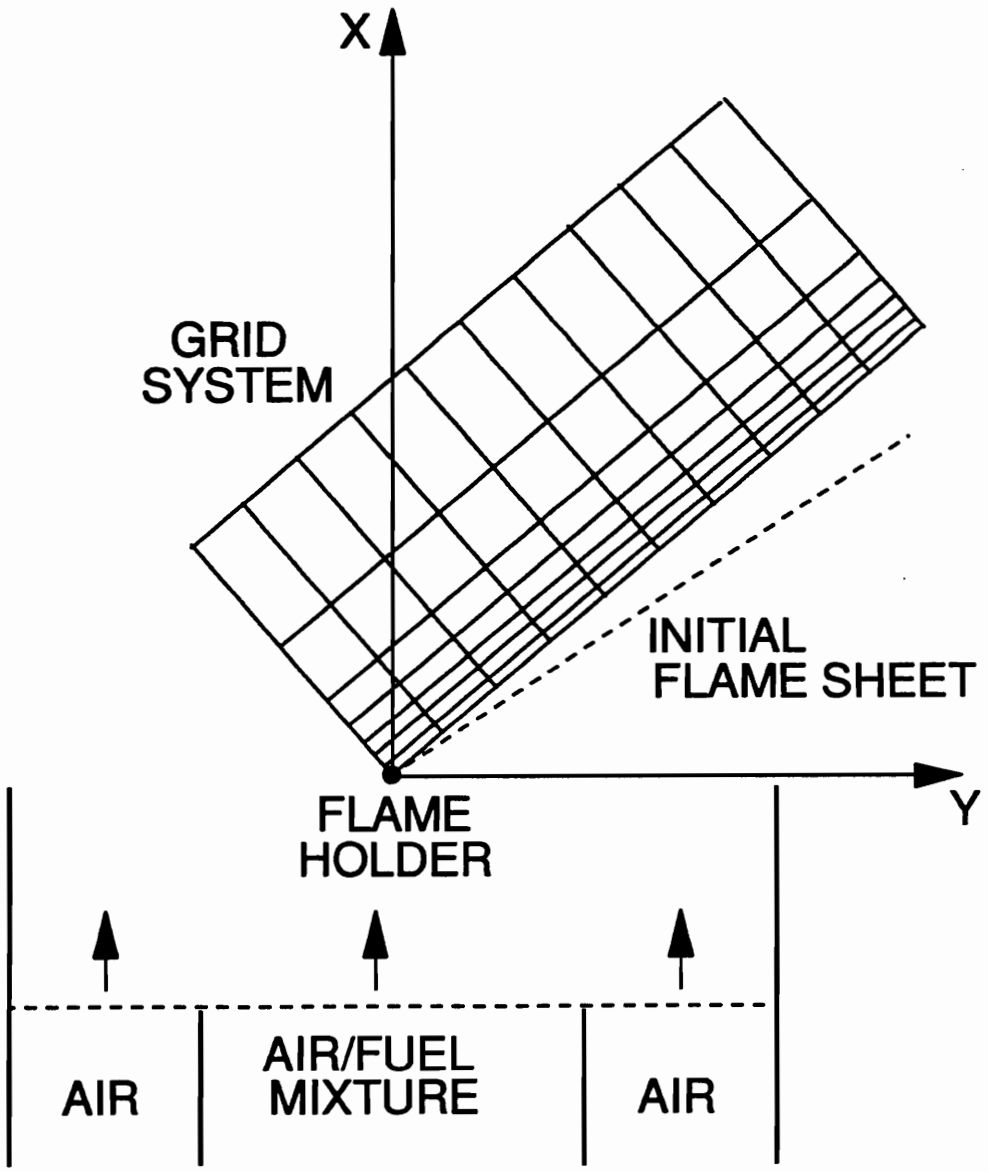

Figure 12. The grid system for reducing computation cost: The flame generated vortices are combined on each grid cell. The assumed initial flame position is shown in a dashed line

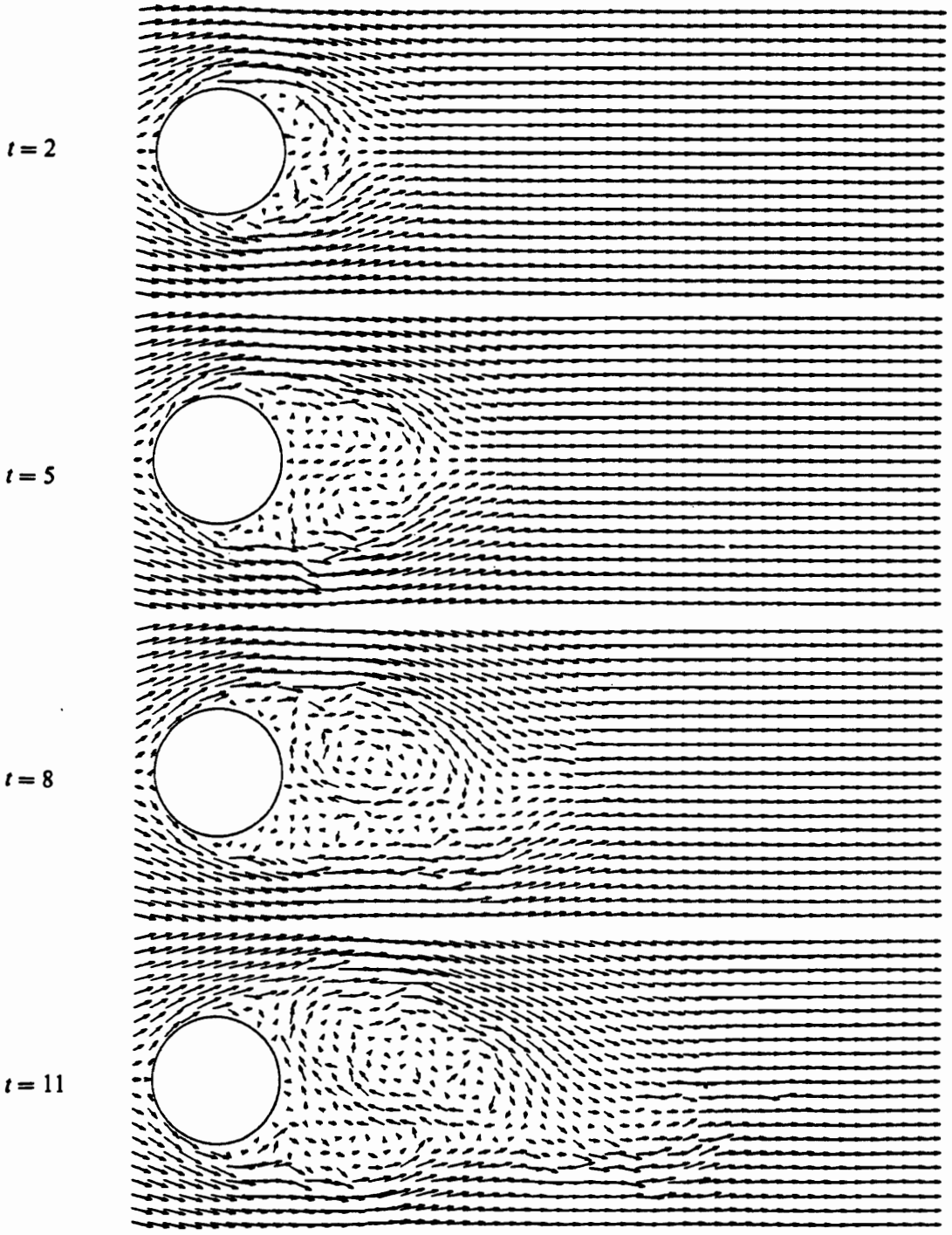

Figure 13. Flow past a 2-D circular cylinder, Re = 300: Velocity vectors are plotted at fixed sampling points.

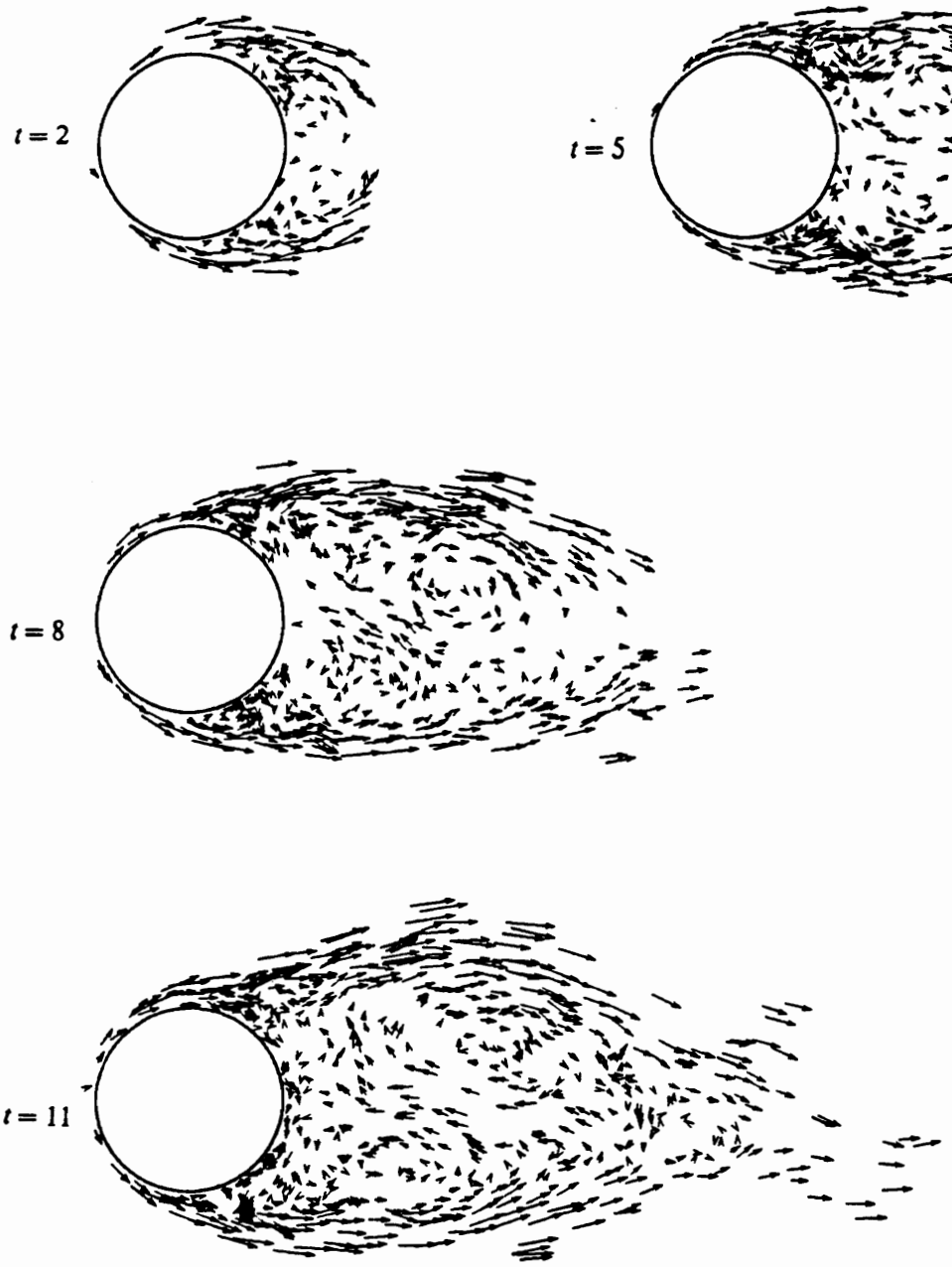

Figure 14. Flow past a 2-D circular cylinder, Re = 300: Same flow as in Fig.13, velocity vectors at locations where individual vortices are.

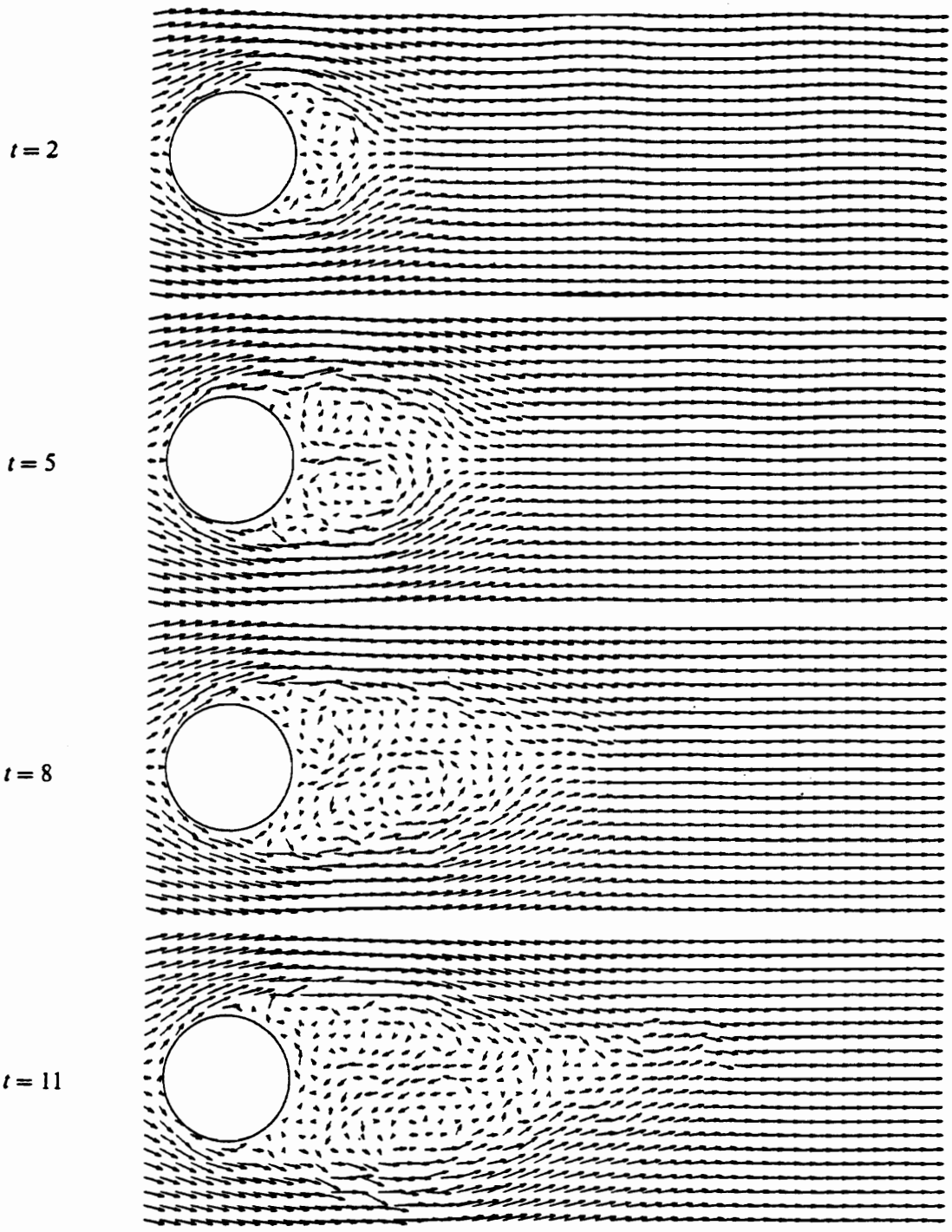

Figure 15. Flow past a 2-D circular cylinder, Re = 300: Same input parameters as in Fig.13, the effect of random walk causes different appearance and the bottom eddy sheds first.

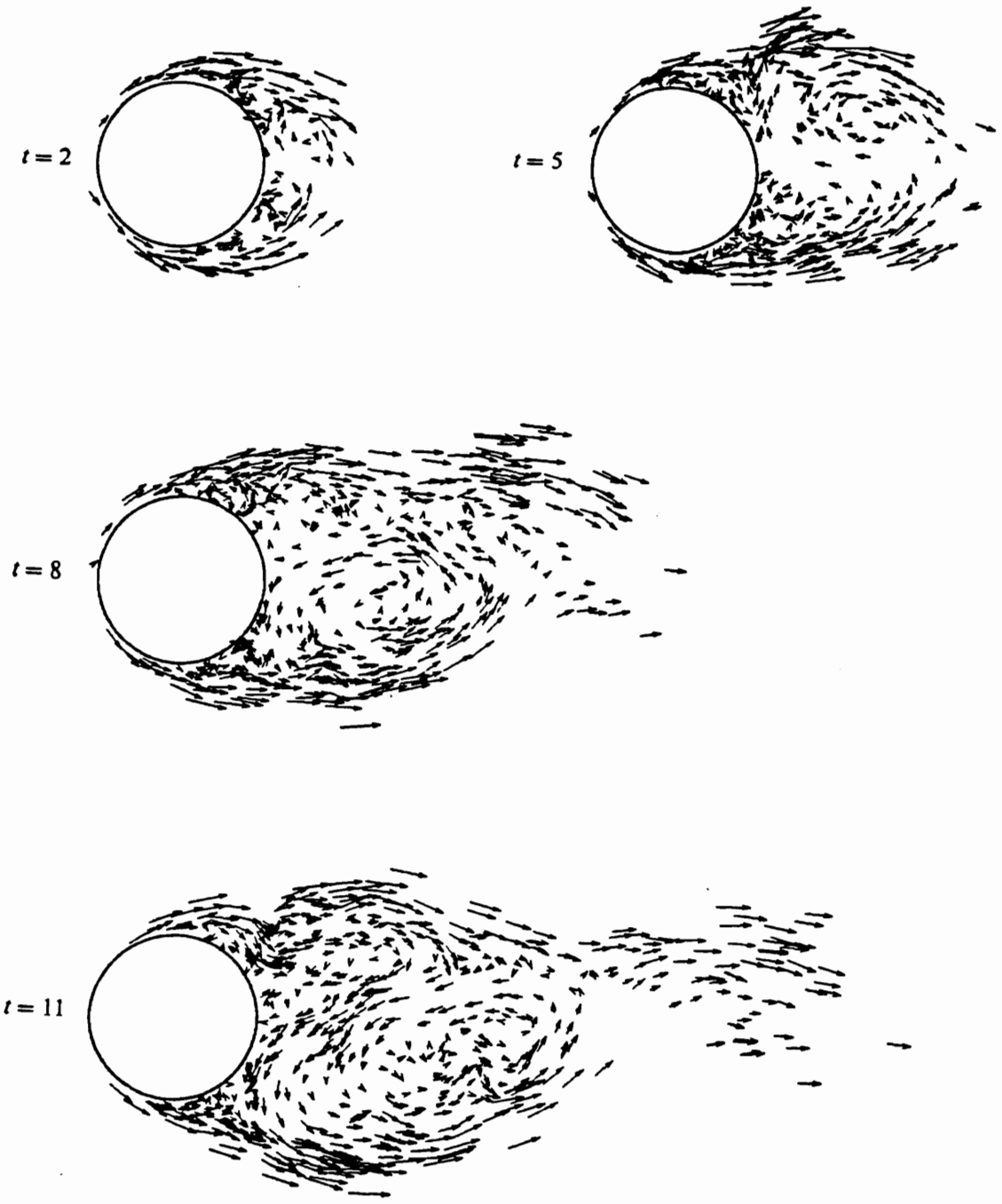

Figure 16. Flow past a 2-D circular cylinder, Re = 300: Same flow as in Fig.15, velocity vectors shown at locations where individual vortices are.

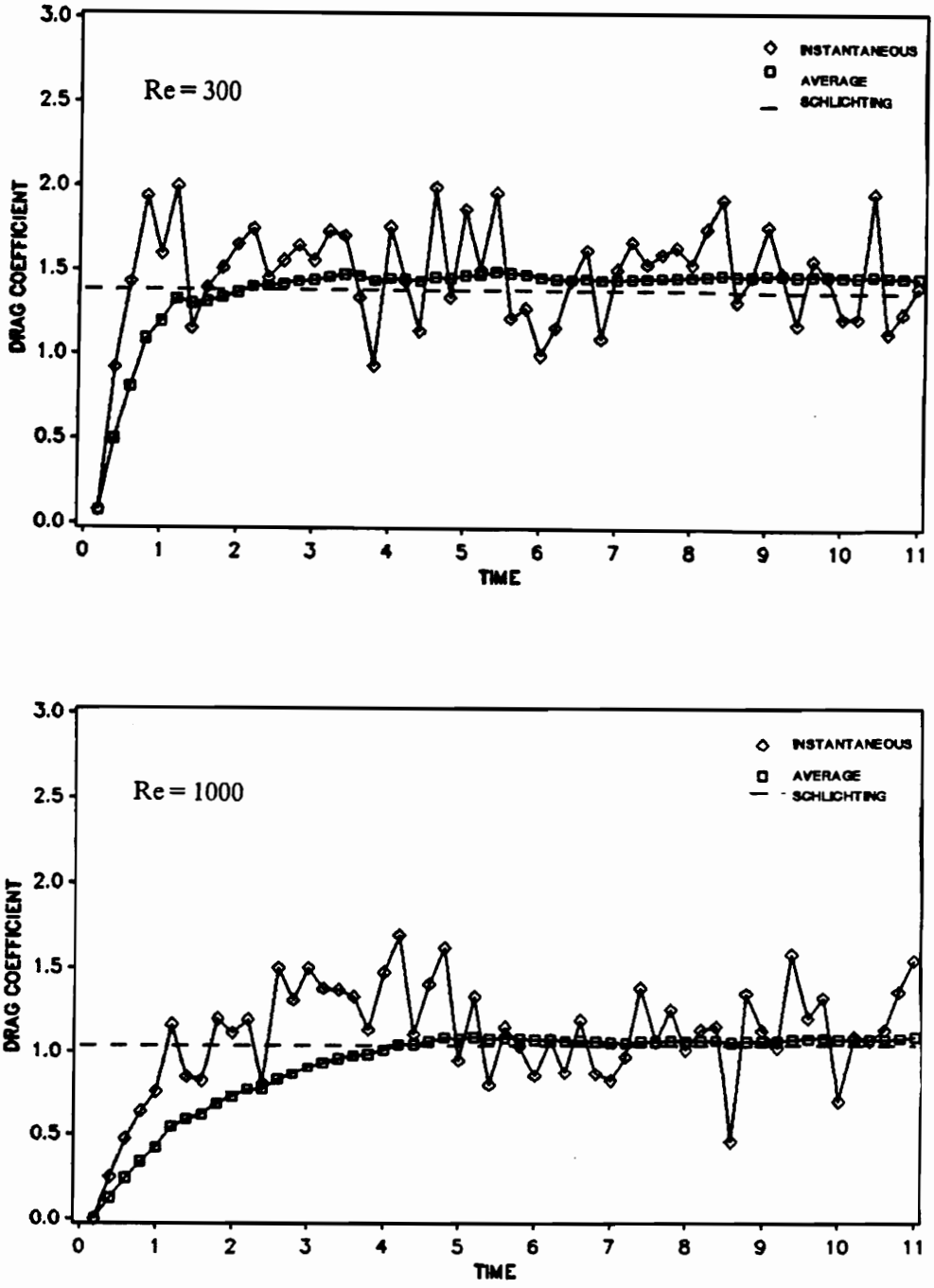

Figure 17a. Computed drag coefficients of a 2-D circular cylinder: Experimental values are 1.38 and 1.04 for $Re = 300$ and $Re = 1000$ respectively. Computed mean values are 1.47 and 1.08.

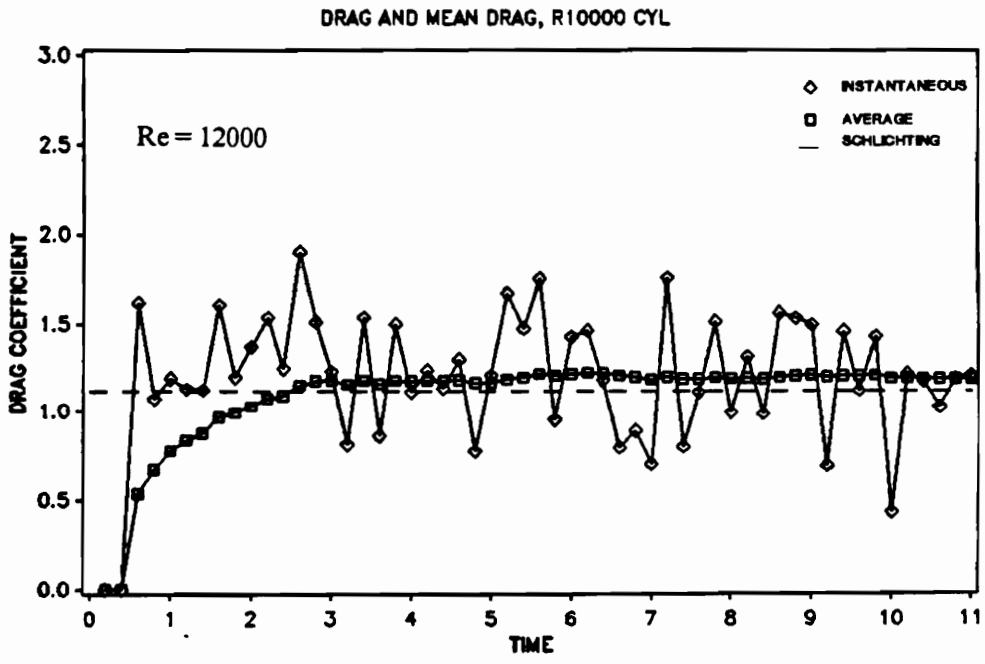

Figure 17b. Computed drag coefficient of a 2-D circular cylinder, Re = 12000: Experimental value is 1.12. Computed mean is 1.15.

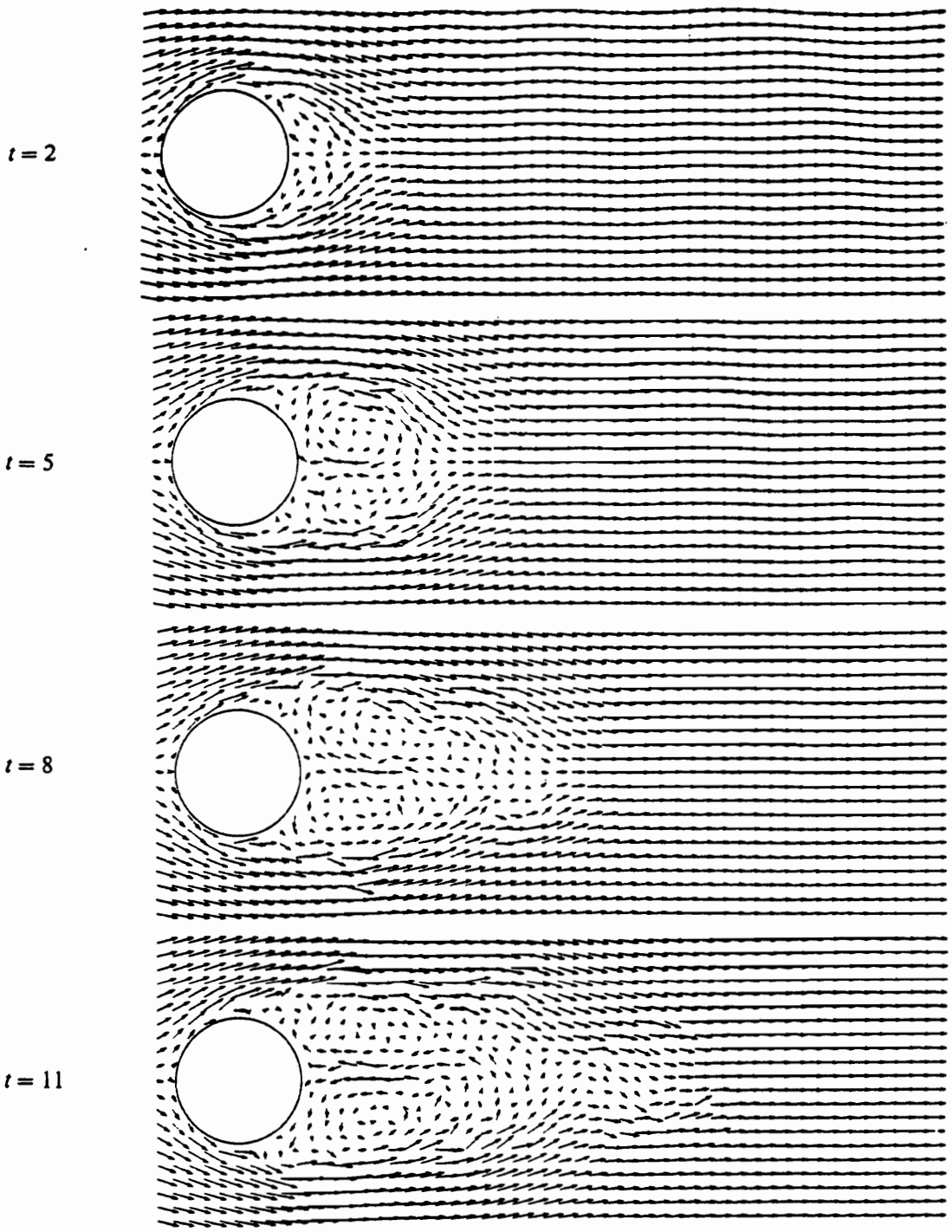

Figure 18. Flow past a circular cylinder, Re = 1000: Velocity vectors at fixed sampling points.

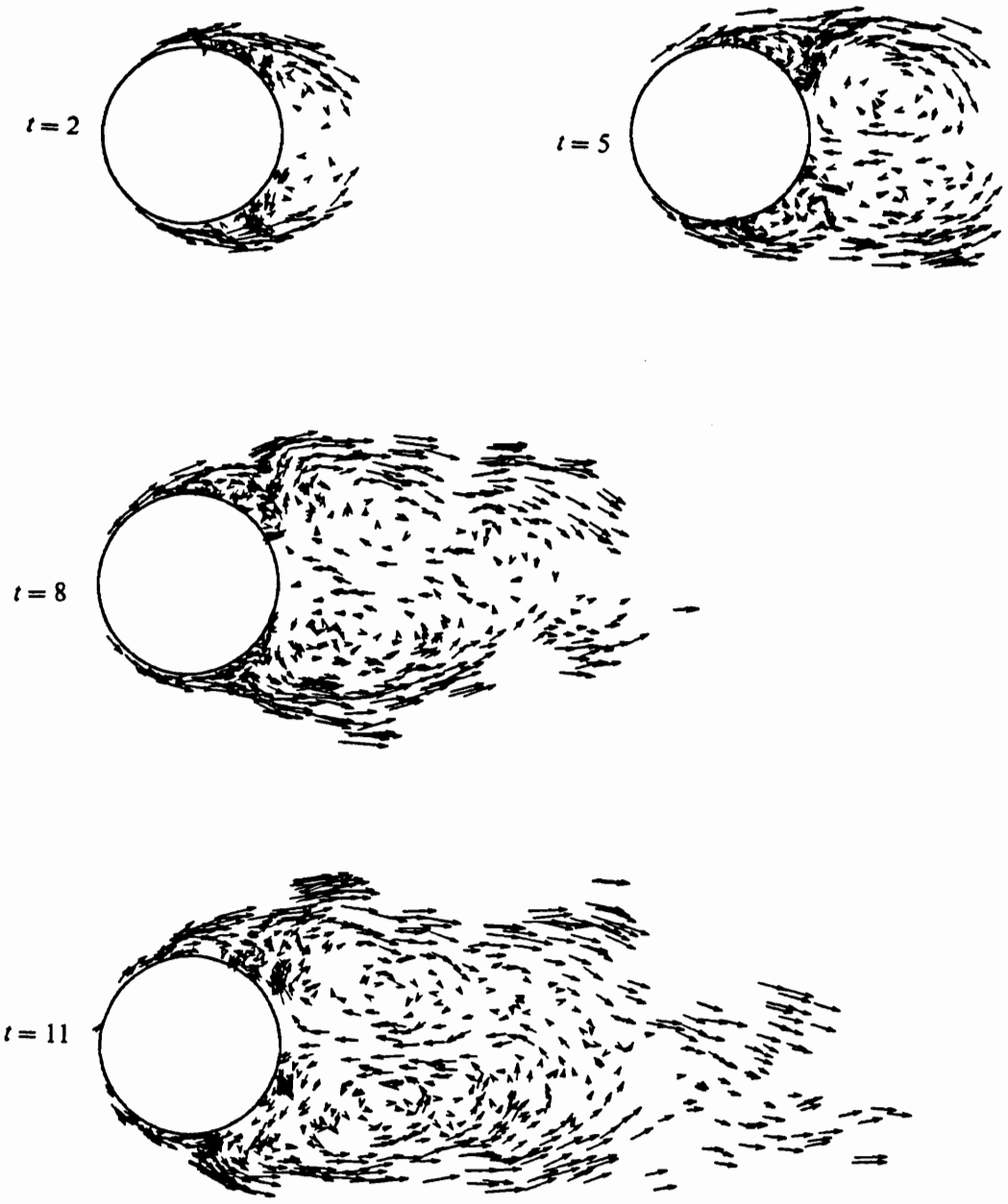

Figure 19. Flow past a circular cylinder, Re = 1000: Velocity vectors at locations where individual vortices are.

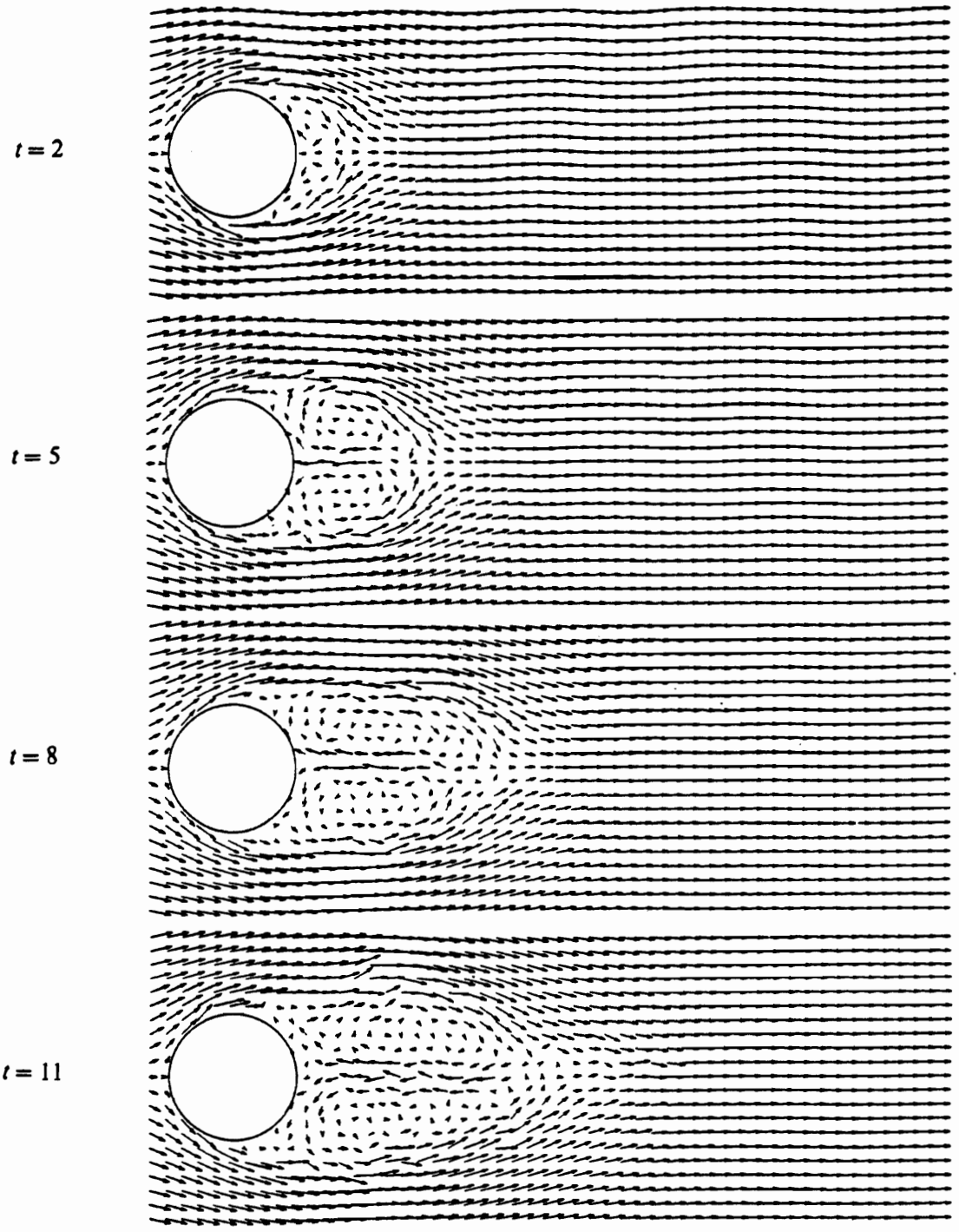

Figure 20. Flow past a circular cylinder, Re = 12000: Velocity vectors at fixed sampling points.

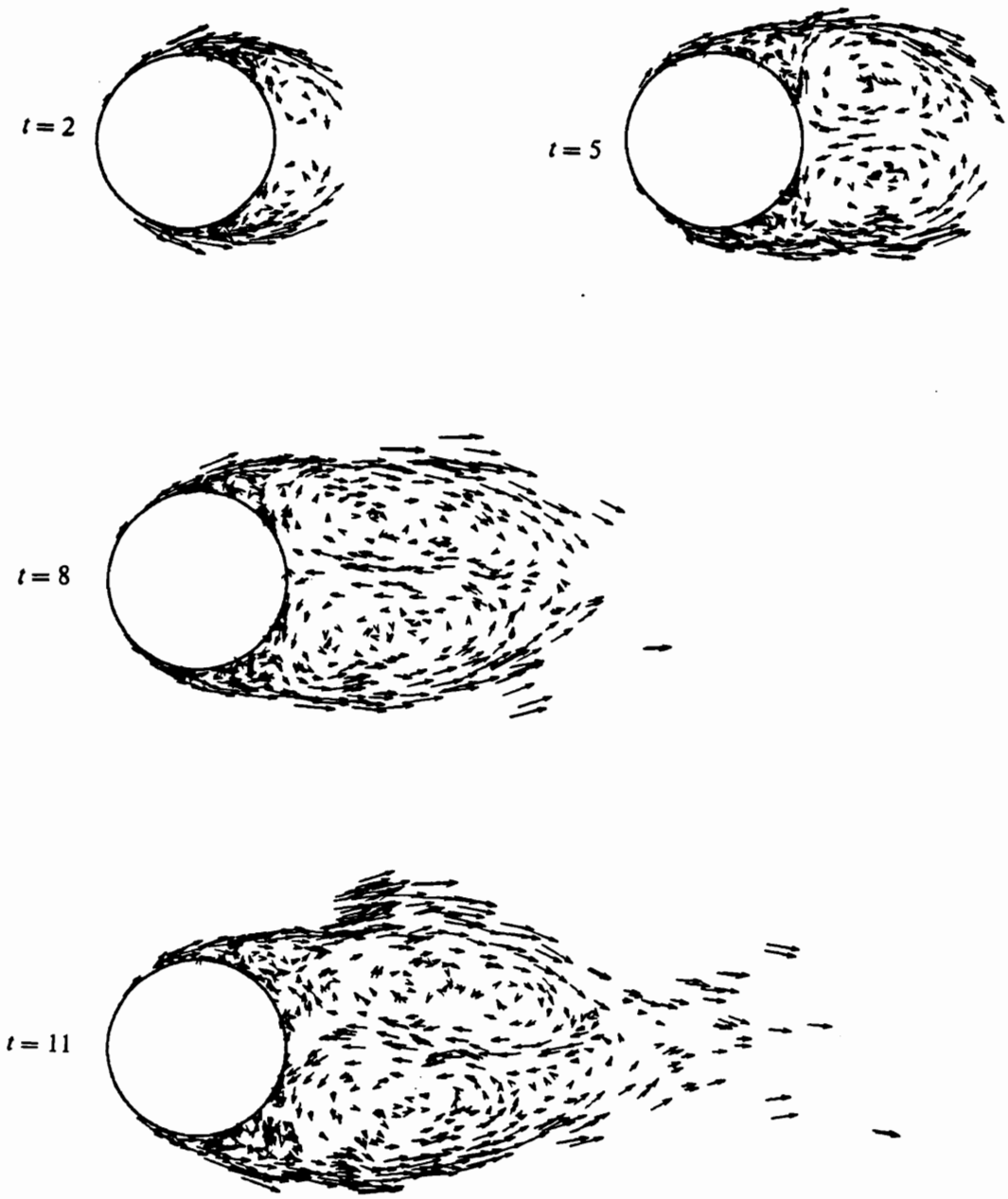

Figure 21. Flow past a circular cylinder, Re = 12000: Velocity vectors at locations where individual vortices are.

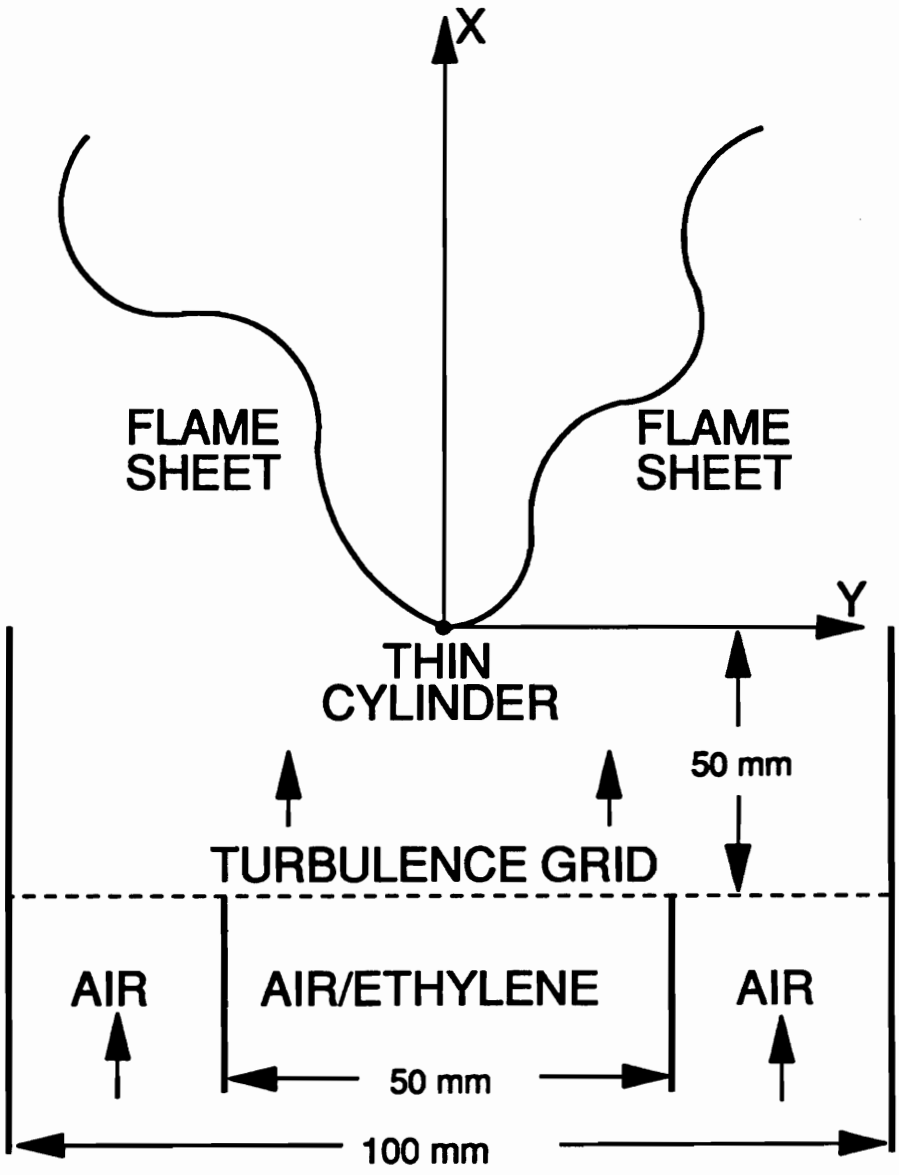

Figure 22. General setup of Cheng's experiment

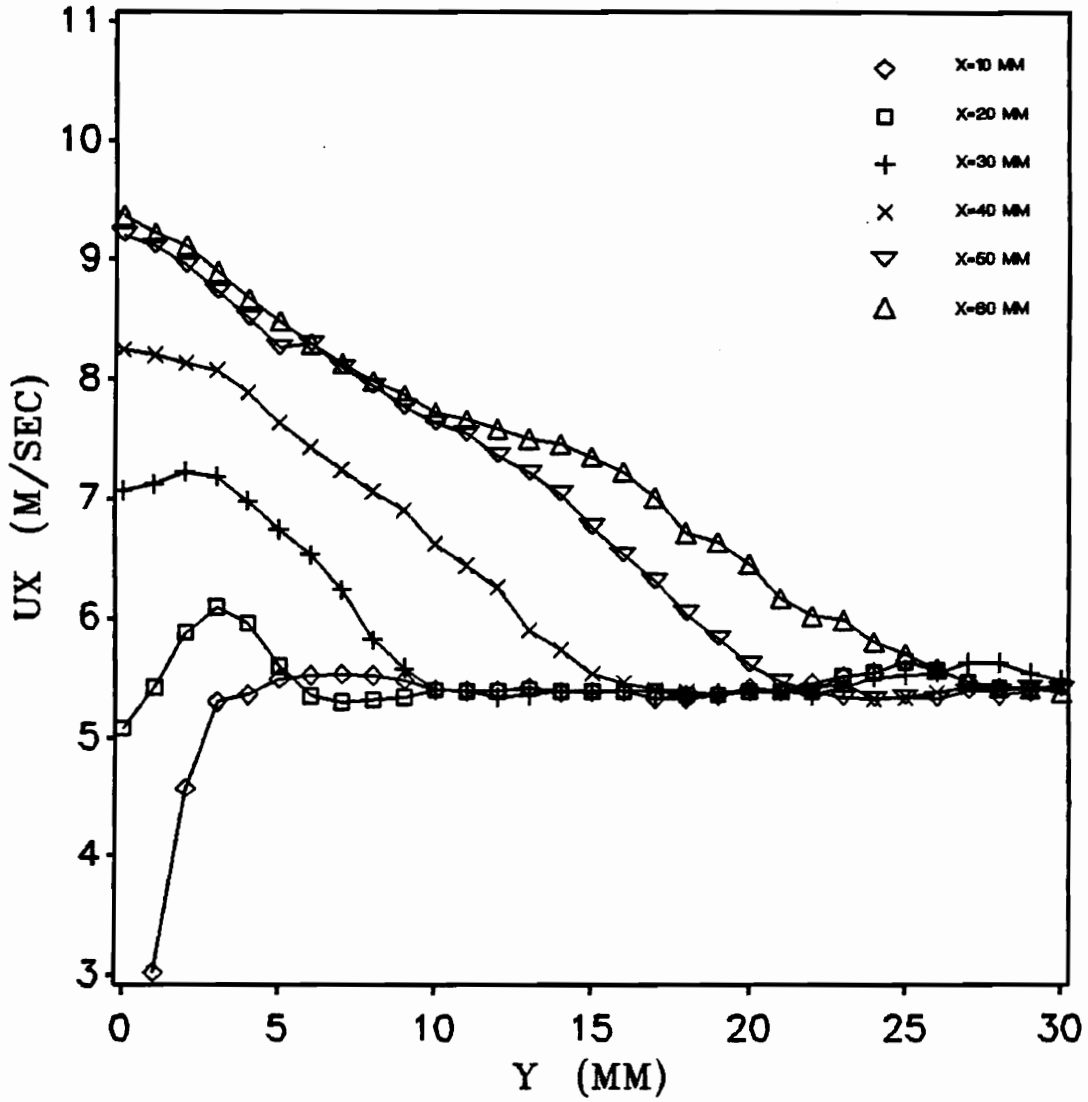

Figure 23. Ux velocity profiles measured by Cheng.

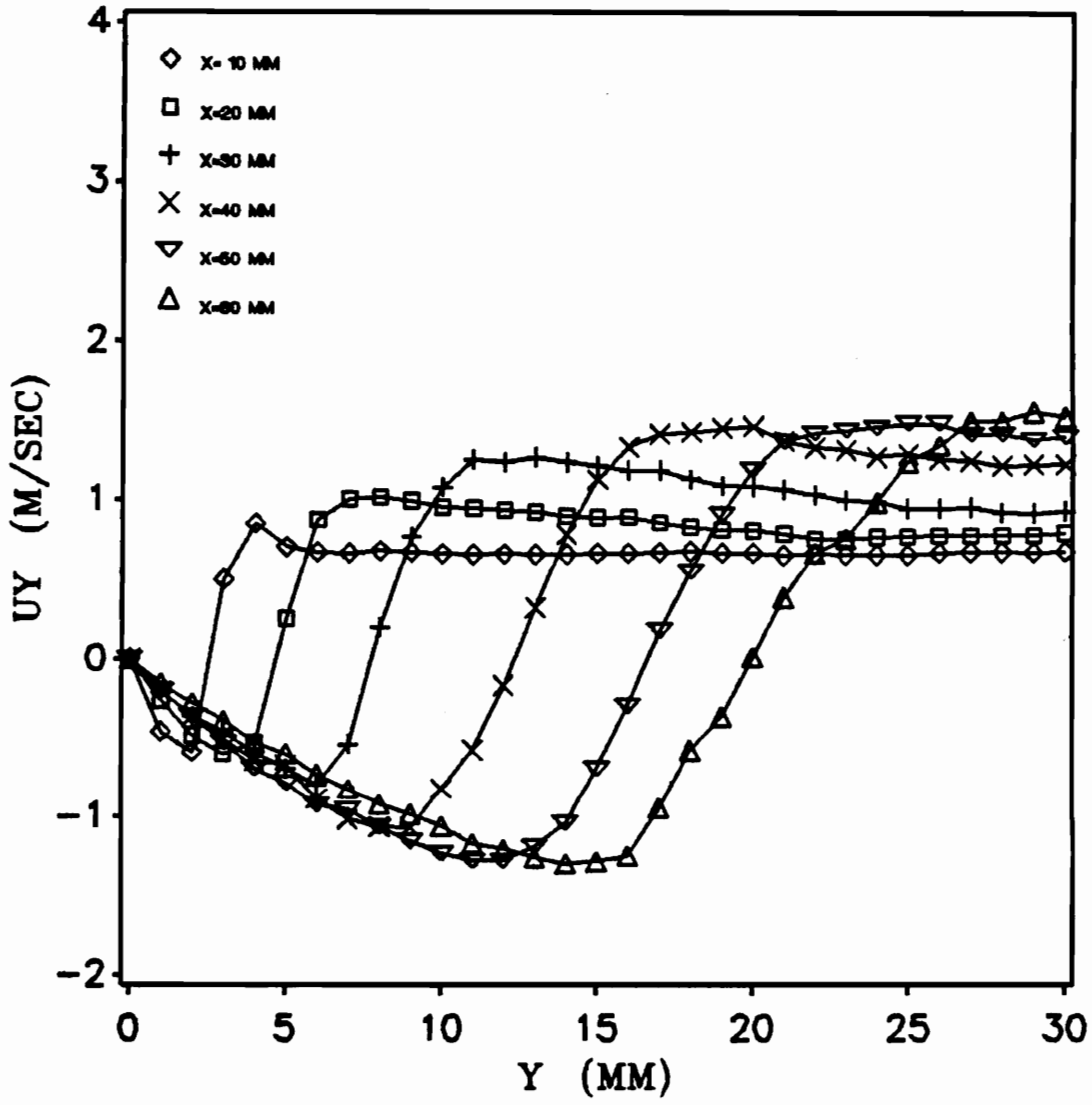

Figure 24. Uy velocity profiles measured by Cheng.

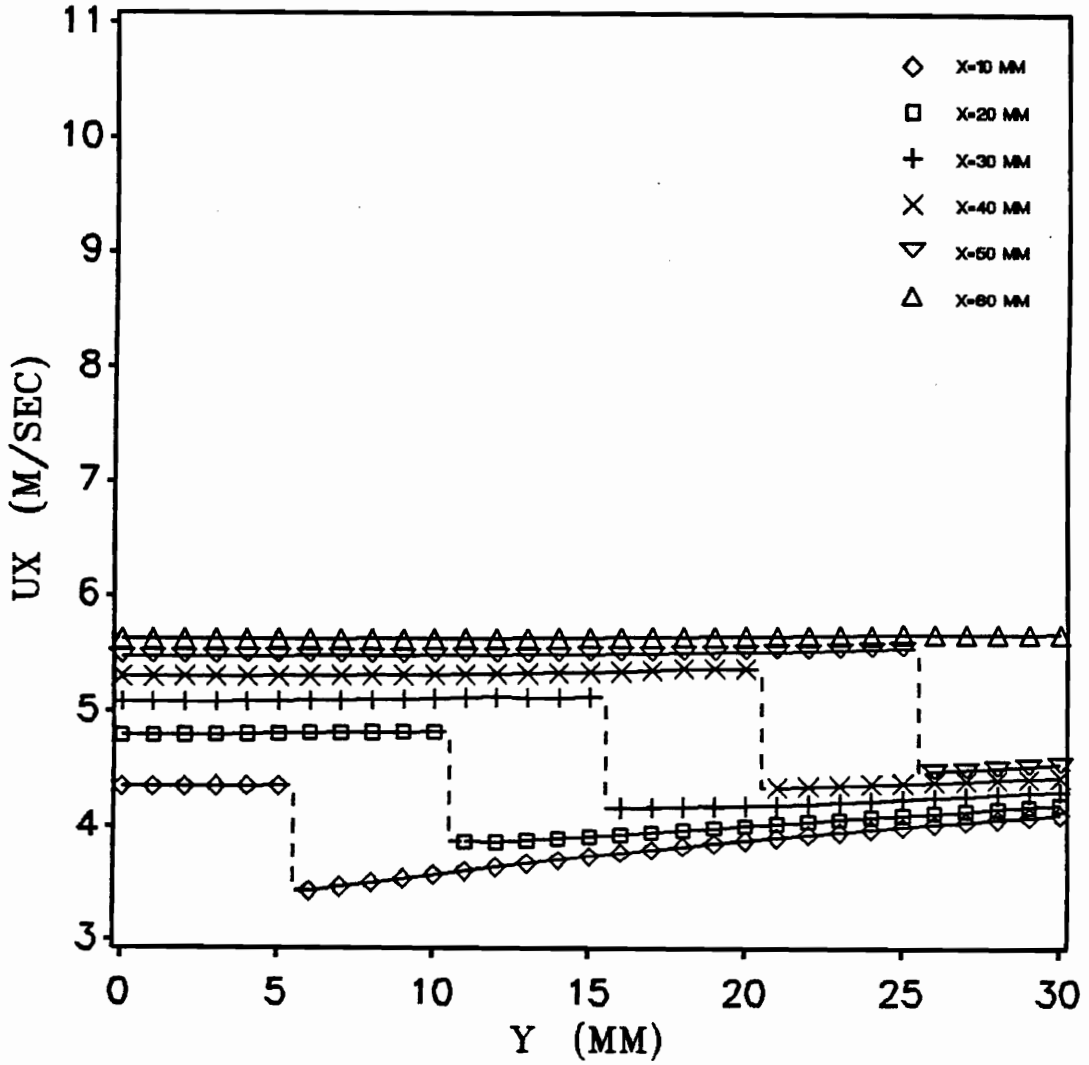

Figure 25. Ux profiles computed with the existing source model: Note that the velocity jump for $x = 60\ mm$ is outside the bound of this figure because the computed flame angle is too large.

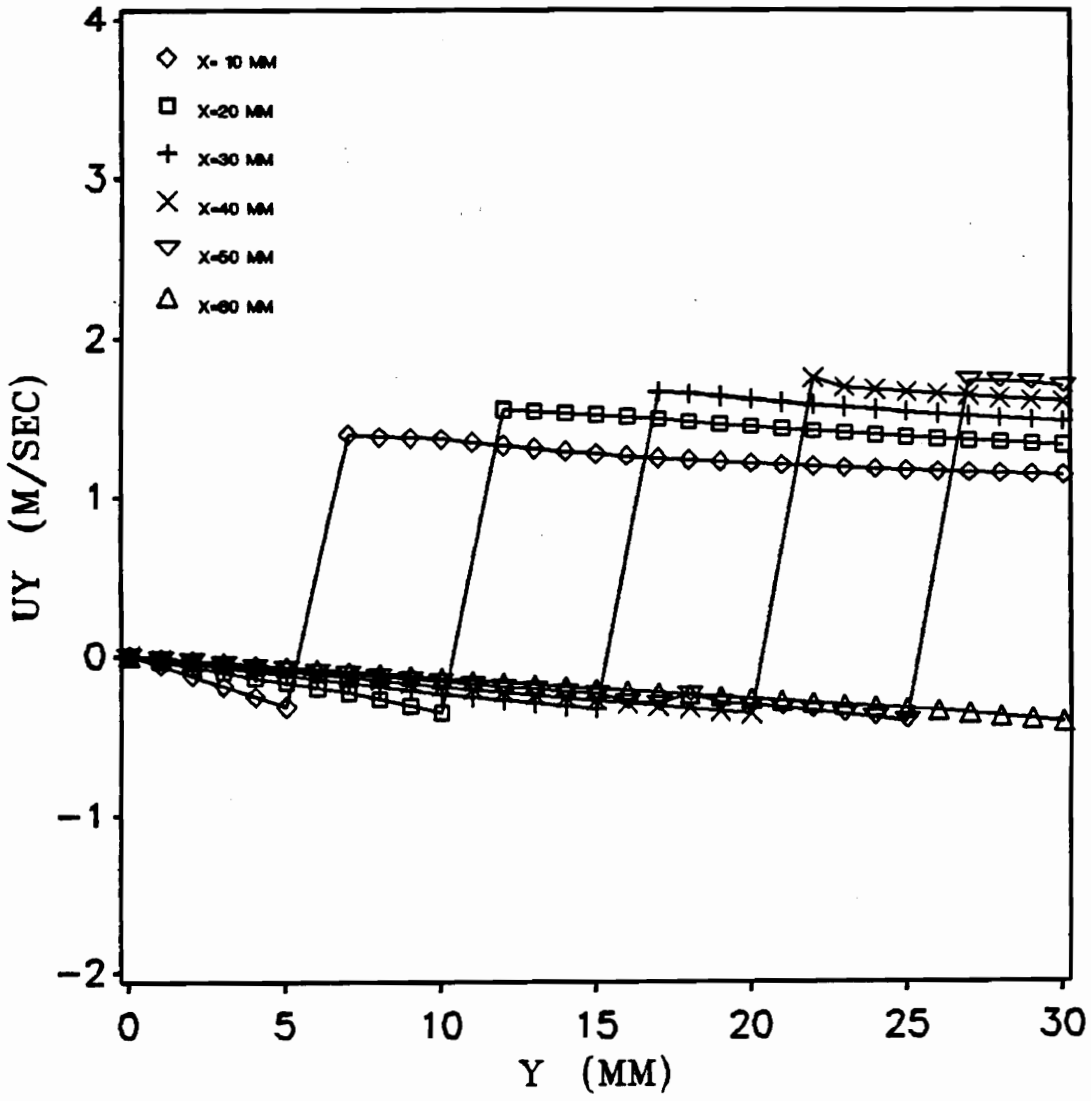

Figure 26. Uy profiles computed with the existing source model: As in Fig.25, the velocity jump for $x = 60$ *mm* is also ouside the bound of this figure.

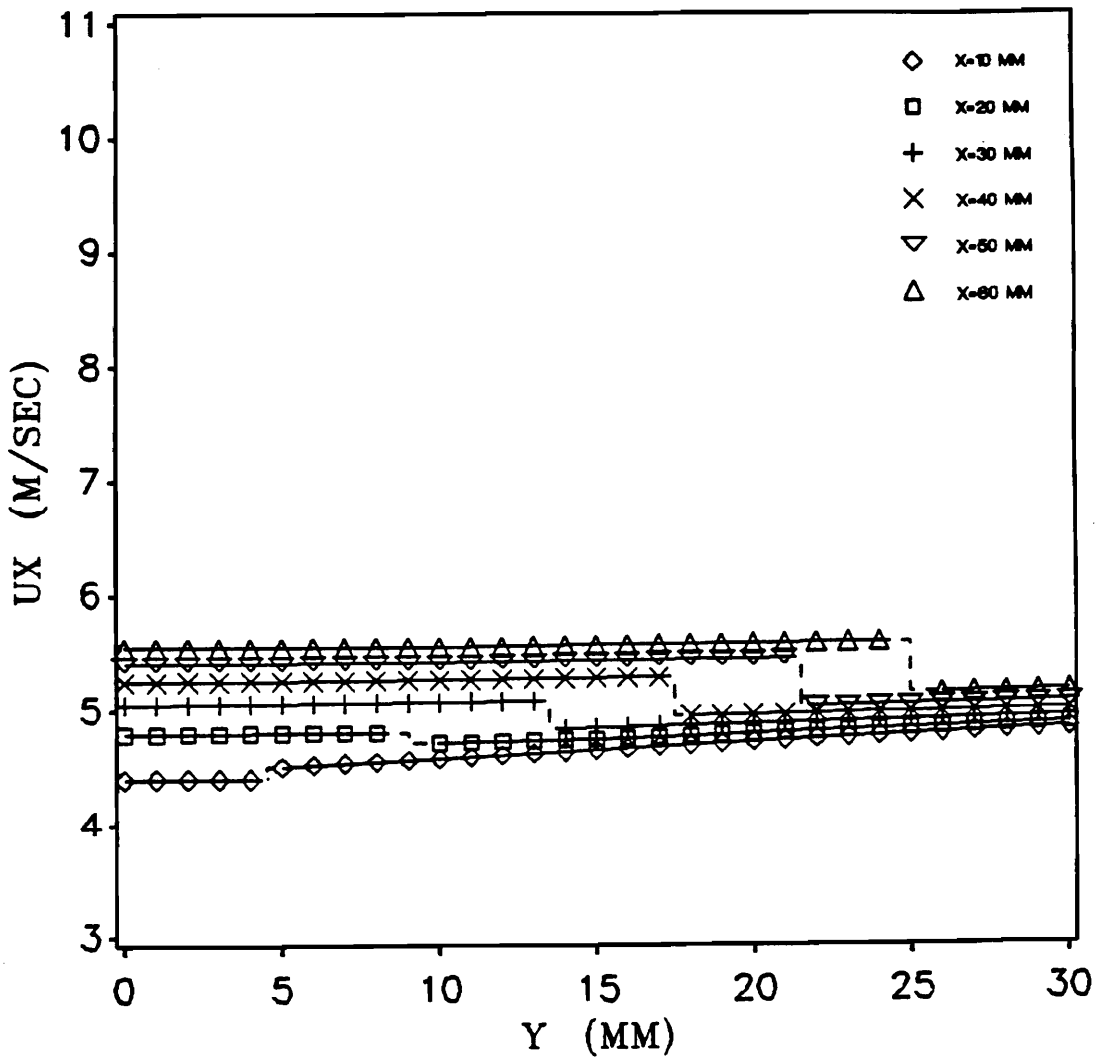

Figure 27. Ux profiles computed with the modified source model: All velocity jumps occurs at locations closer to the axis of symmetry and a much smaller computed flame angle is infered.

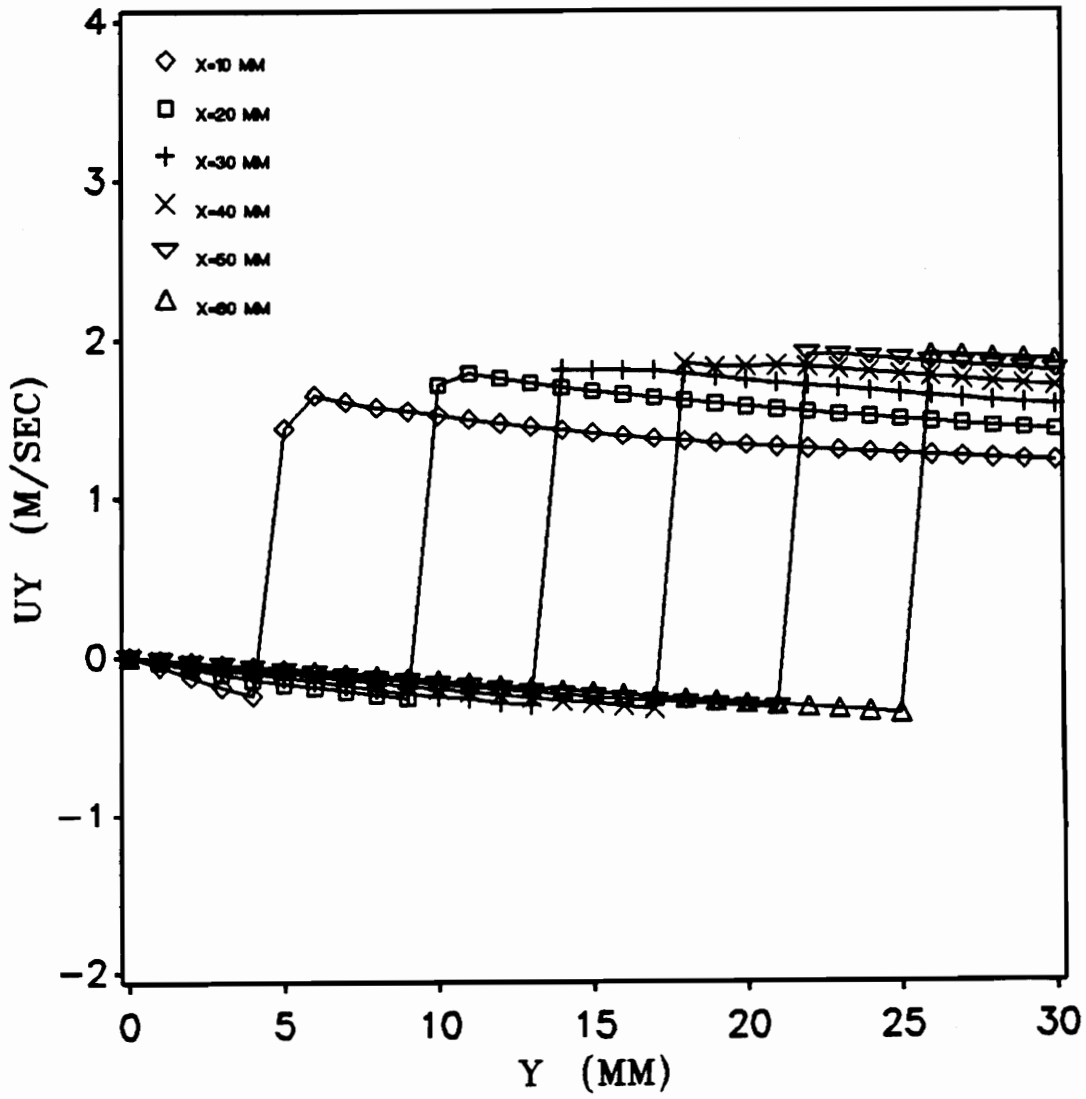

Figure 28. Uy profiles computed with the modified source model.: Positive U_y before the flame means the flow is deflected away from the axis of symmetry, negative U_y behind the flame means the flow is turned toward the above axis.

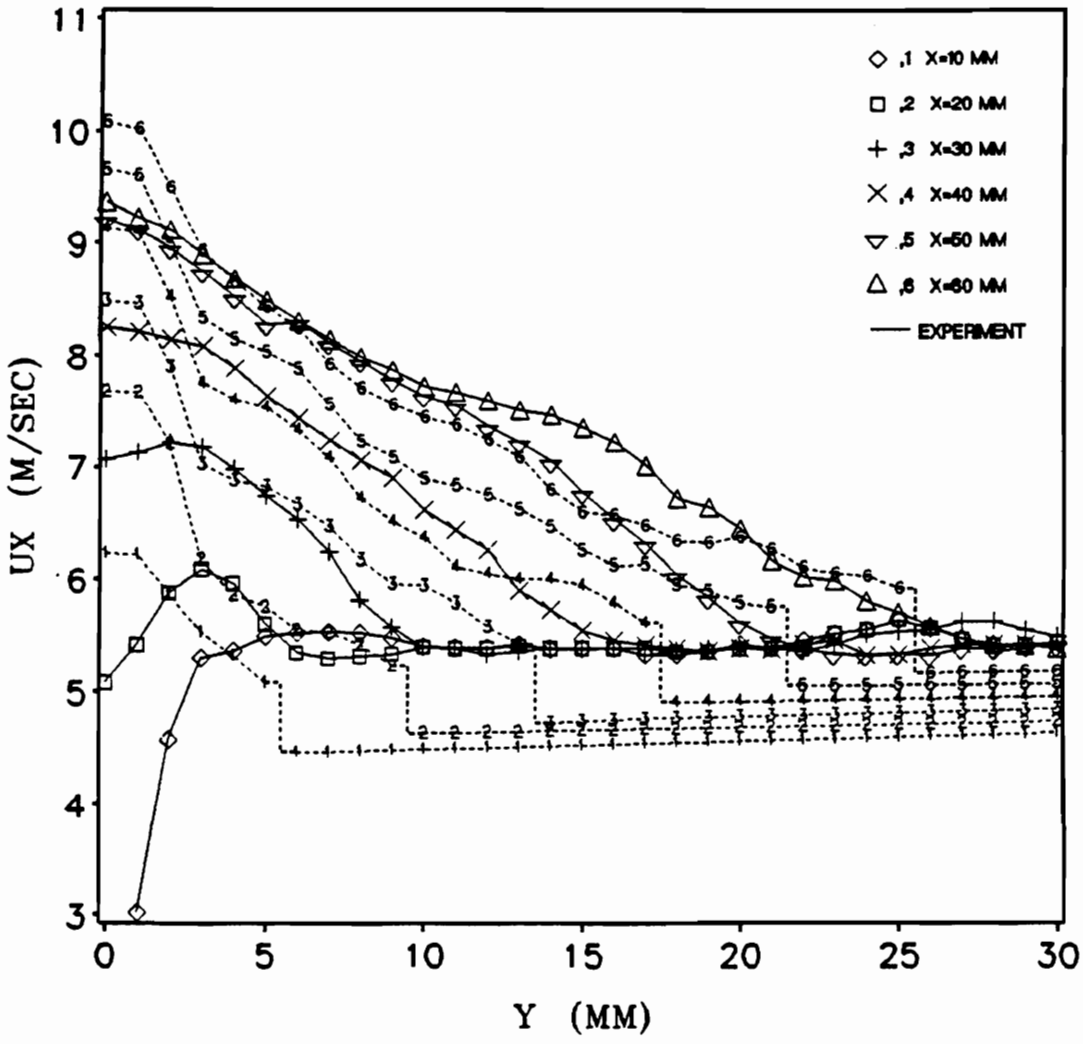

Figure 29. Computed mean Ux profiles: The existing source model with flame vorticity included. Note that U_x increases more steeply near the X-axis.

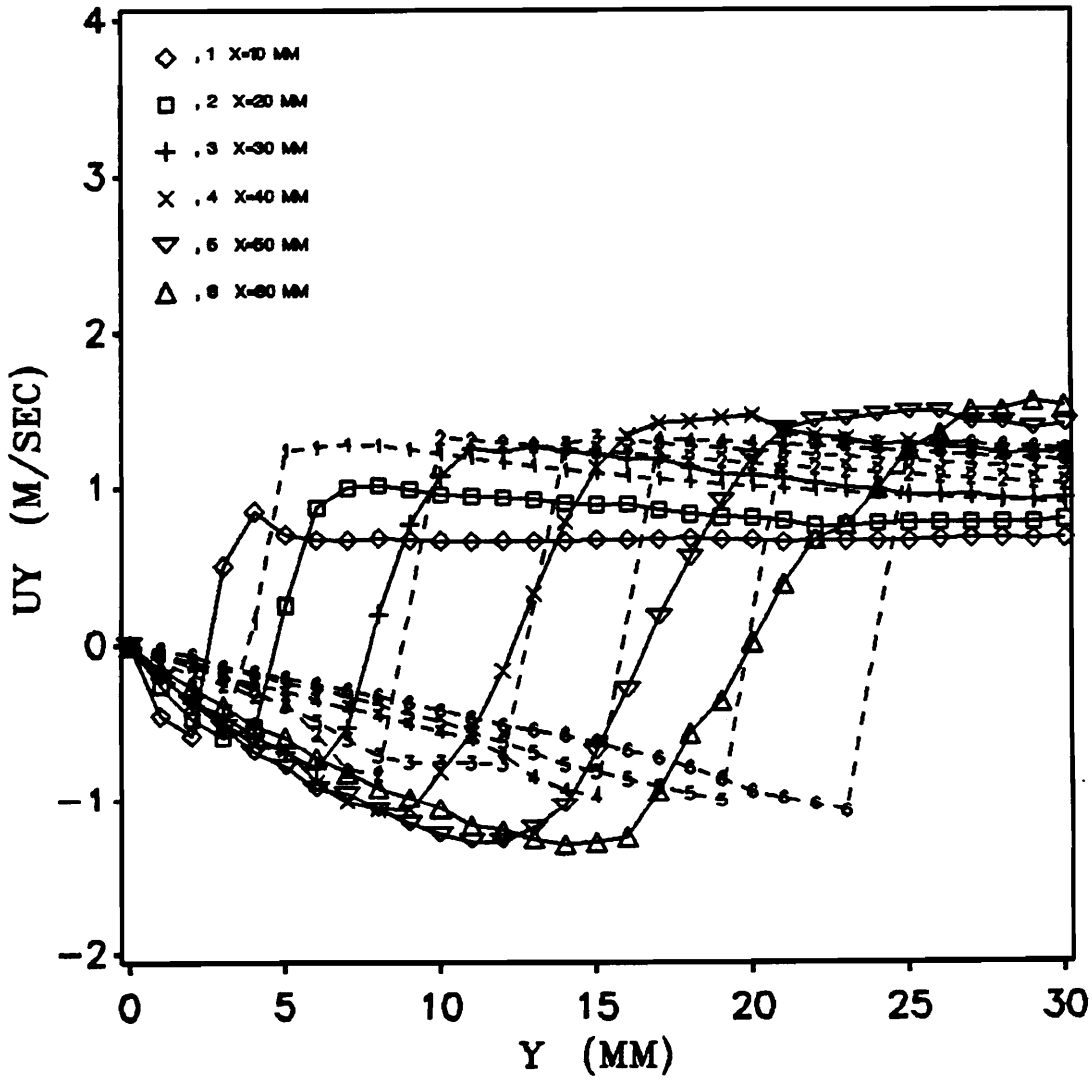

Figure 30. Computed Uy profiles: The existing source model with flame vorticity included.

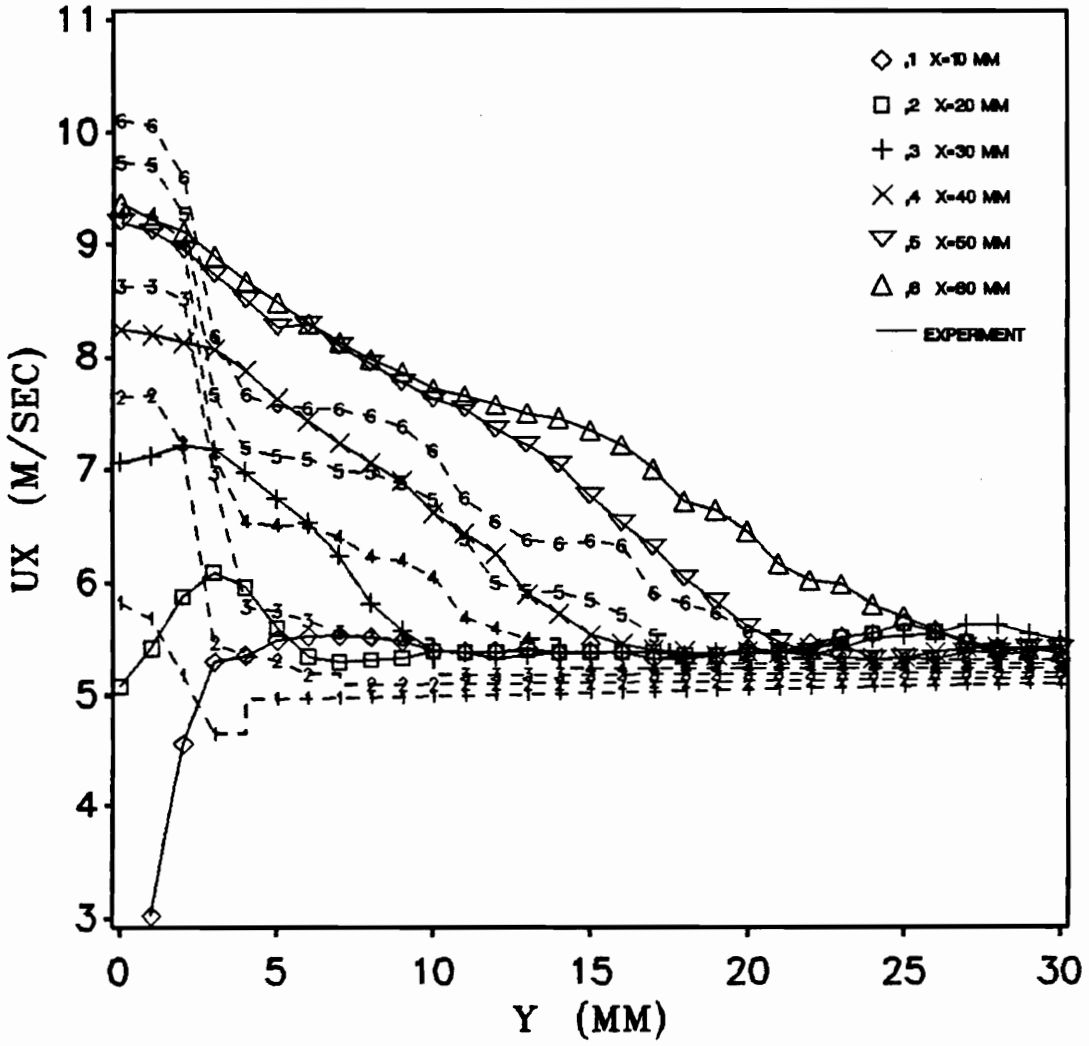

Figure 31. Computed Ux profiles: The modified source model with flame vorticity included.

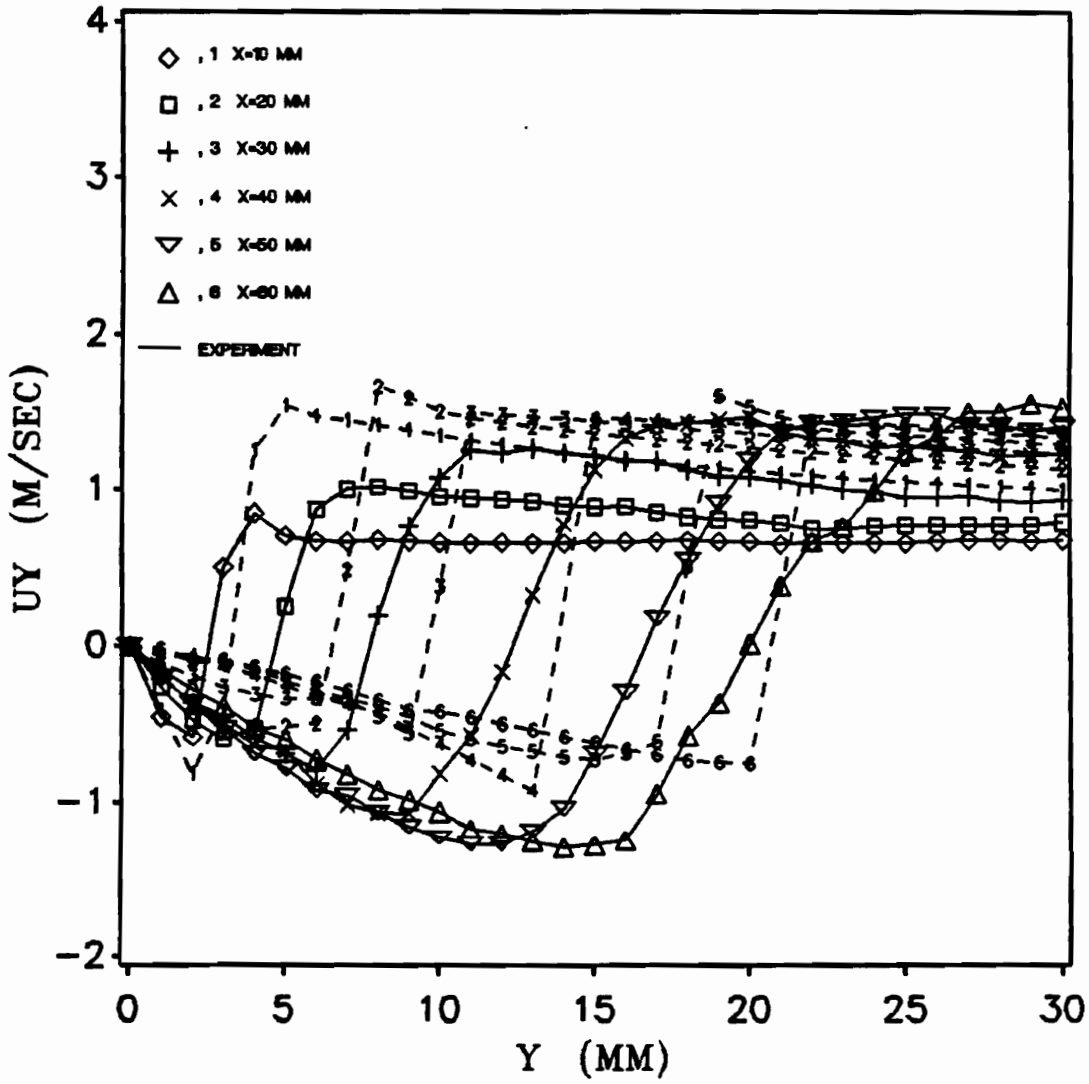

Figure 32. Computed Uy profiles: The modified source model with flame vorticity included. The upstream/downstream source discharge velocity ratio is 0.25/0.75.

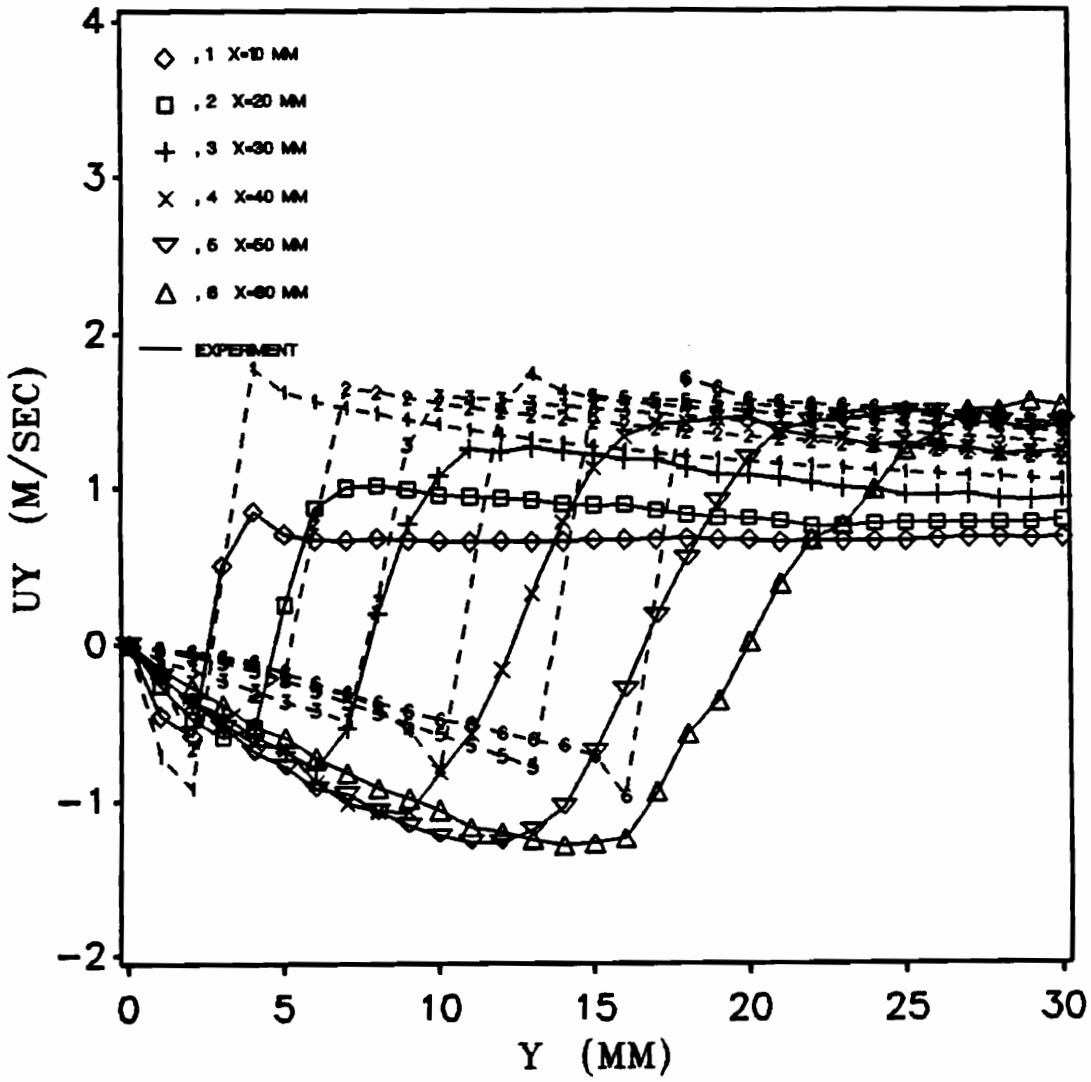

Figure 33. Computed Uy profiles: The modified source model with flame vorticity included. The upstream/downstream discharge velocity ratio is 0.10/0.90.

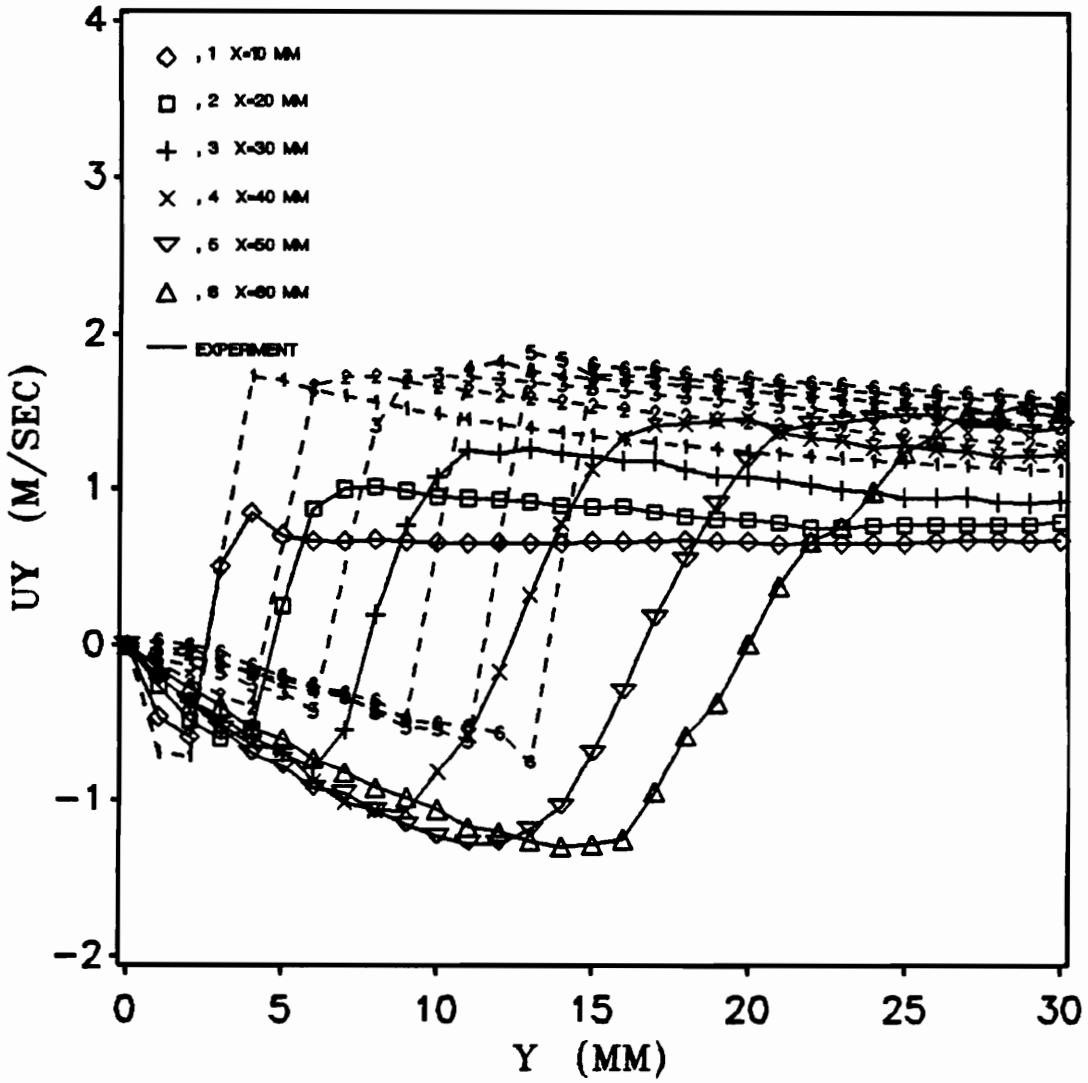

Figure 34. Computed Uy profiles: The modified source model with flame vorticity included. The upstream/downstream discharge velocity ratio is 0.00/1.00.

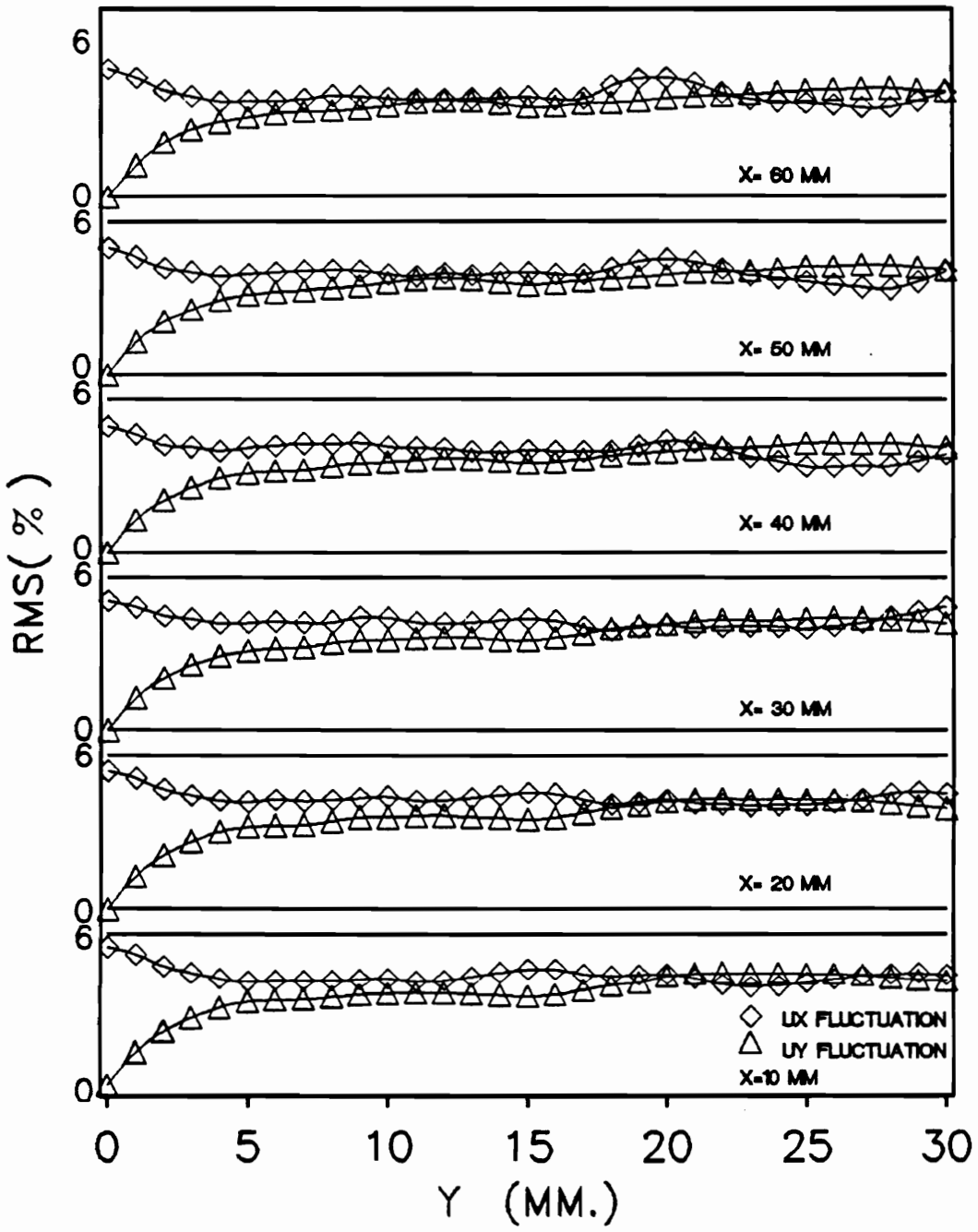

Figure 35. Computed R.M.S. fluctuations of simulated turbulence

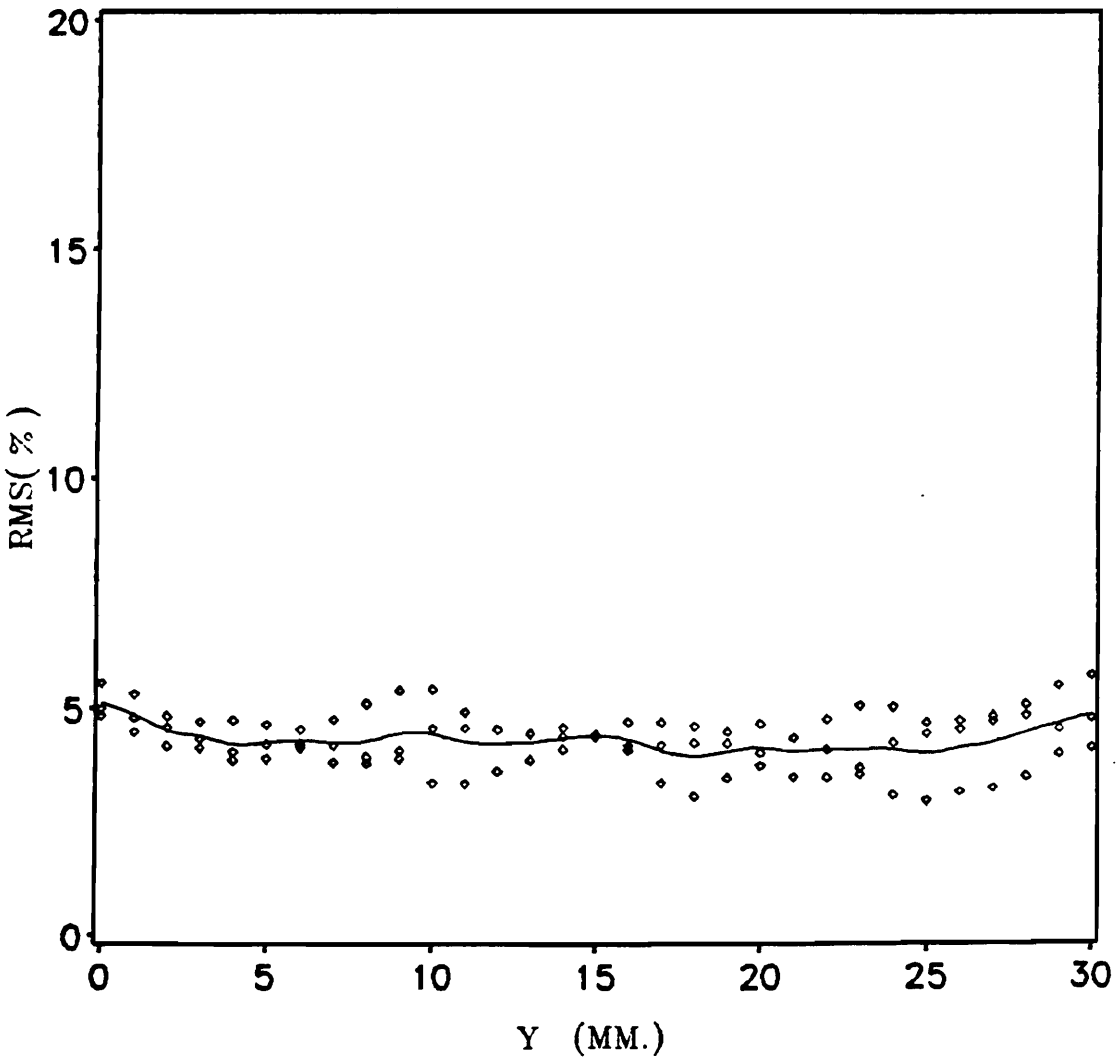

Figure 36. Ensemble averages and their mean values: Fluctuations in U_x at $x = 30mm$.

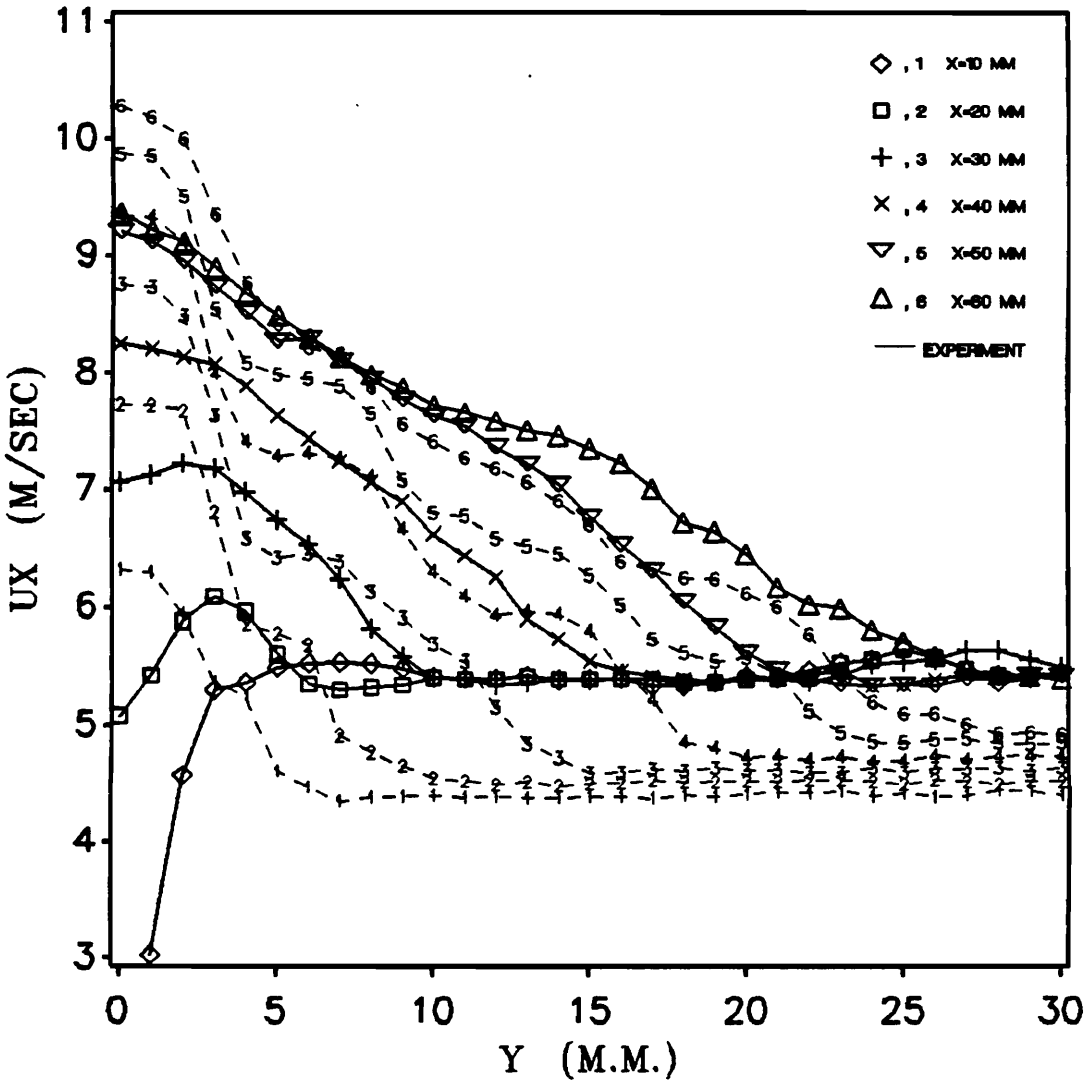

Figure 37. Computed turbulent Ux profiles: The existing source model with flame vorticity and simulated turbulence.

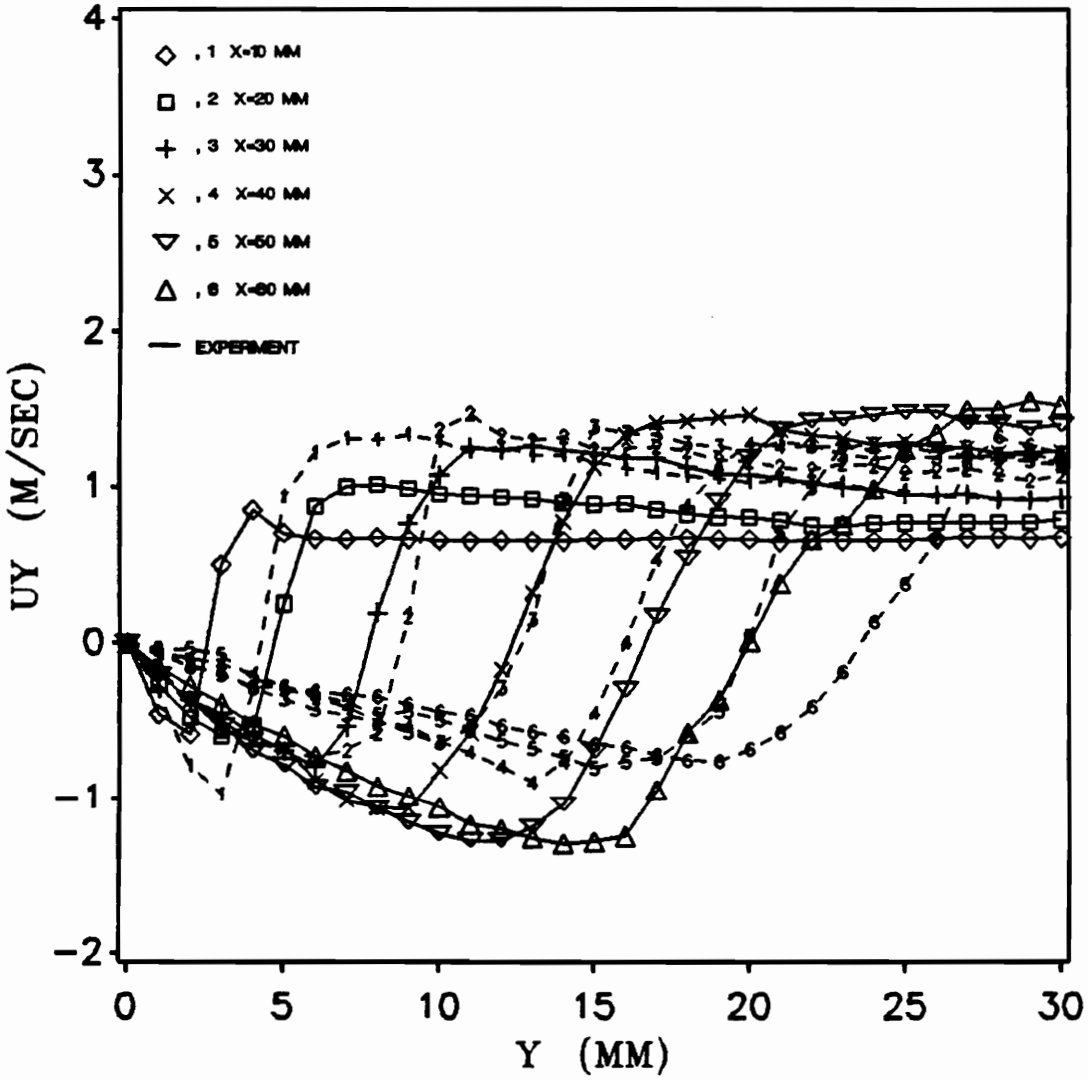

Figure 38. Computed turbulent Uy profiles: The existing source model with flame vorticity and turbulence.

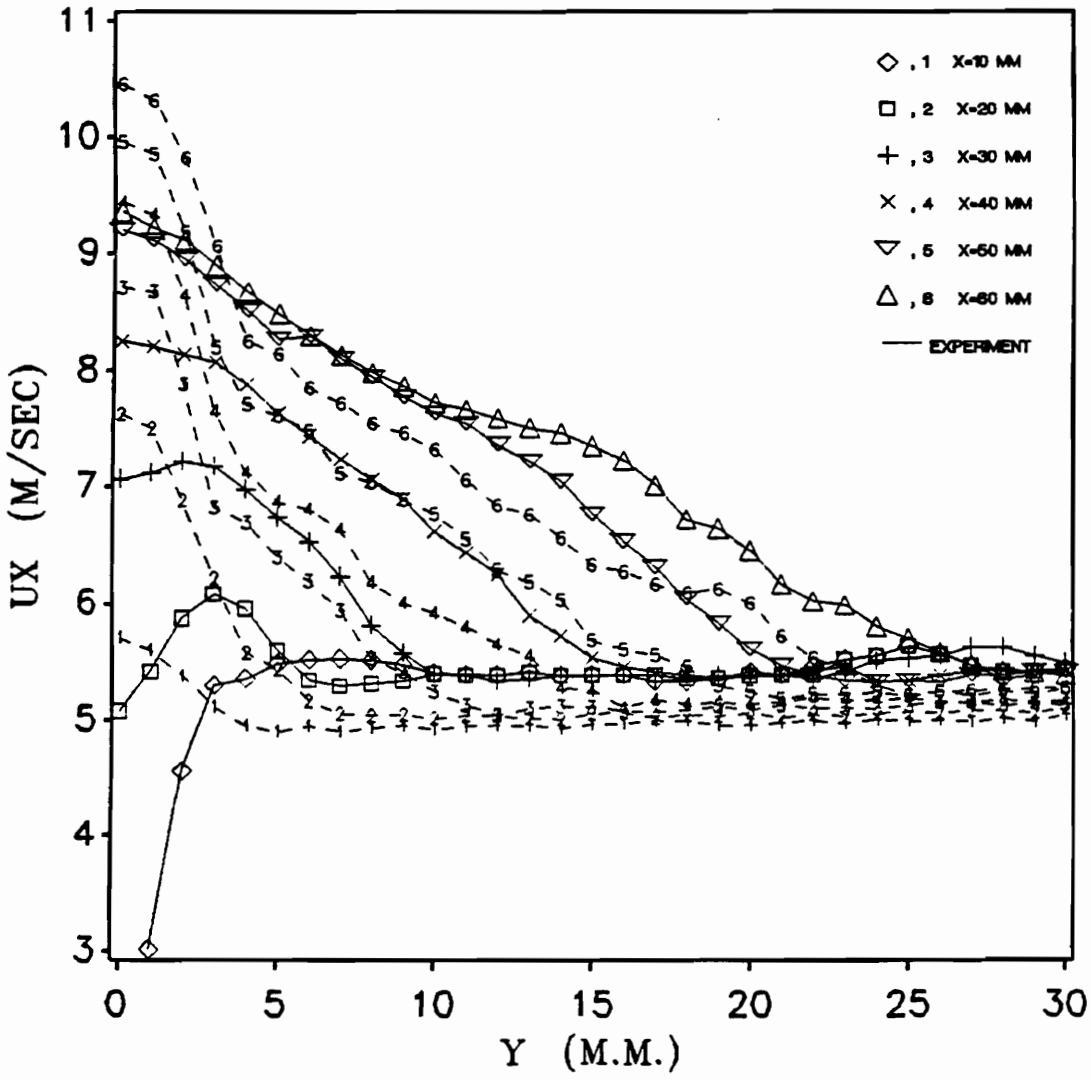

Figure 39. Computed turbulent Ux profiles: The modified source model with flame vorticity and turbulence.

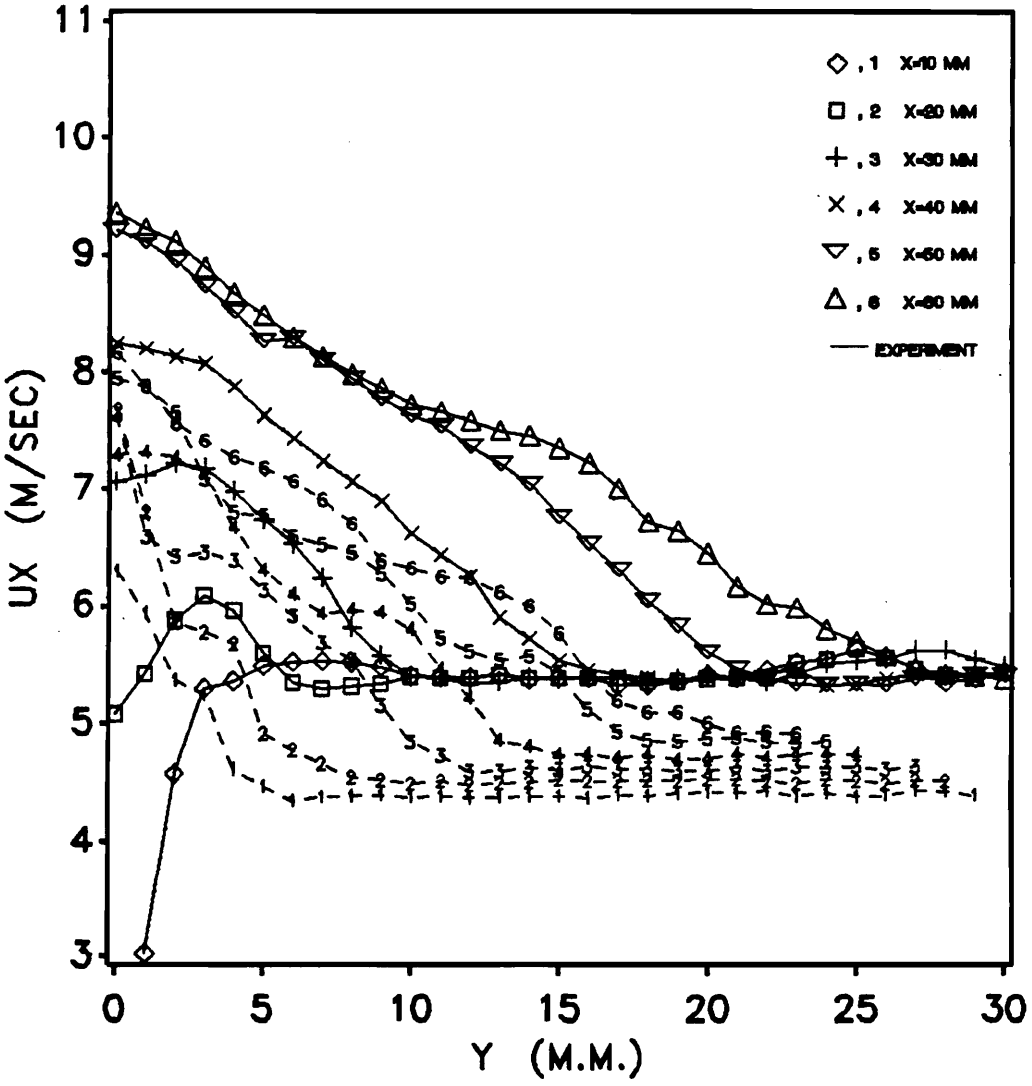

Figure 39a. Shifted turbulent Uy using the existing source model: Flame vorticity is included. The curves are shifted so that the computed flame angle matches the experiment. The superficial fitting to experiment is shown by discrepancy in this figure.

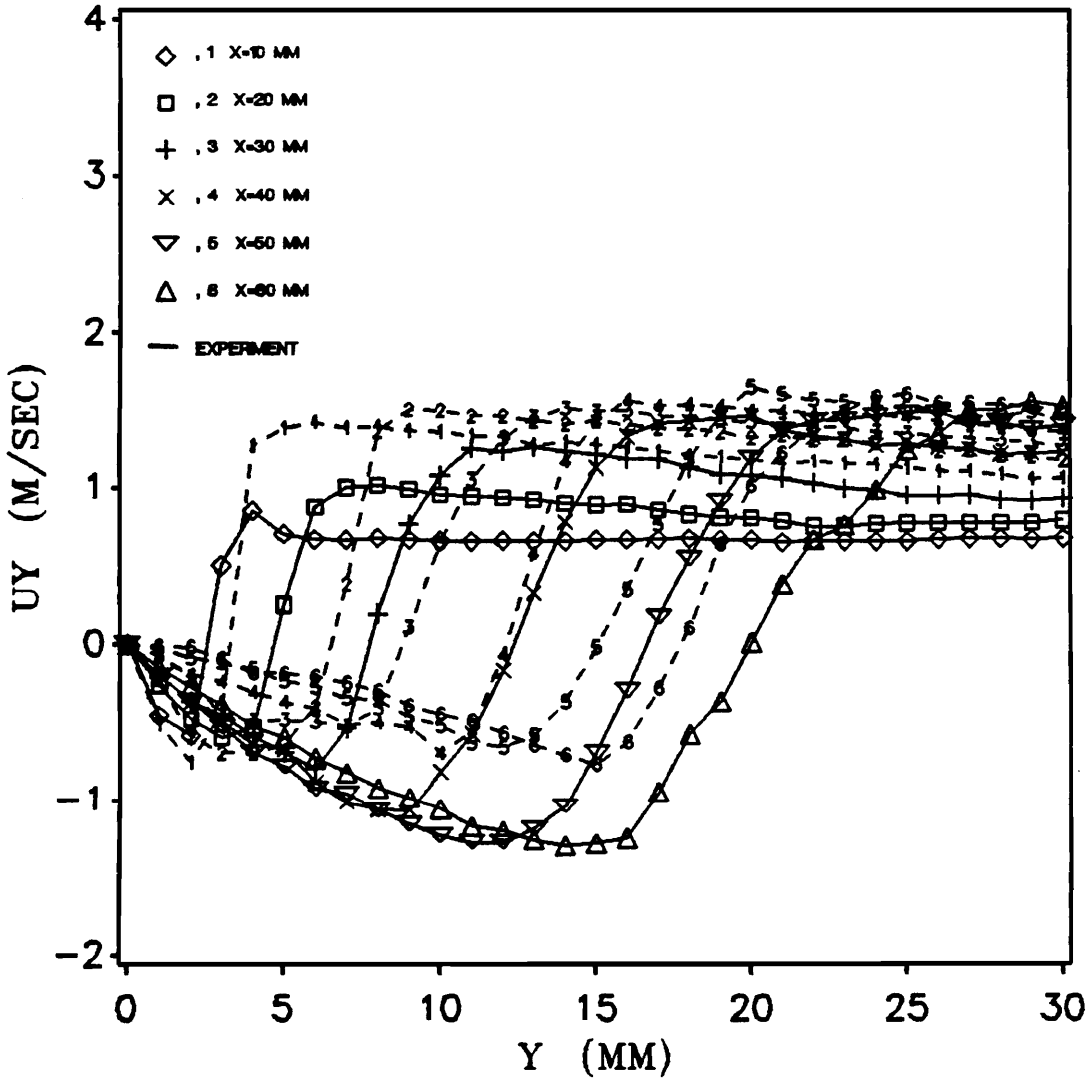

Figure 40. Computed turbulent Uy profiles: The modified source model with flame vorticity and turbulence.

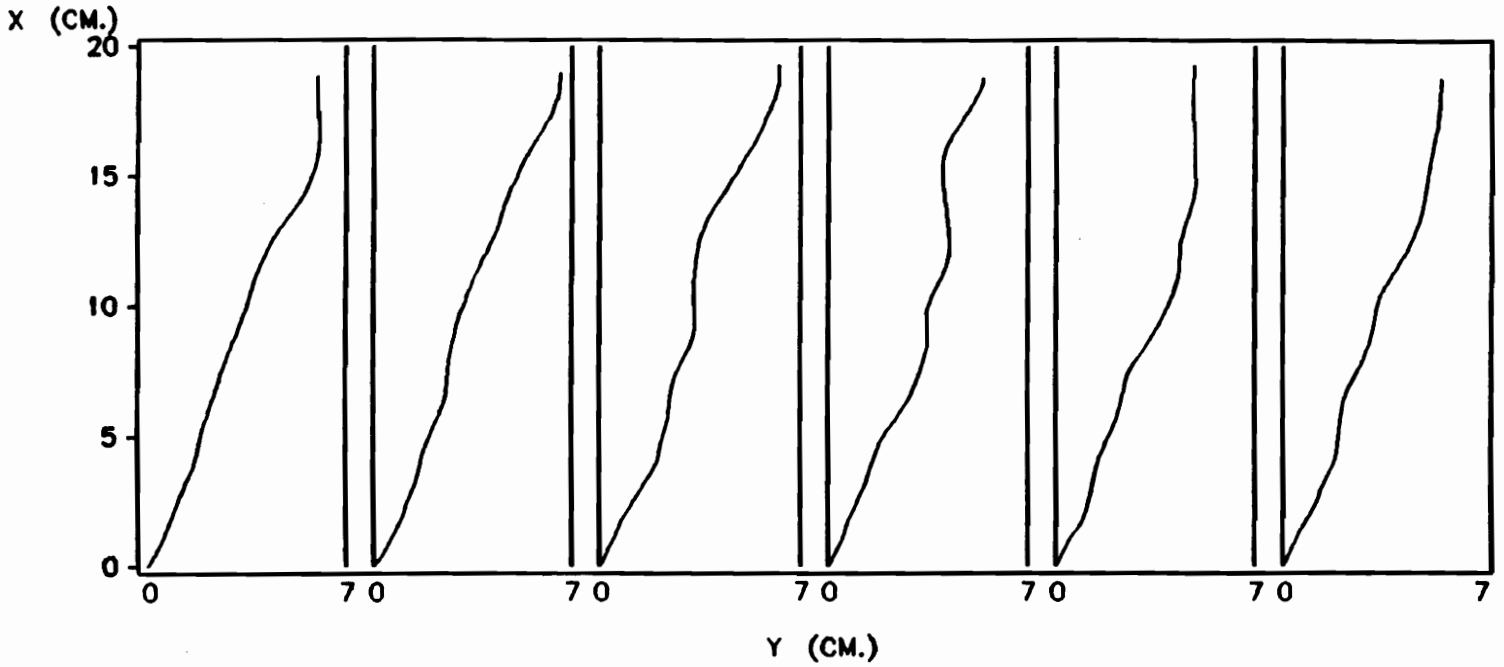

Figure 41. Instantaneous shape of a wrinkled flame sheet

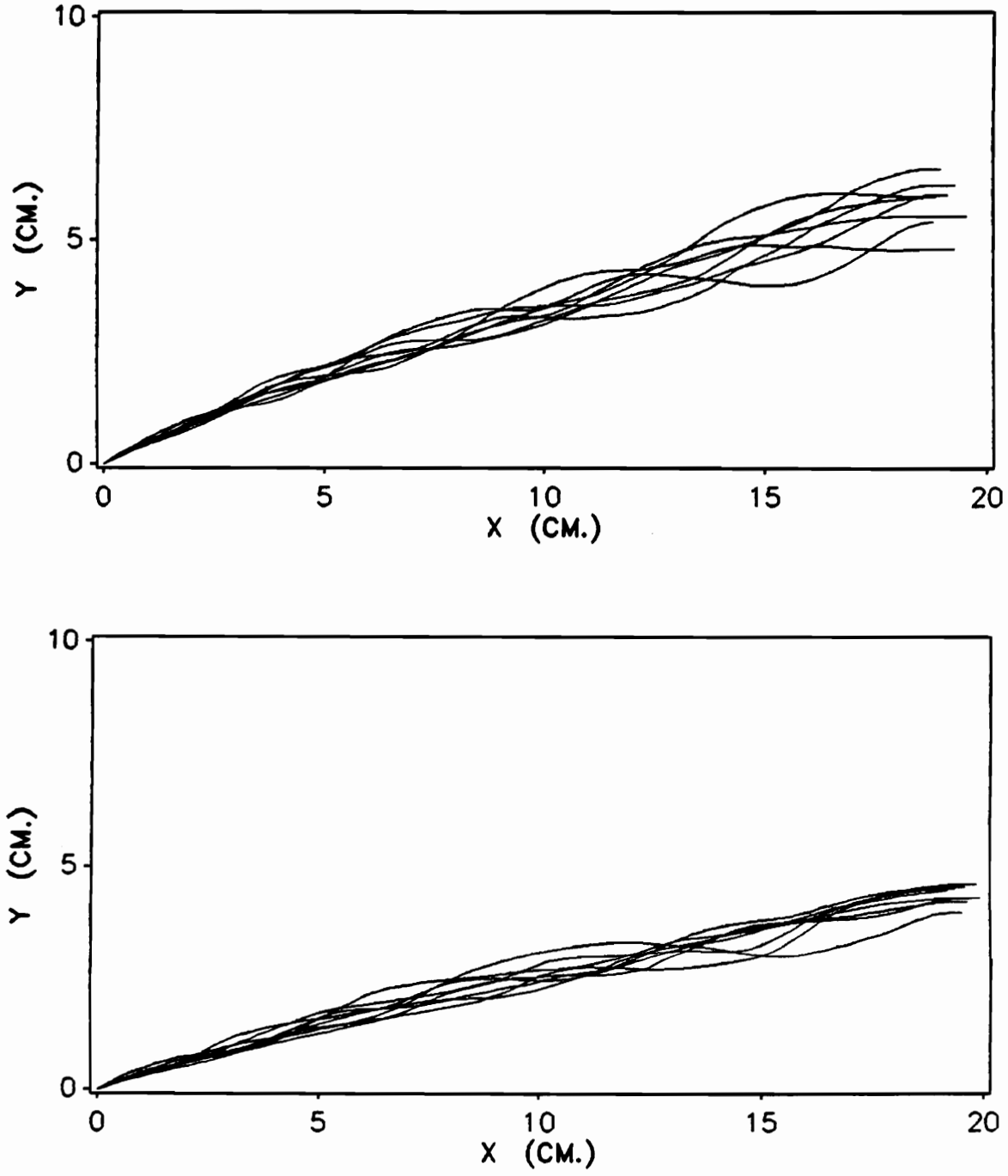

Figure 42. Computed turbulent flame brushes: Top figure is for the existing source model, bottom figure is for the modified source model.

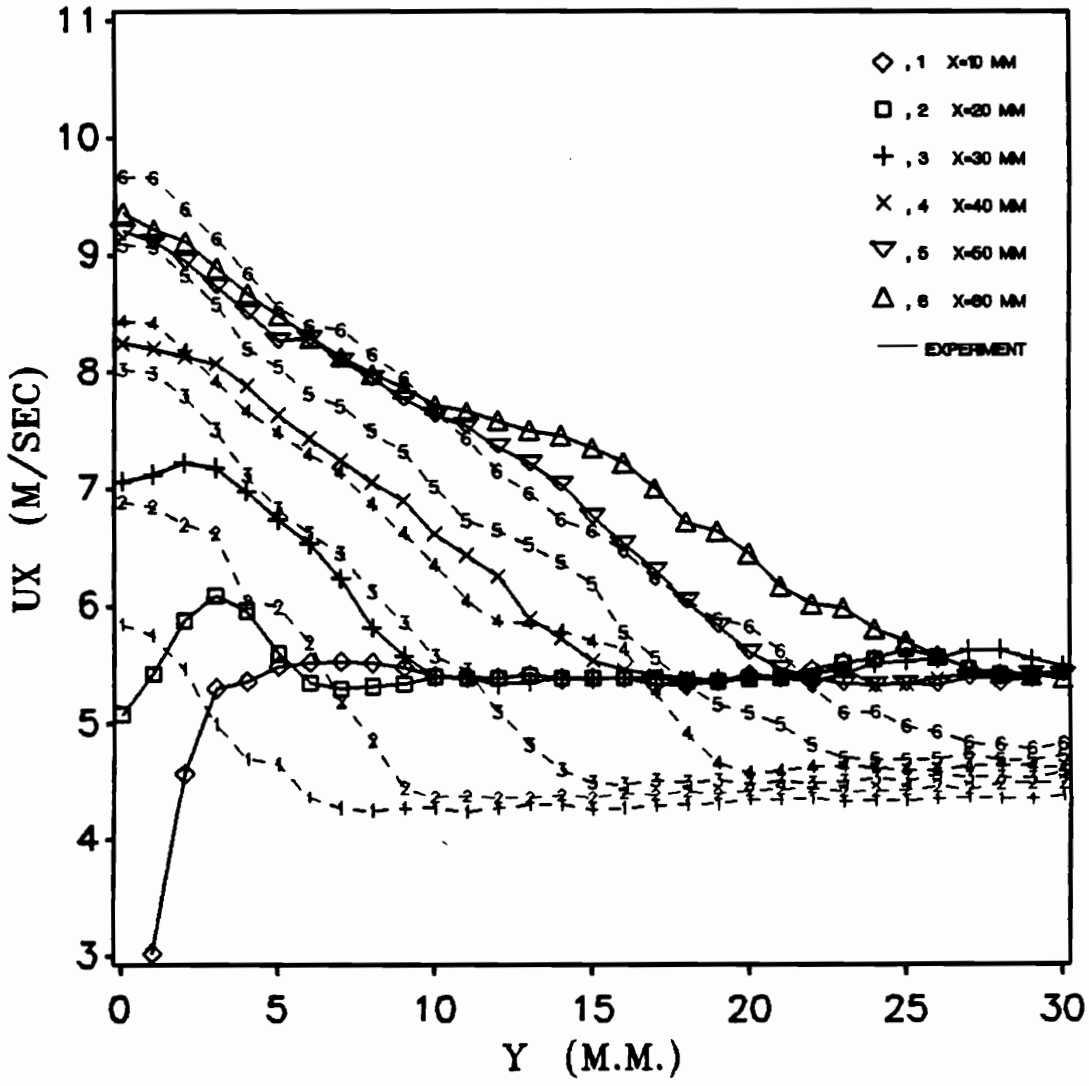

Figure 43. Turbulent Ux profiles computed without symmetry assumption: The existing source model with flame vorticity and turbulence.

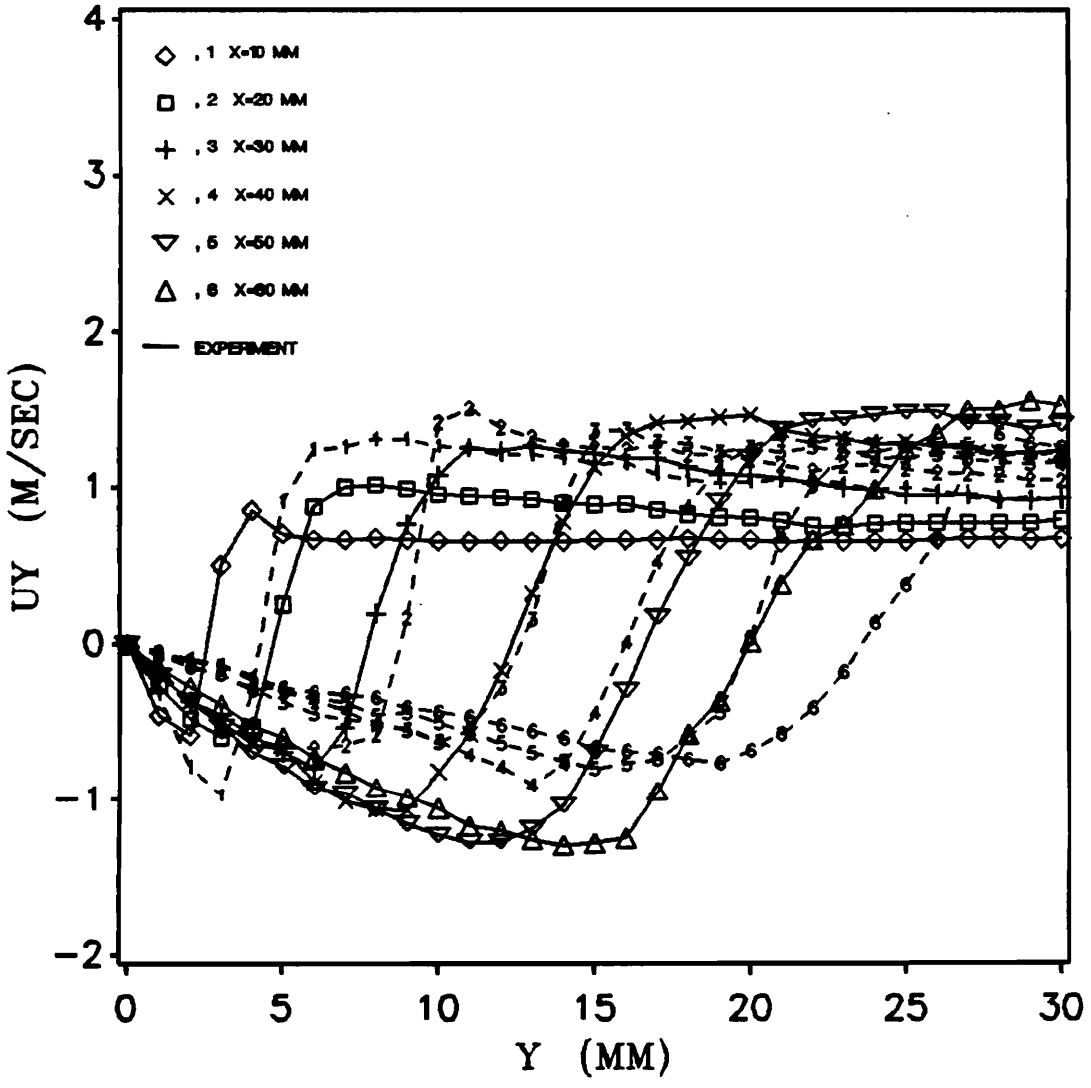

Figure 44. Turbulent Uy profiles computed without symmetry assumption: The existing source model with flame vorticity and turbulence.

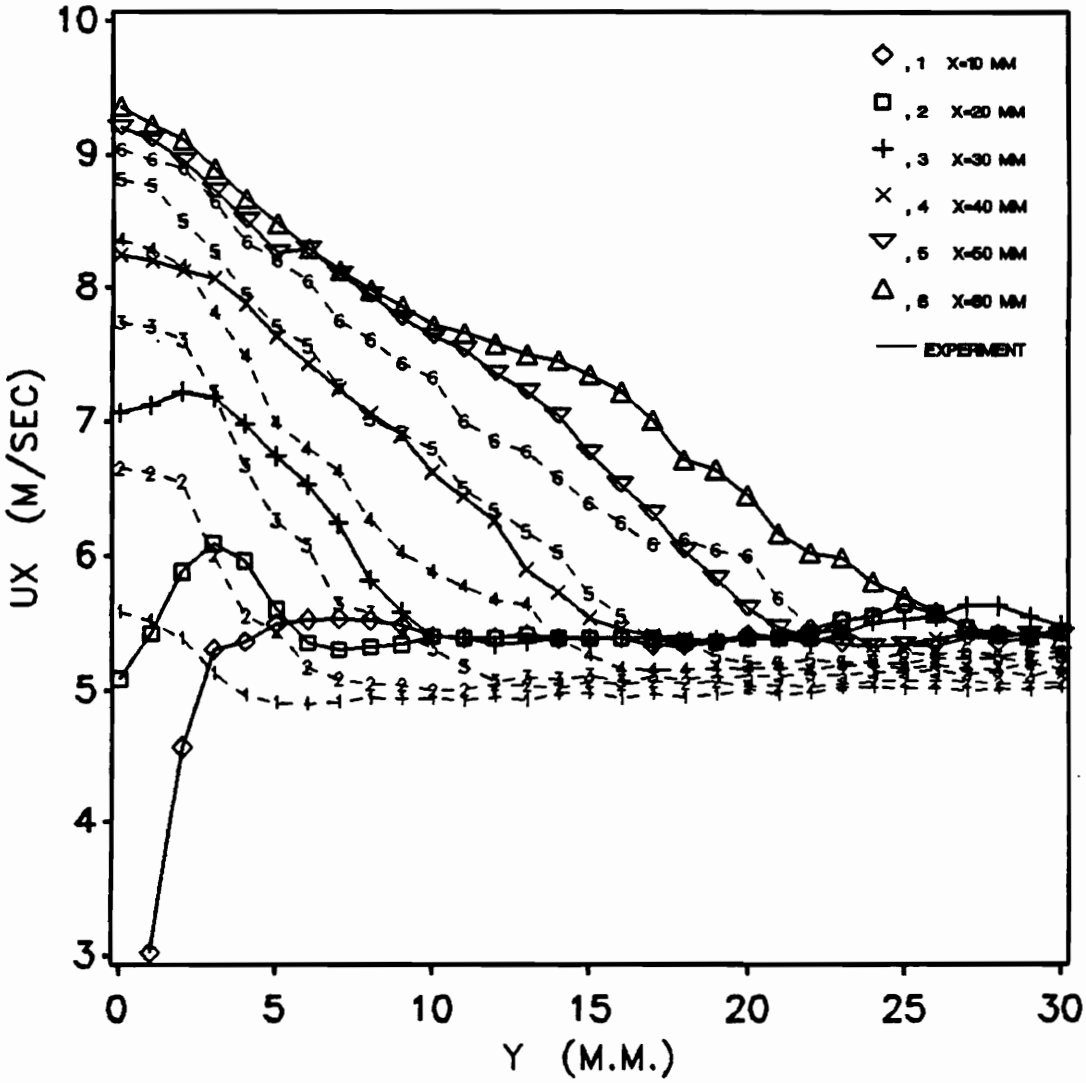

Figure 45. Turbulent Ux profiles computed without symmetry assumption: The modified source model with flame vorticity and turbulence

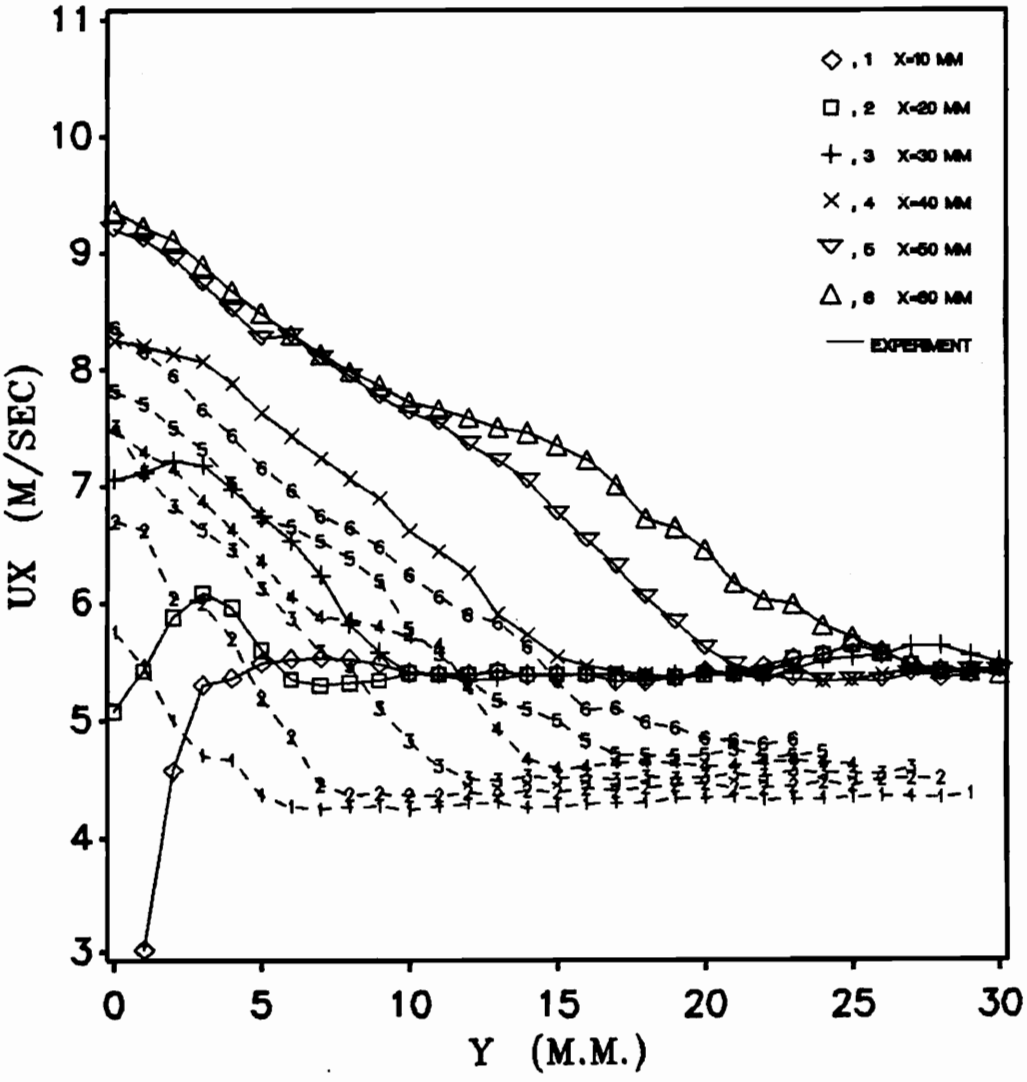

Figure 45a. Shifted turbulent Ux profiles using the existing source model: Flame vorticity is included, symmetry assumption is relaxed. The curves are shifted to match the measured flame angle.

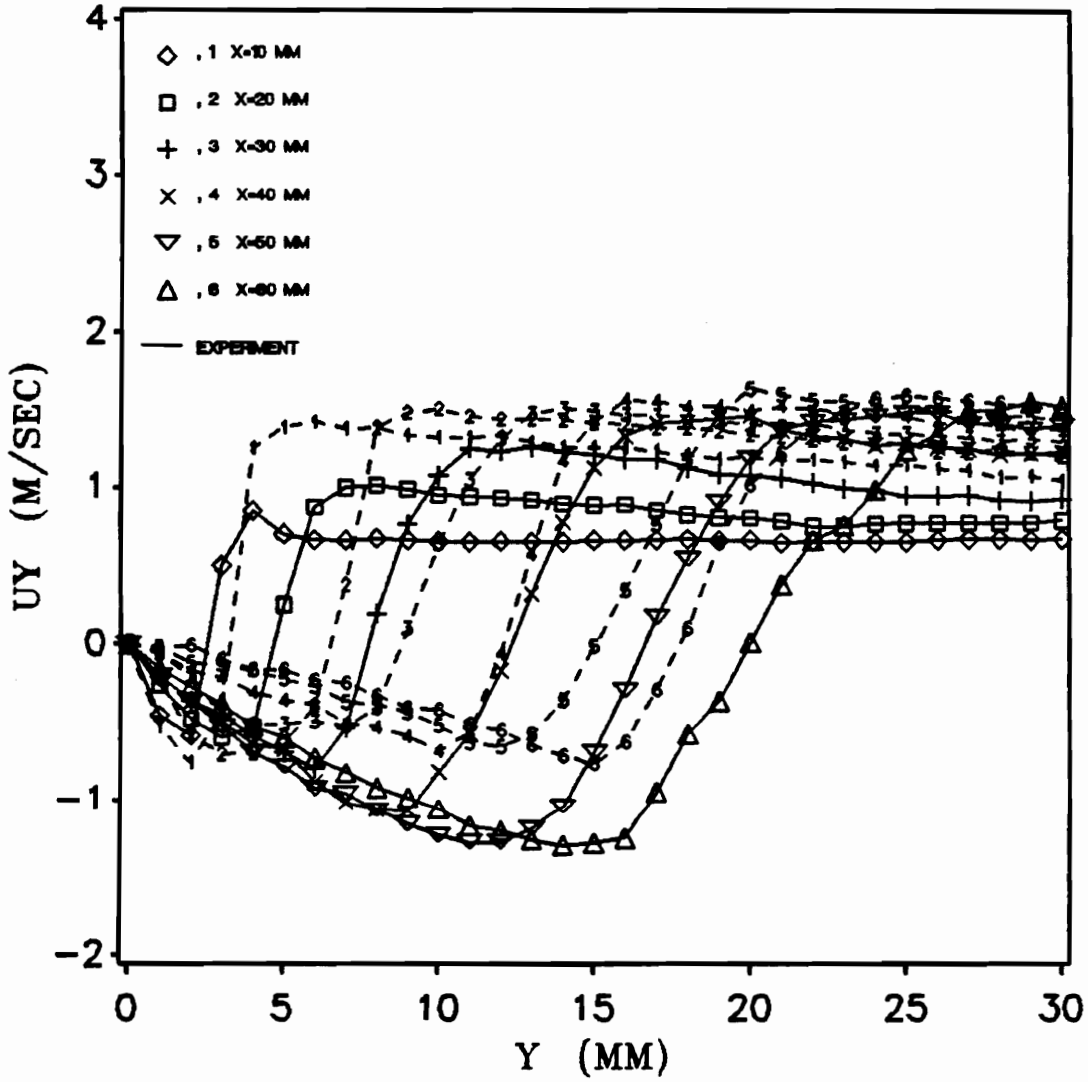

Figure 46. Turbulent Uy profiles computed without symmetry assumption: The modified source model with flame vorticity and turbulence

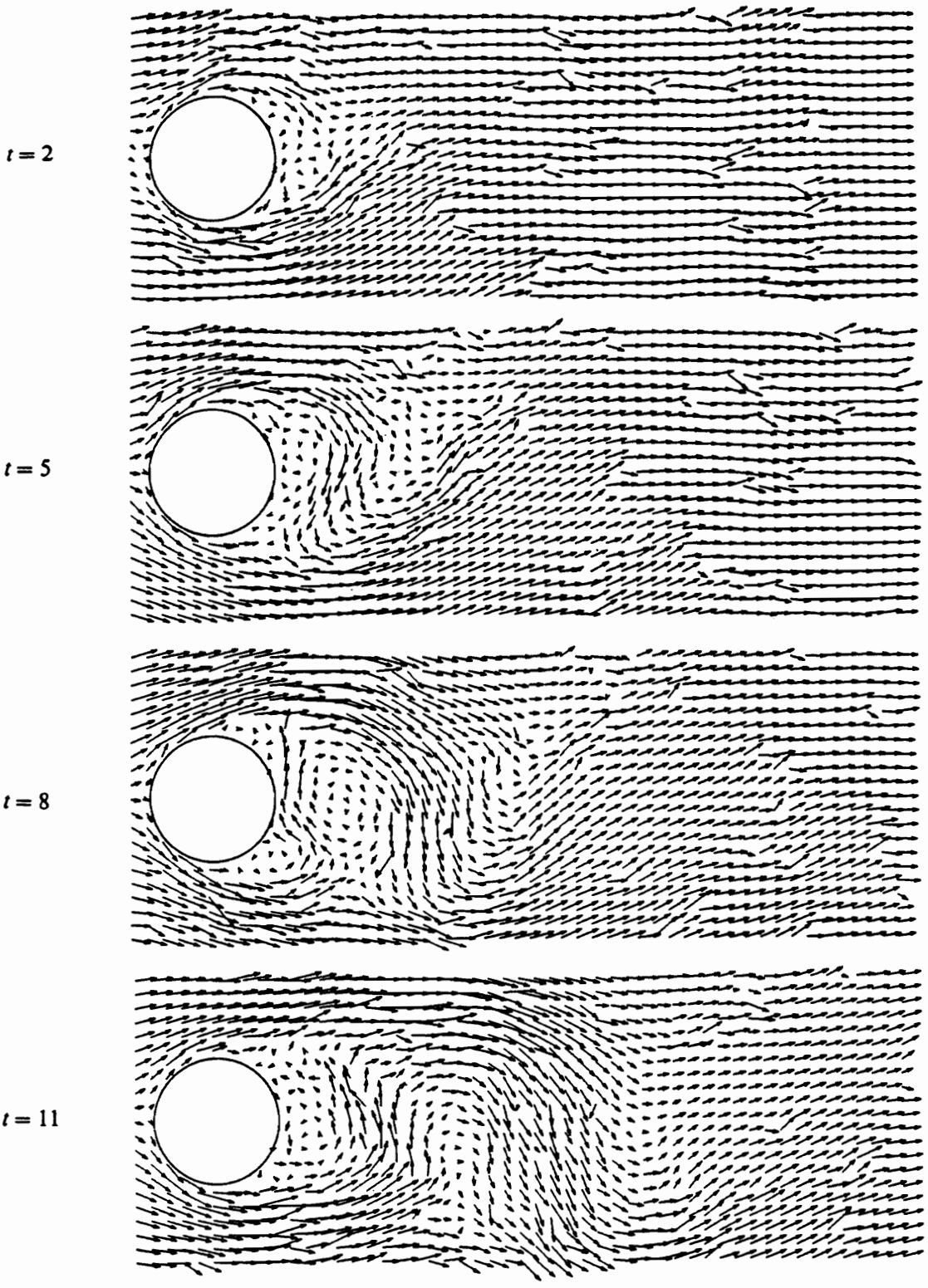

Figure 47. Computed turbulent flow past a circular cylinder, Re = 12000

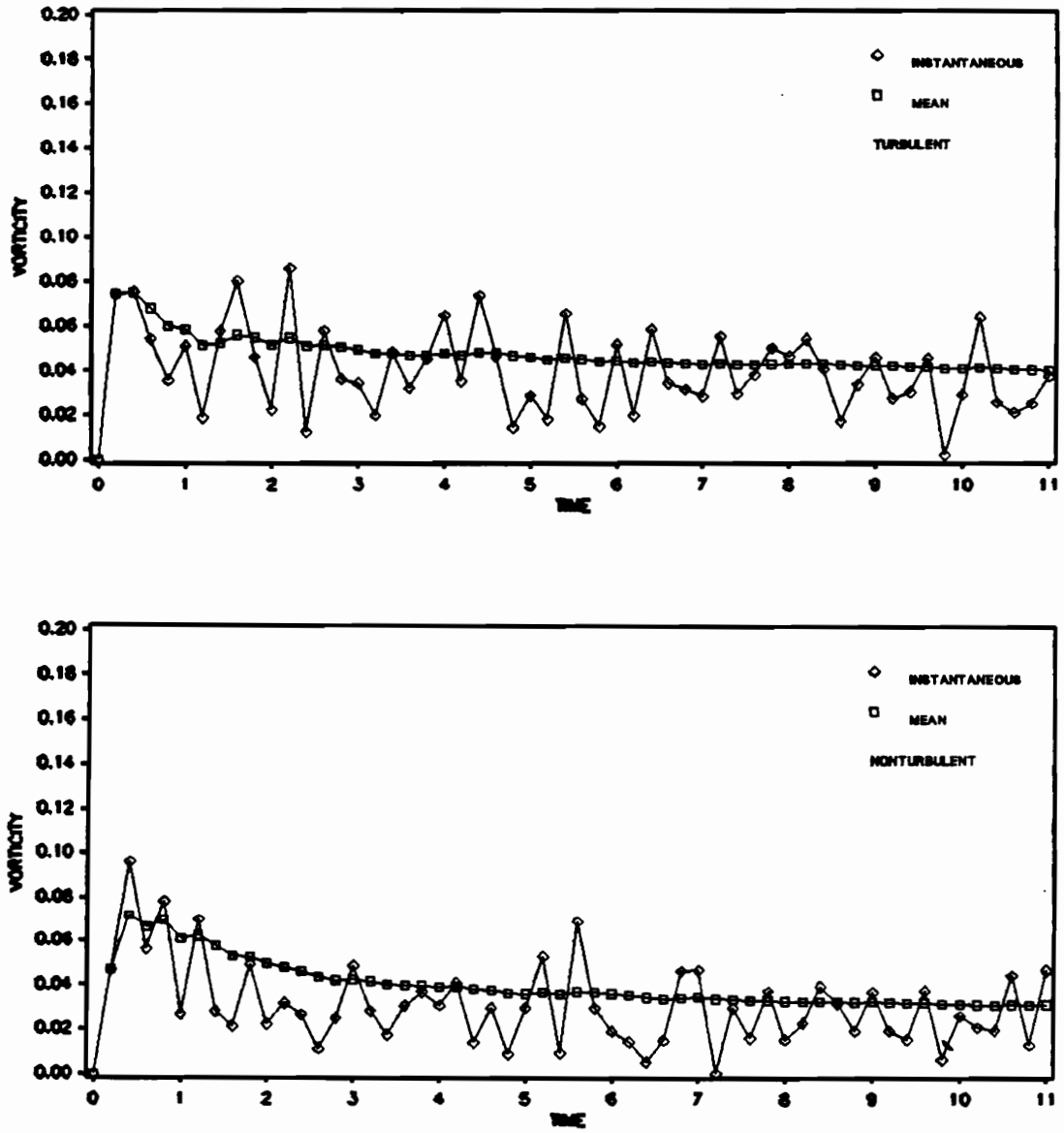

Figure 48. Clockwise vorticity shed by a circular cylinder: Top figure is obtained with turbulence in the approach flow, bottom figure is without turbulence.

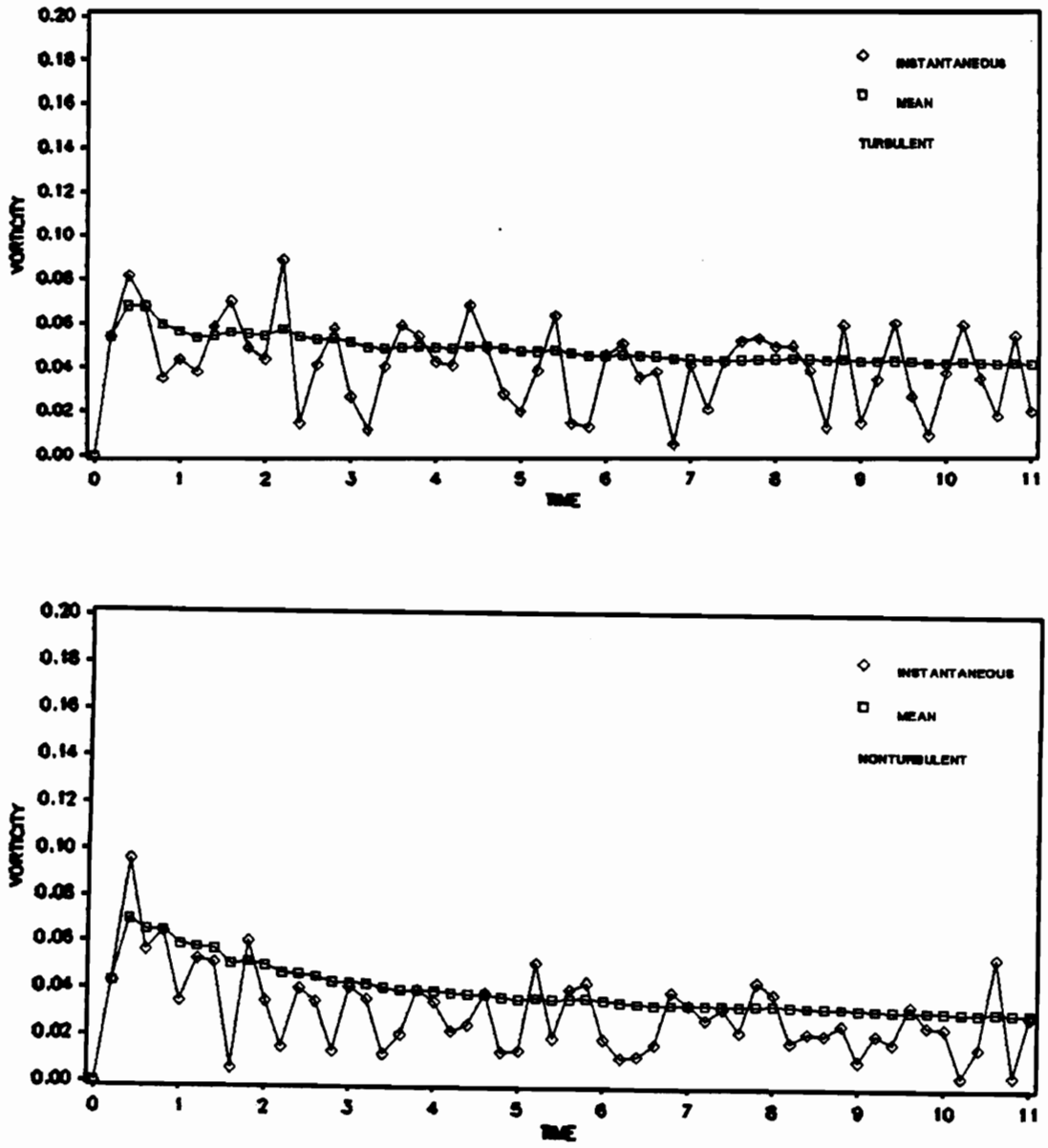

Figure 49. Counterclockwise vorticity shed by a circular cylinder: Top figure is obtained with turbulence in the approach flow, bottom figure is without turbulence.

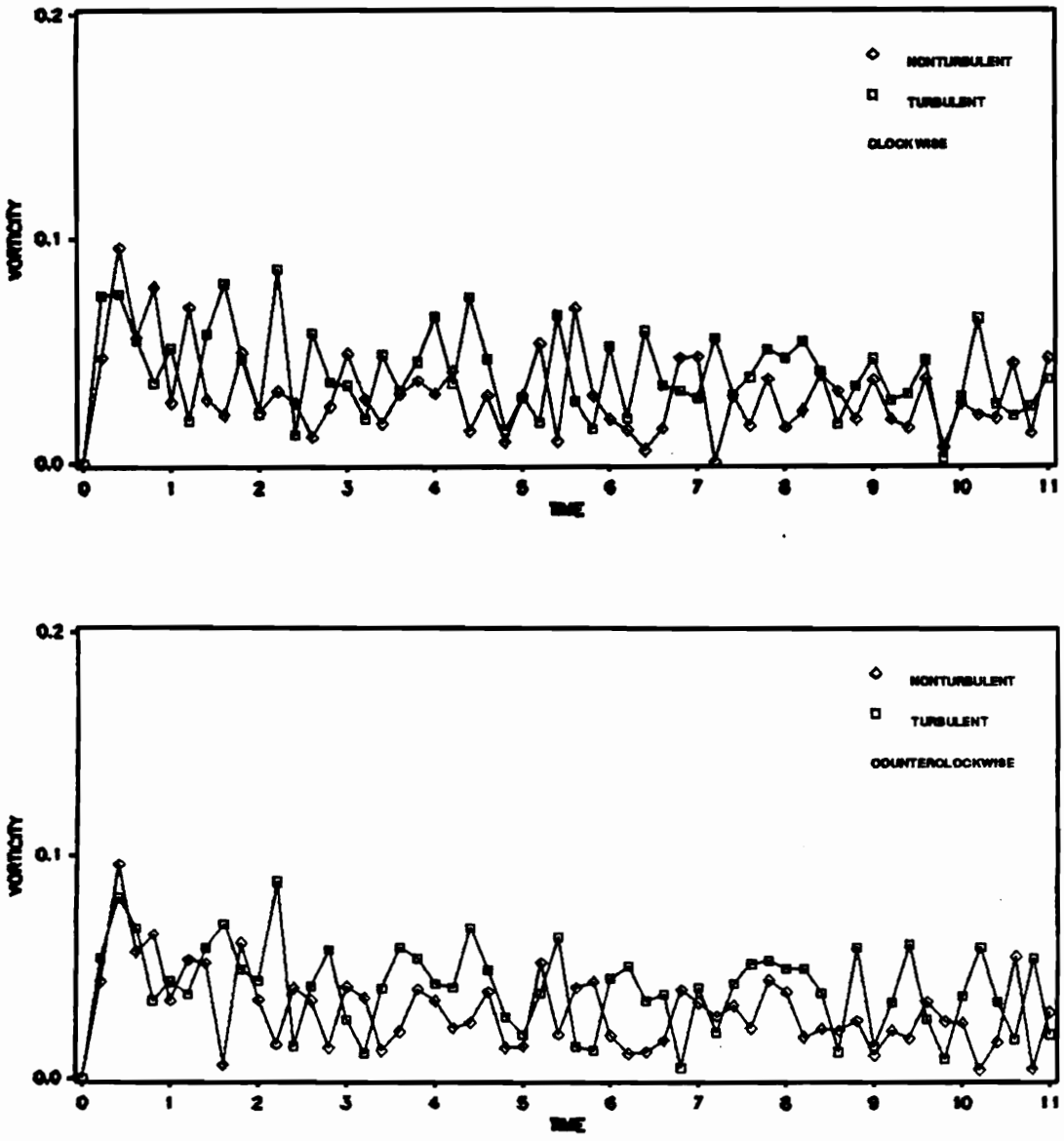

Figure 50. Vorticity shed by a circular cylinder in turbulent and nonturbulent flows: Top figure is for clockwise vorticity, bottom figure is for counterclockwise vorticity. General behaviors of turbulent and nonturbulent production are similar.

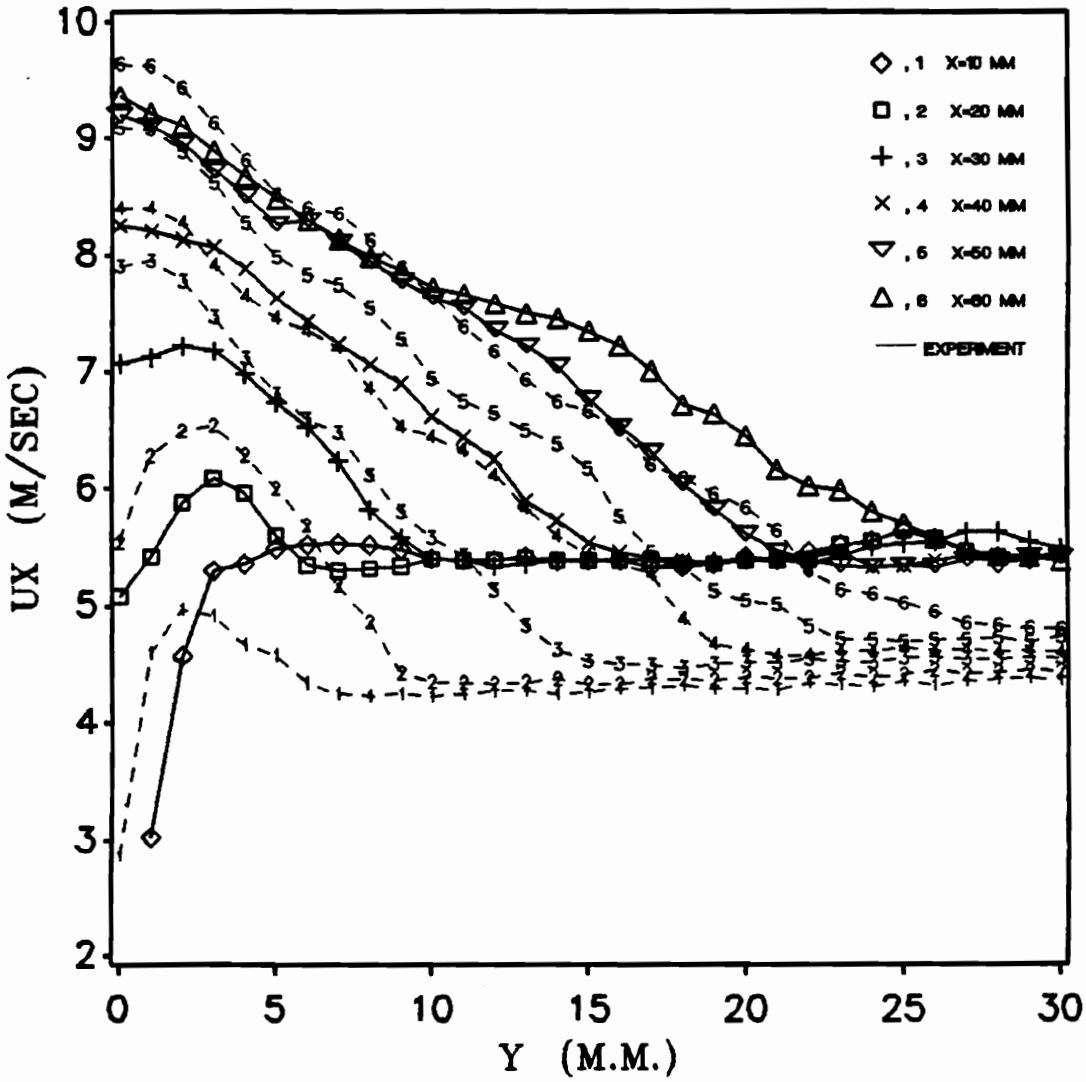

Figure 51. Computed Ux profiles with flameholder effects included: Existing source model with flame vorticity and turbulence. Symmetry assumption is relaxed.

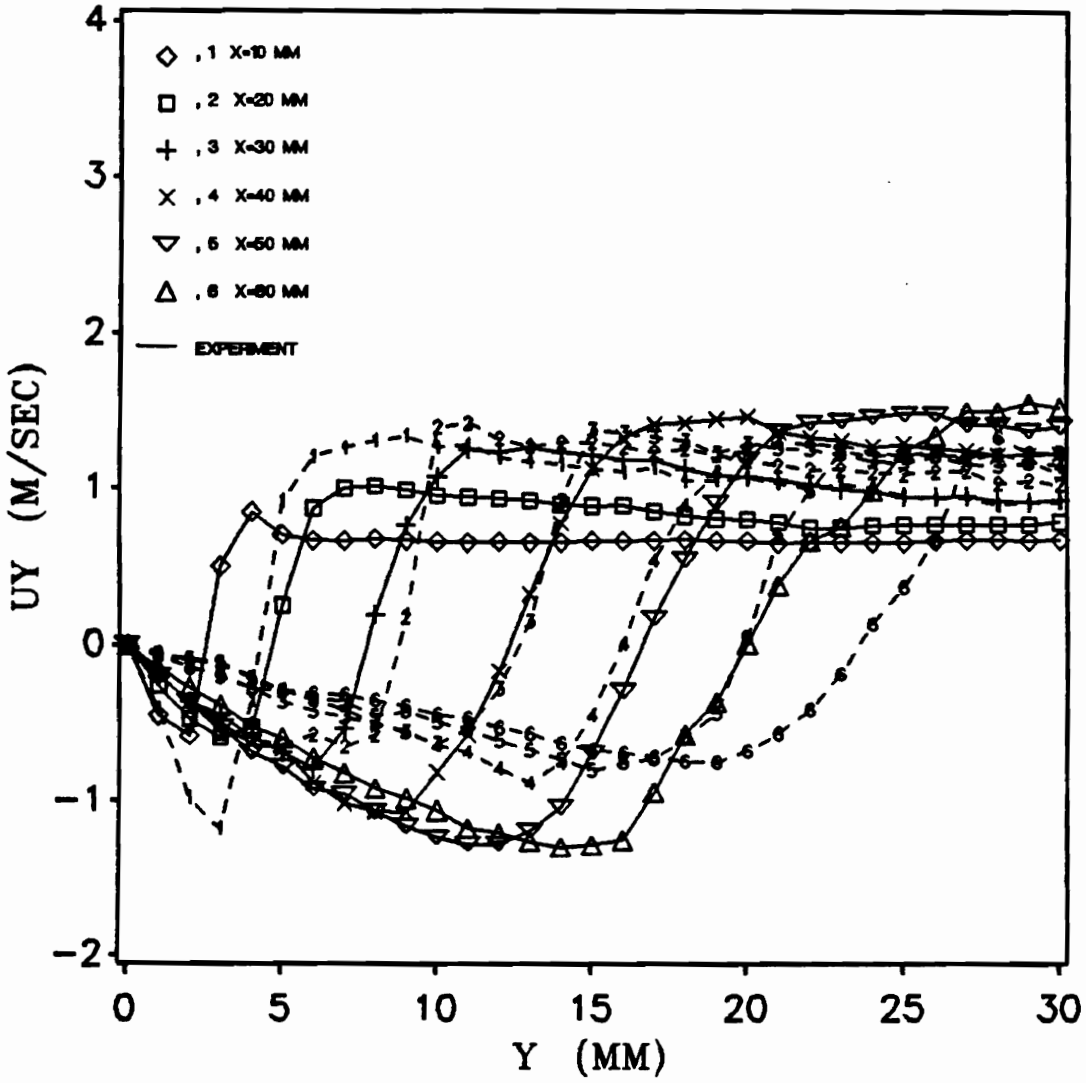

Figure 52. Computed Uy profiles with flameholder effects included: Existing source model with flame vorticity and turbulence. Symmetry assumption is relaxed.

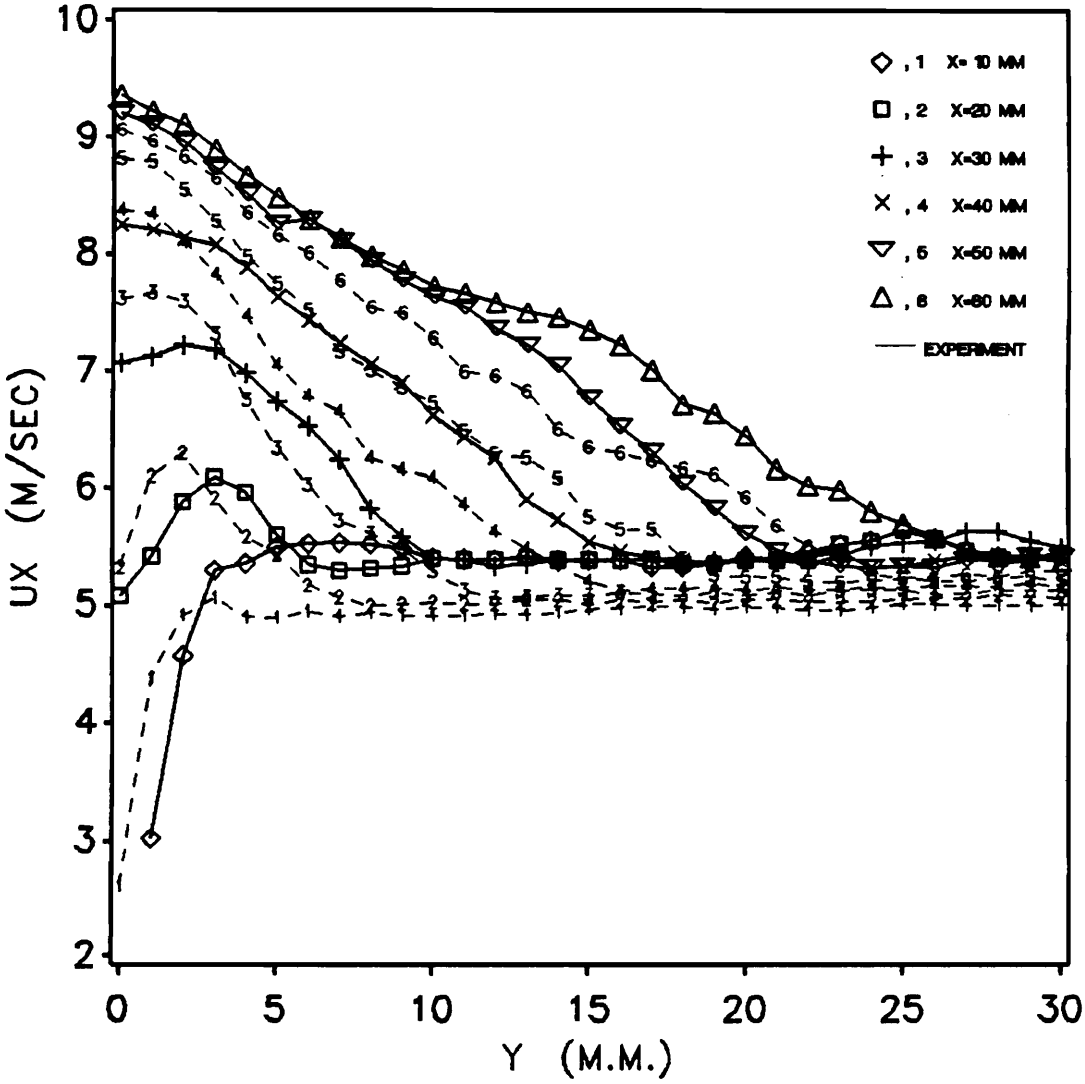

Figure 53. Computed Ux profiles with flameholder effects included: Modified source model with flame vorticity and turbulence. Symmetry assumption is relaxed.

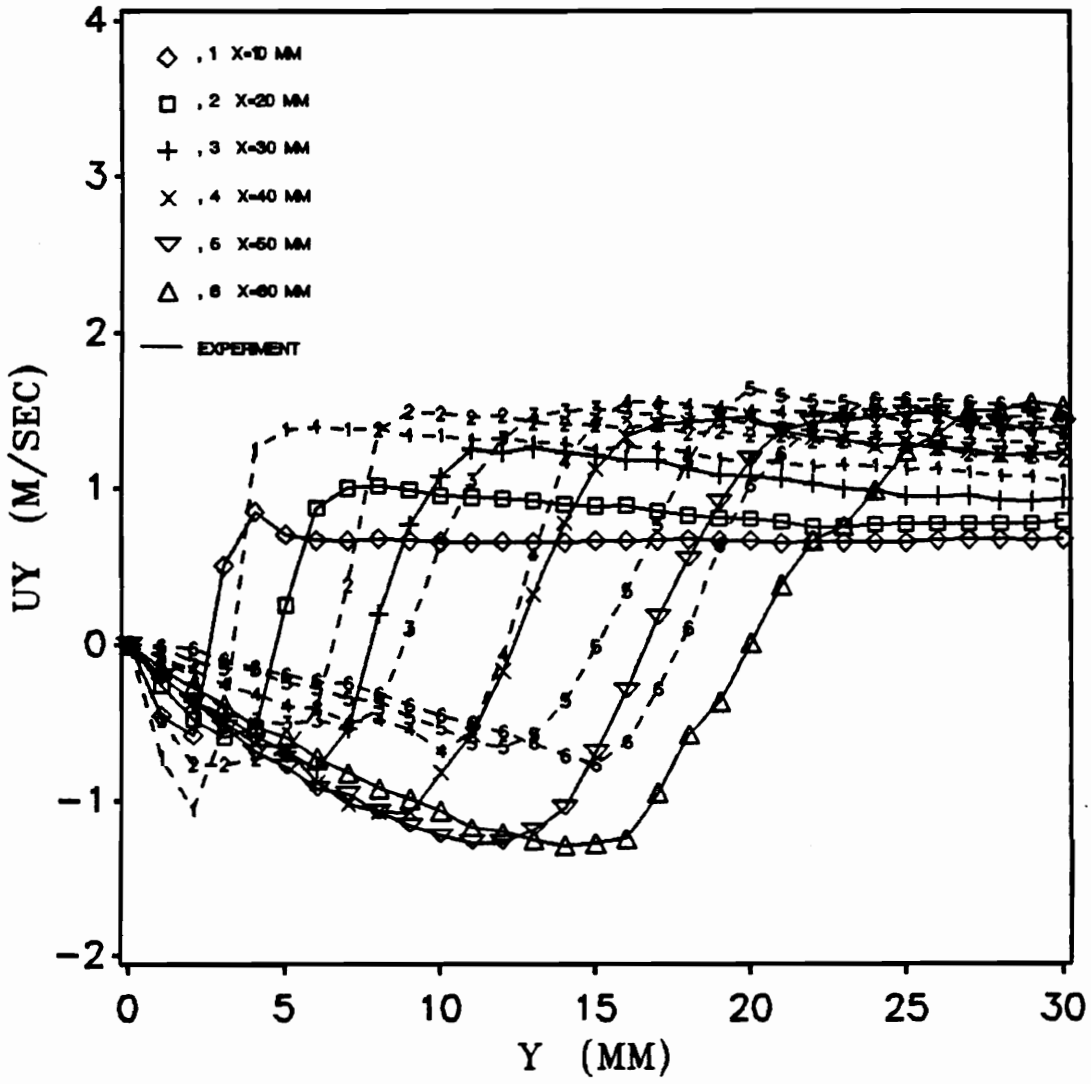

Figure 54. Computed Uy profiles with flameholder effects included: Modified source model with flame vorticity and turbulence. Symmetry assumption is relaxed.

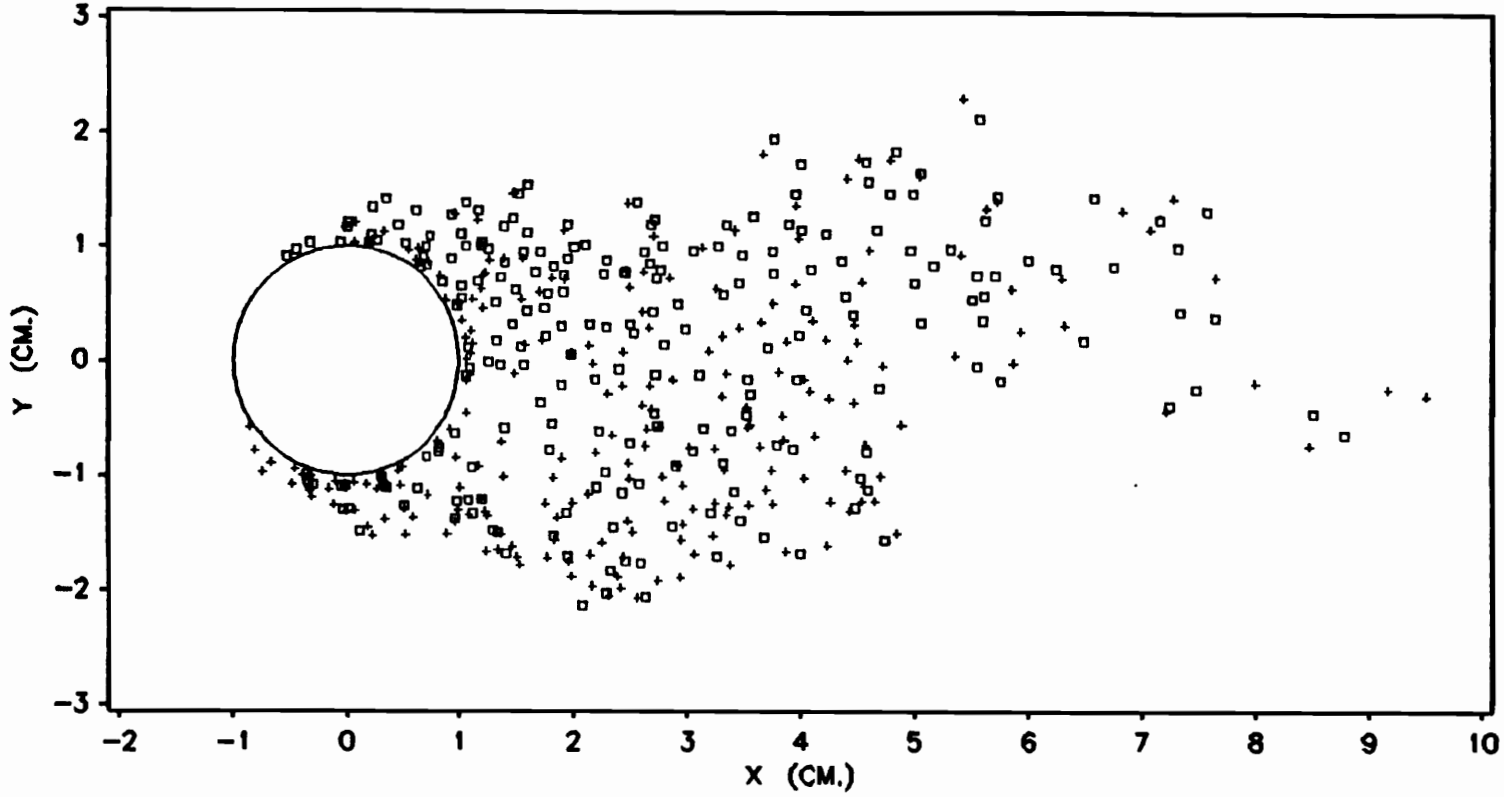

Figure 55. Distribution of vortices with opposite senses of rotation

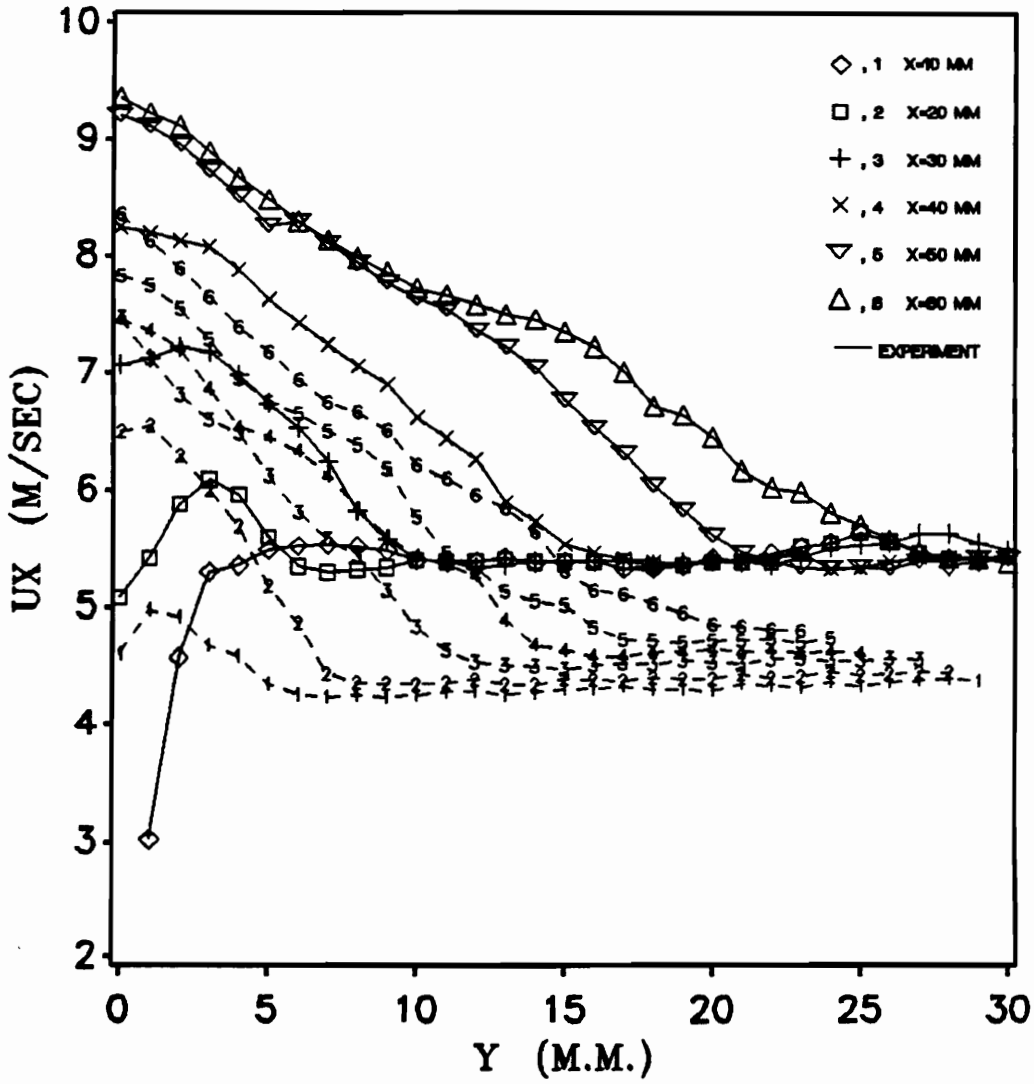

Figure 55a. Shifted turbulent Ux profiles using the existing source model: Flame vorticity is included, symmetry assumption is relaxed, flame stabilizer effect is included. The curves are shifted to match the measured flame angle.

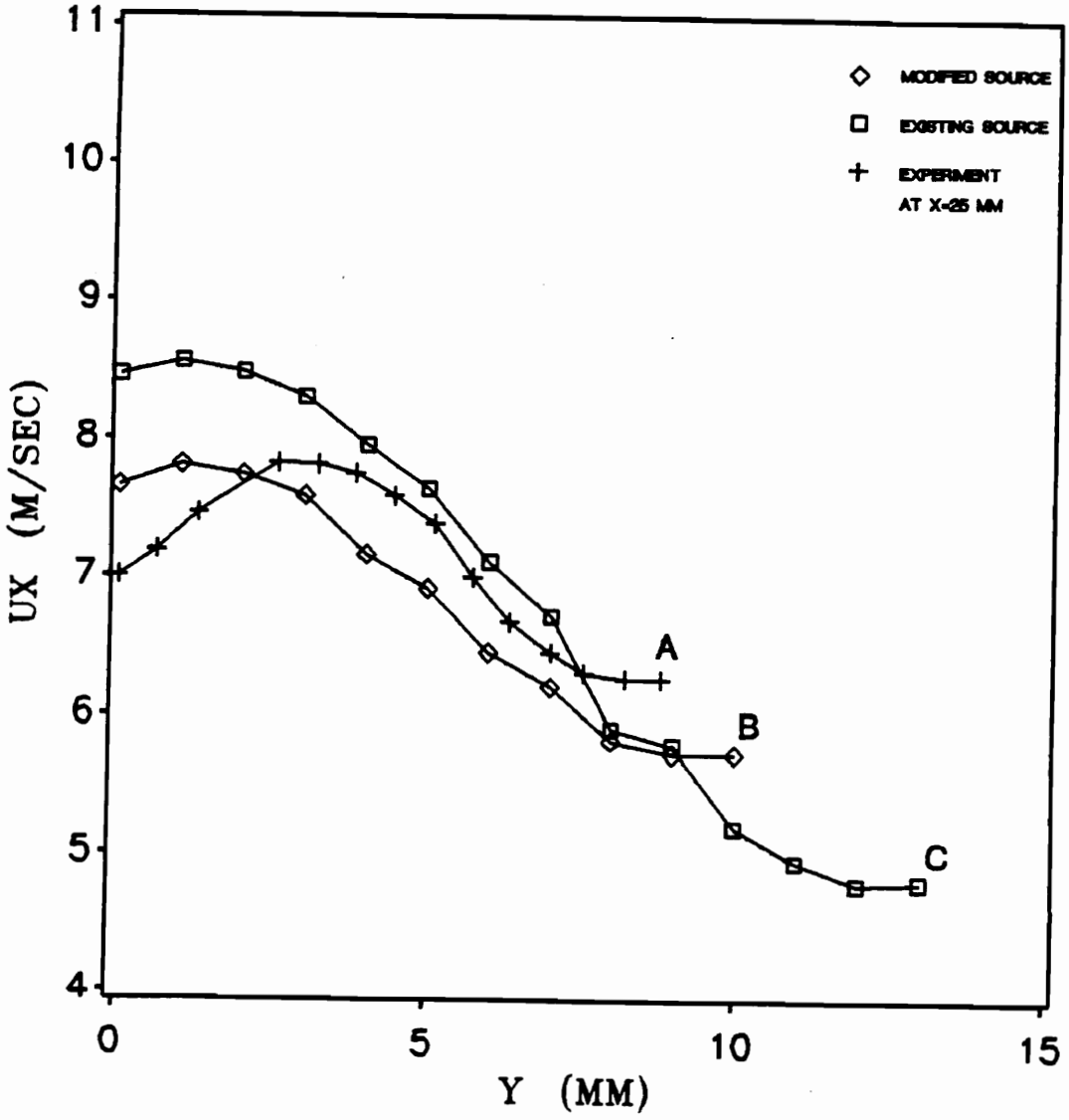

Figure 56. Computed Ux profiles for Dandekar and Gouldin's experiment: Flame 3 in Table 1. Flameholder effects, flame vorticity and turbulence are included. Symmetry assumption is relaxed.

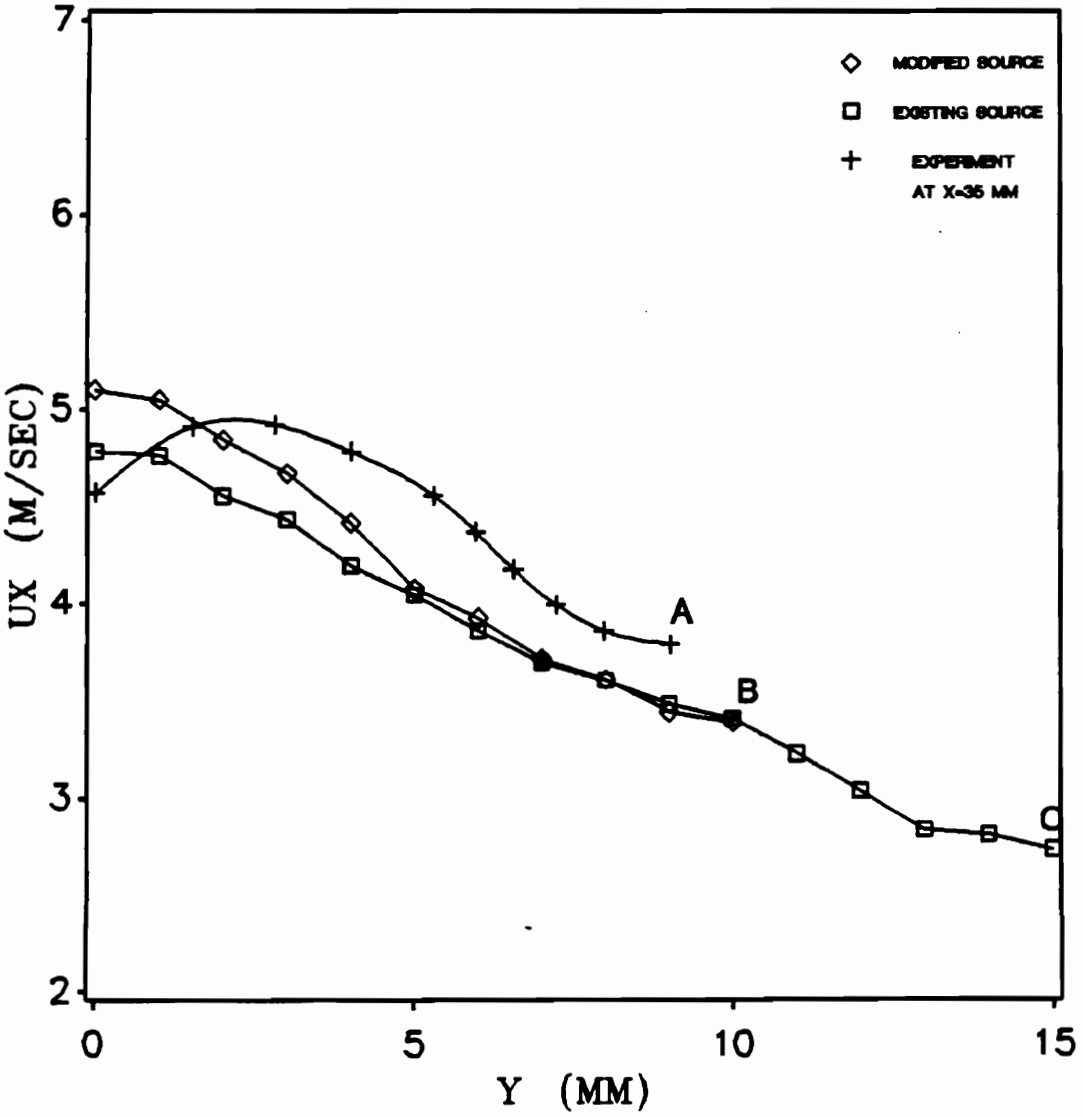

Figure 57. Computed Ux profiles for Dandekar and Gouldin's experiment: Flame 6 in Table 1. Flameholder effects, flame vorticity and turbulence are included. Symmetry assumption is relaxed.

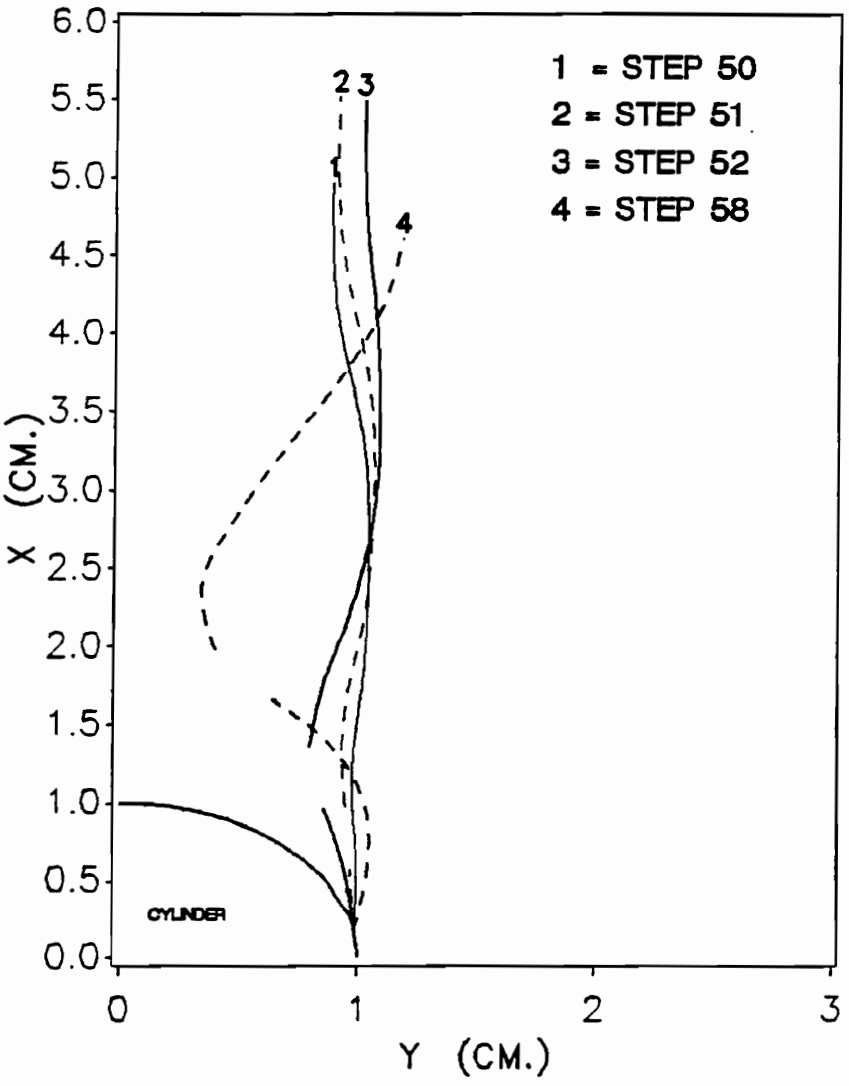

Figure 58. Broken flame sheets near a large circular cylinder: Flame extinction and fragmentation due to high rate of flame stretch near a large circular cylinder.

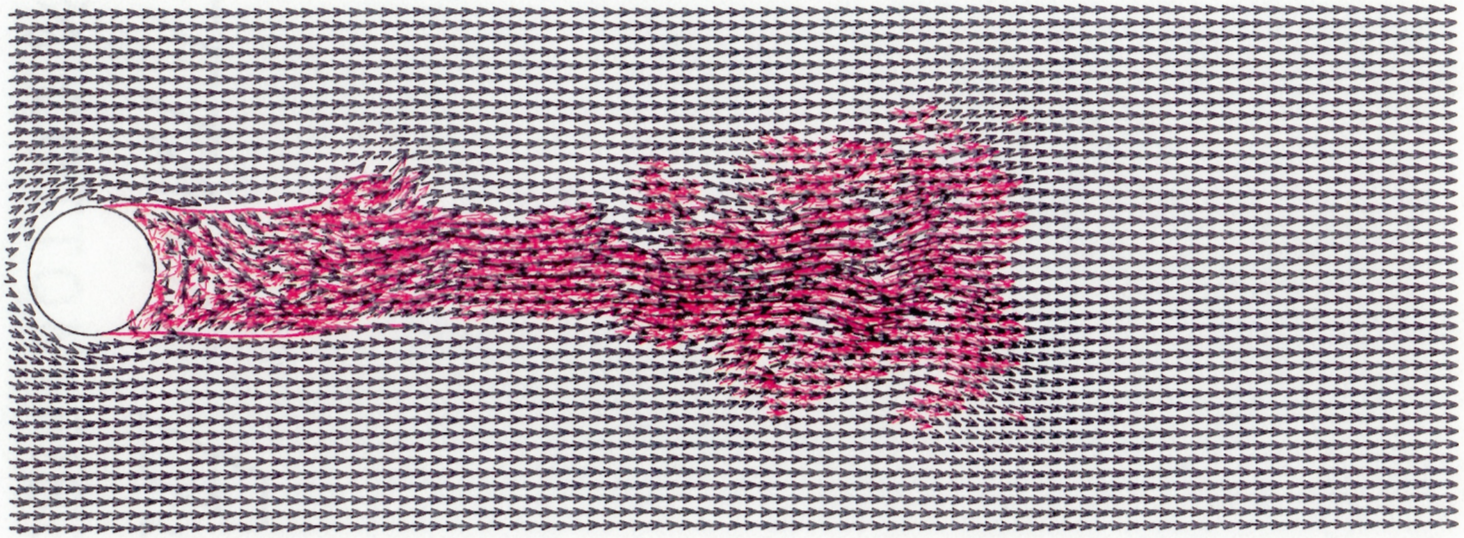

Figure 59. Turbulent reacting flow near a large cylinder, time step = 50: Modofied source model. Thick arrows are velocity vectors at fixed sampling points and thin arrows are velocity of individual vortices.

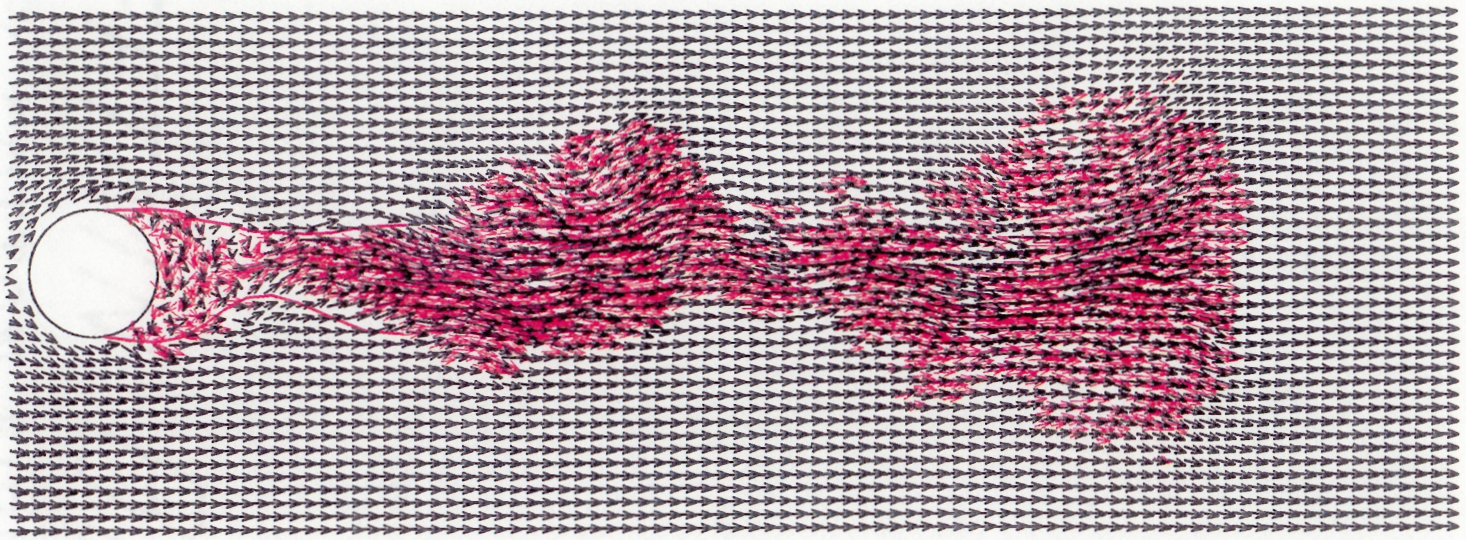

Figure 60. Turbulent reacting flow near a large cylinder, time step = 60: Modofied source model. Thick arrows are velocity vectors at fixed sampling points and thin arrows are velocity of individual vortices.

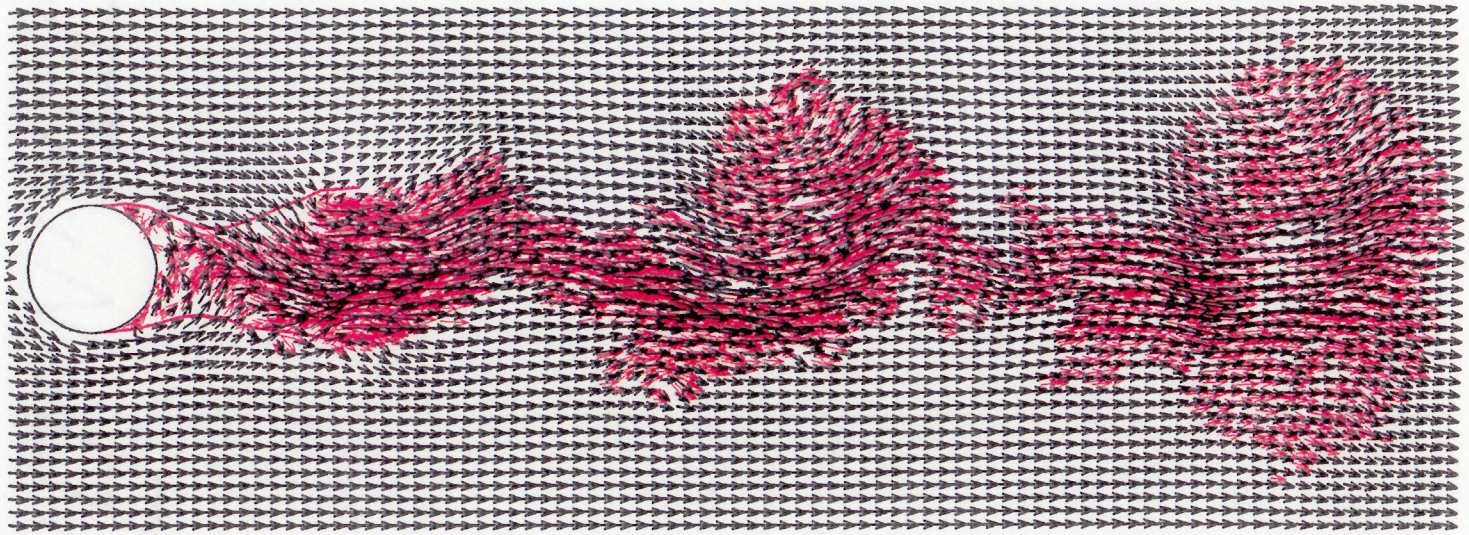

Figure 61. Turbulent reacting flow near a large cylinder, time step = 70: Modofied source model. Thick arrows are velocity vectors at fixed sampling points and thin arrows are velocity of individual vortices.

Figure 62. Contraction of reacting flow near a bluff-body flame holder: Taken from Fig. 24 (top) and Fig. 25 in 'Some experimental techniques for the investigation of the mechanism of flame stabilization in the wakes of bluff bodies'; Nicholson, H. M. and Field, J. P.; 3rd Symp. on Comust., Flame, and Explosion; 1949; pp. 44-68.

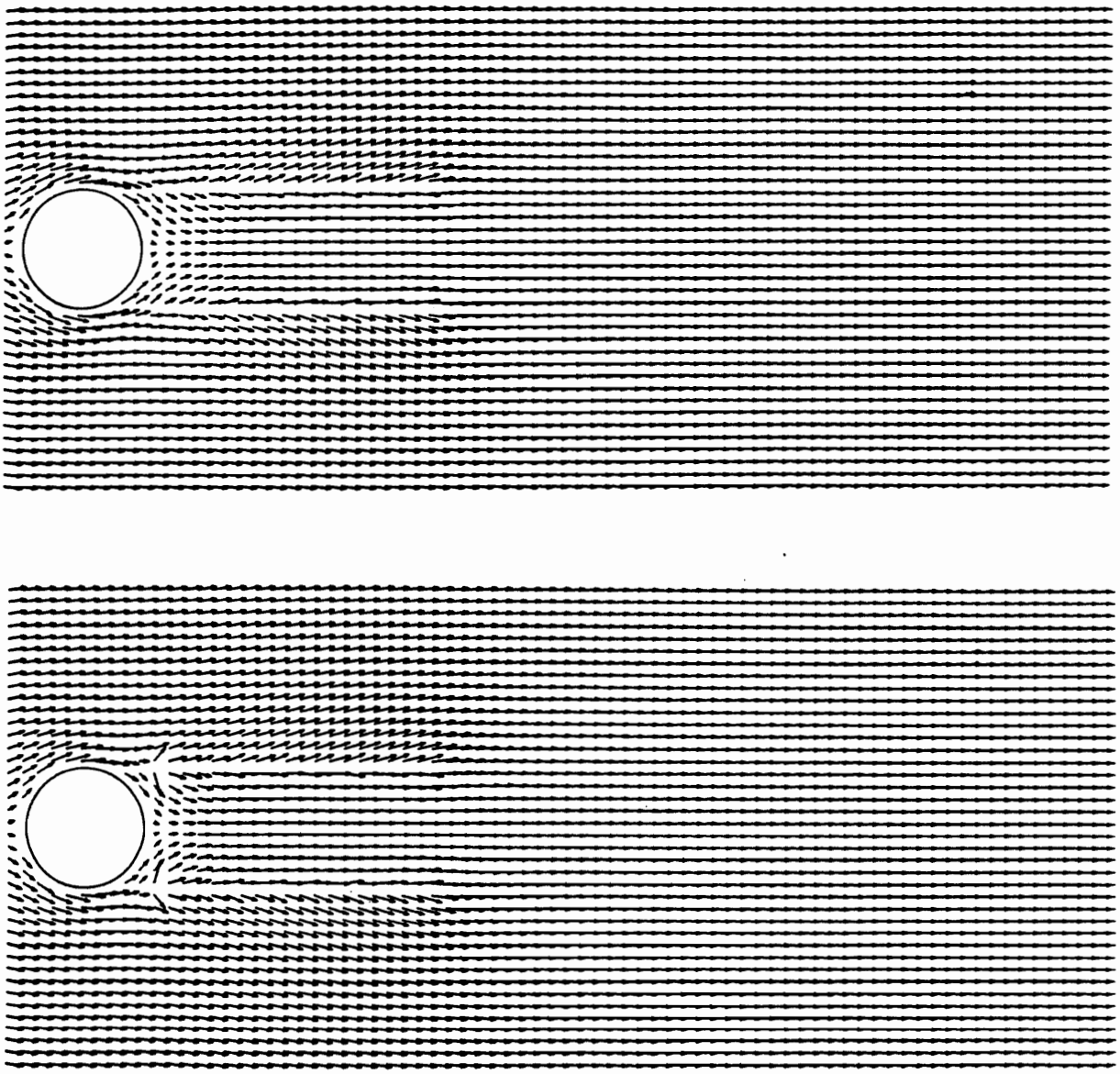

Figure 63. Two source lines exhibiting the effects of volume expansion: The volume expansion of source lines in the top figure is equal to the volume expansion of flame sheets. The strength of source lines in the bottom figure is five times as strong as that in the top figure.

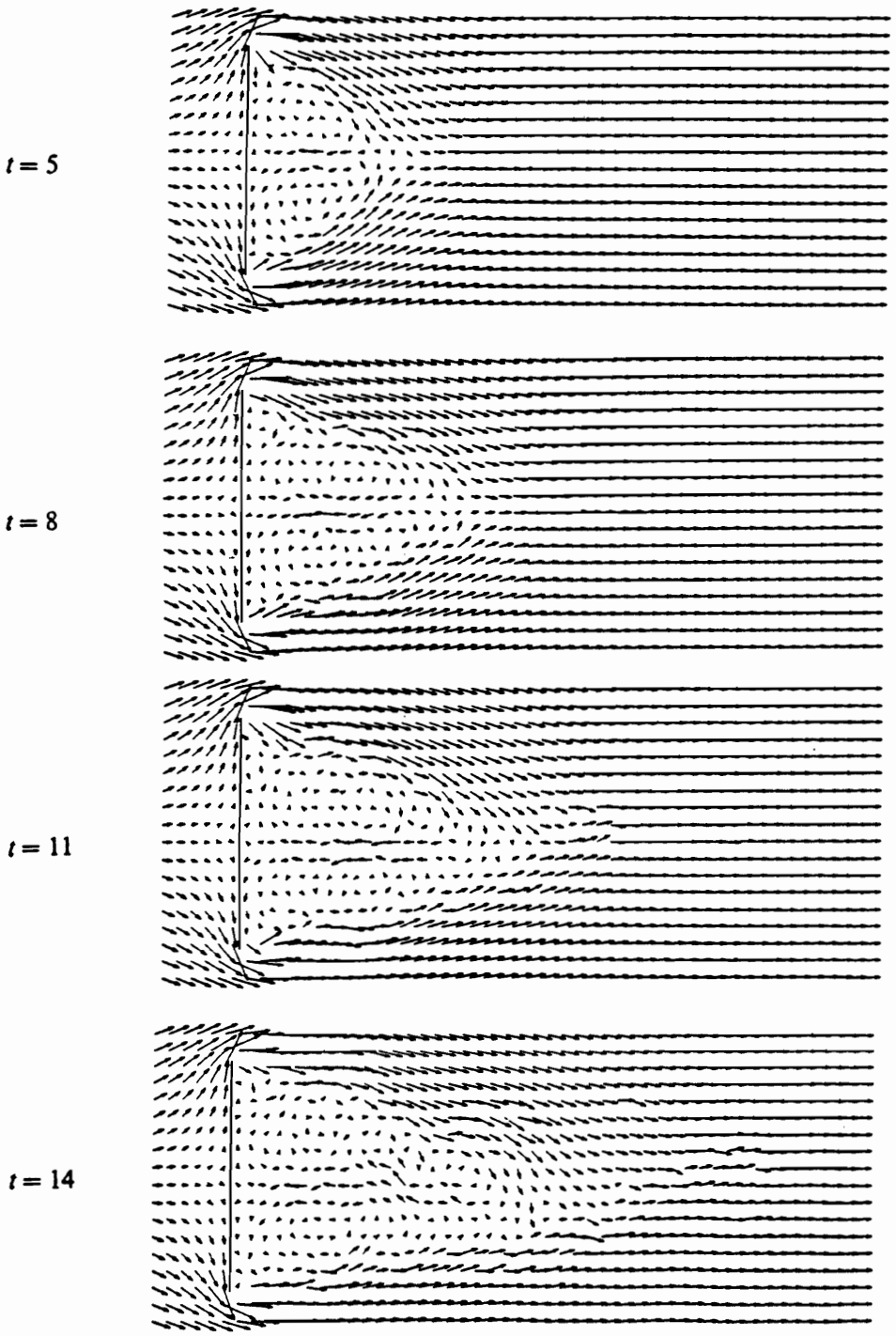

Figure 64. Flow past a flat plate normal to freestream, Re = 2000: Velocity vectors at fixed sampling points.

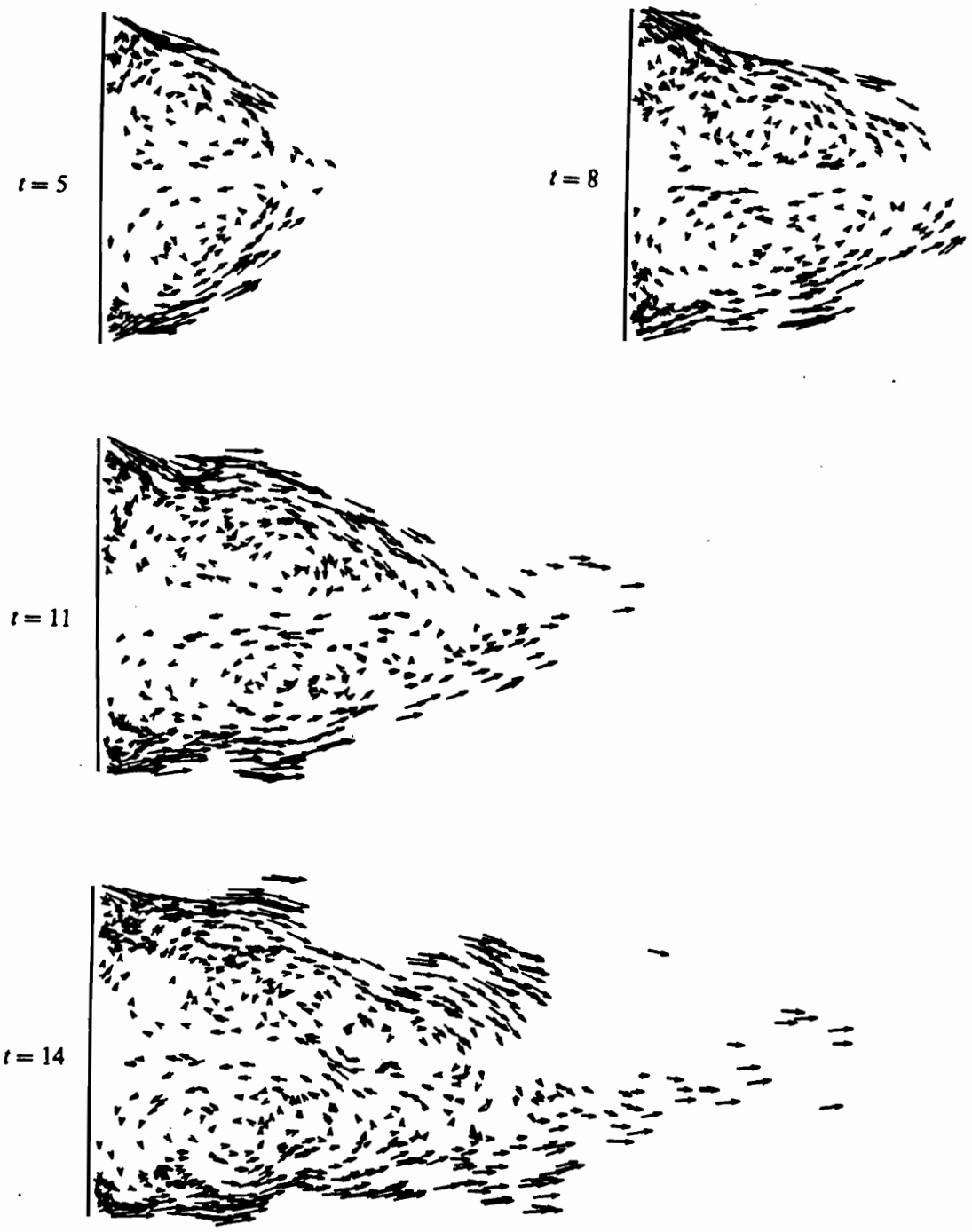

Figure 65. Flow past a flat plate normal to freestream, Re = 2000: Velocity vectors at locations where individual vortices are.

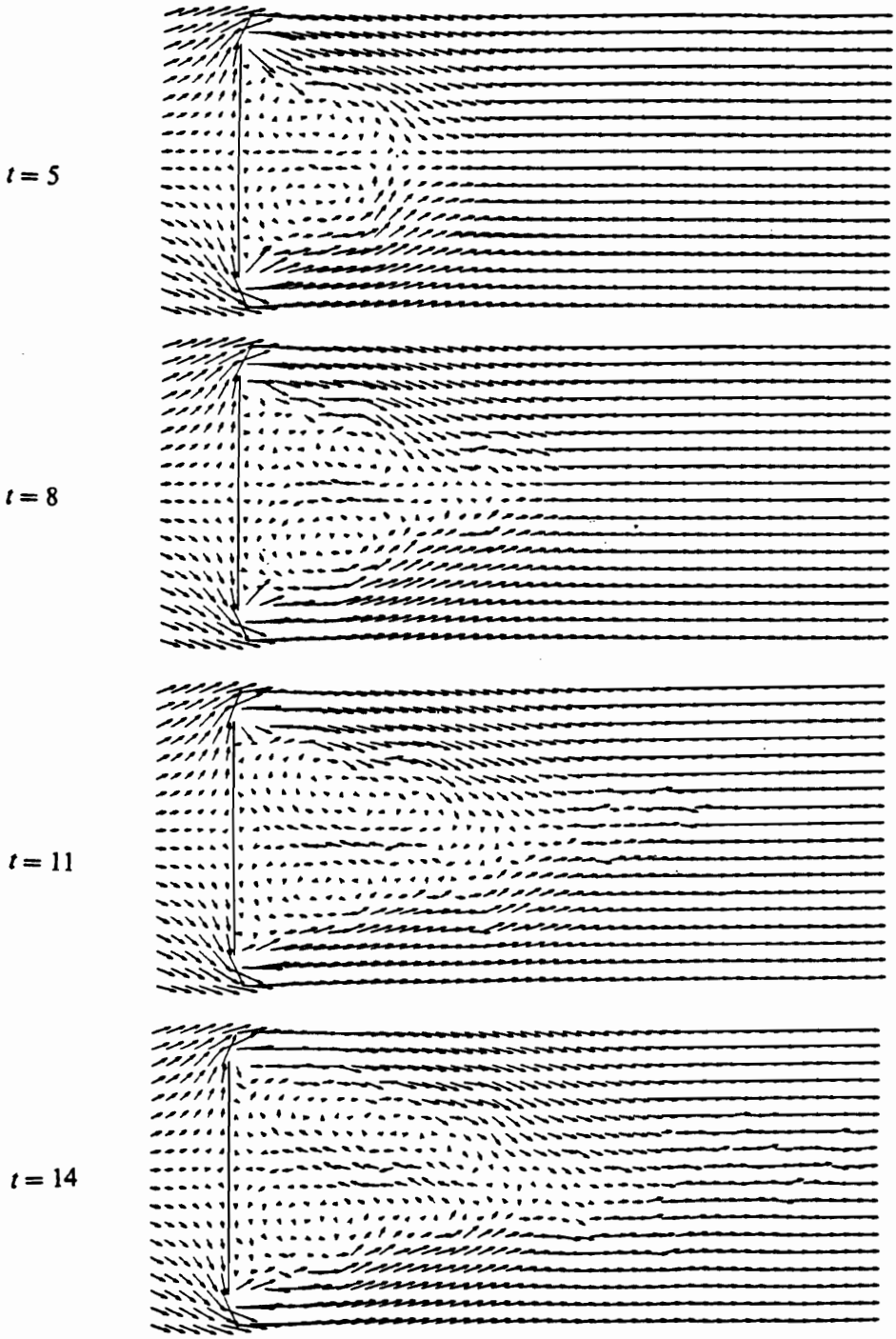

Figure 66. Flow past a flat plate normal to freestream, Re = 10000: Velocity vectors at fixed sampling points.

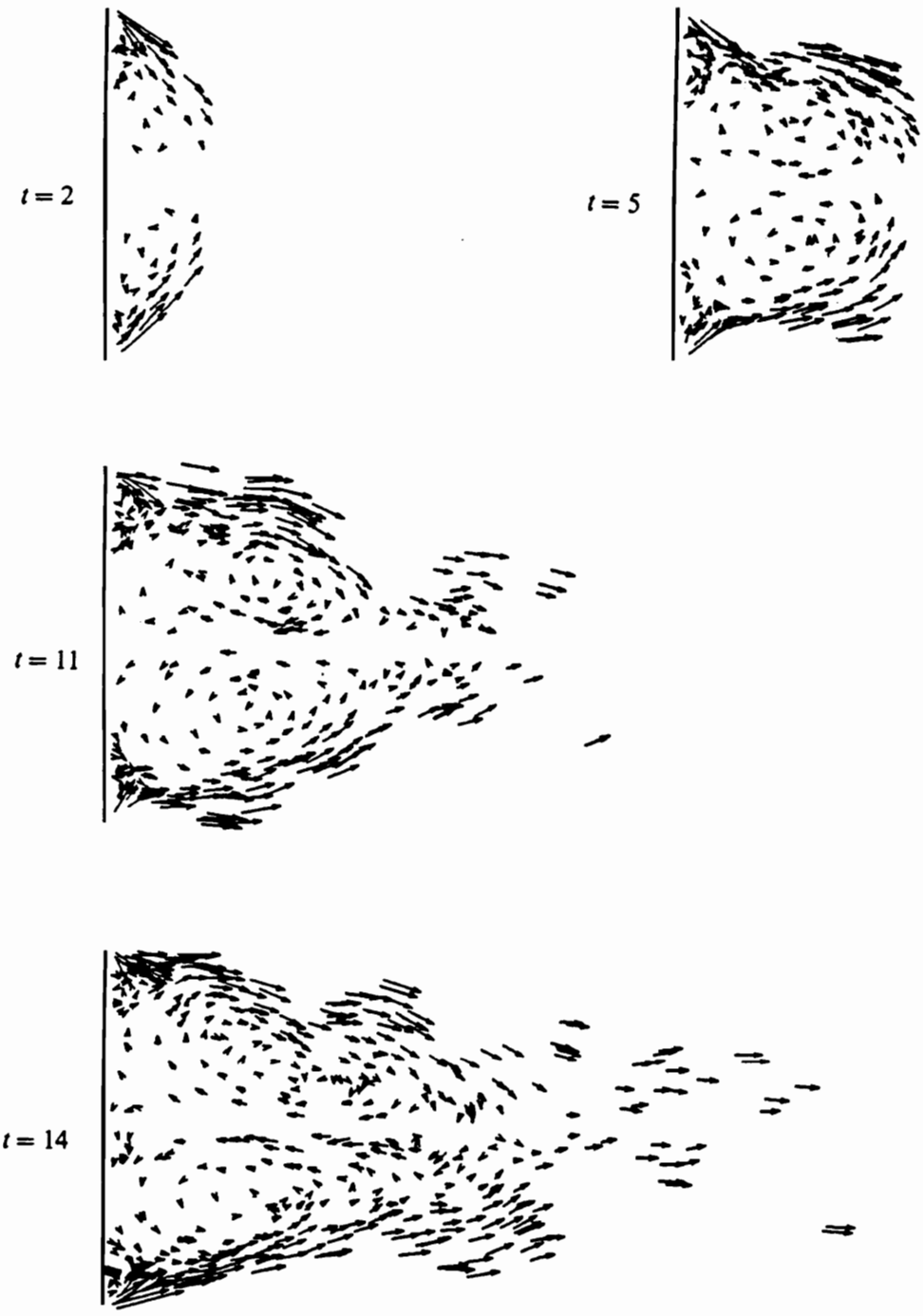

Figure 67. Flow past a flat plate normal to freestream, Re = 10000: Velocity vectors at locations where individual vortices are.

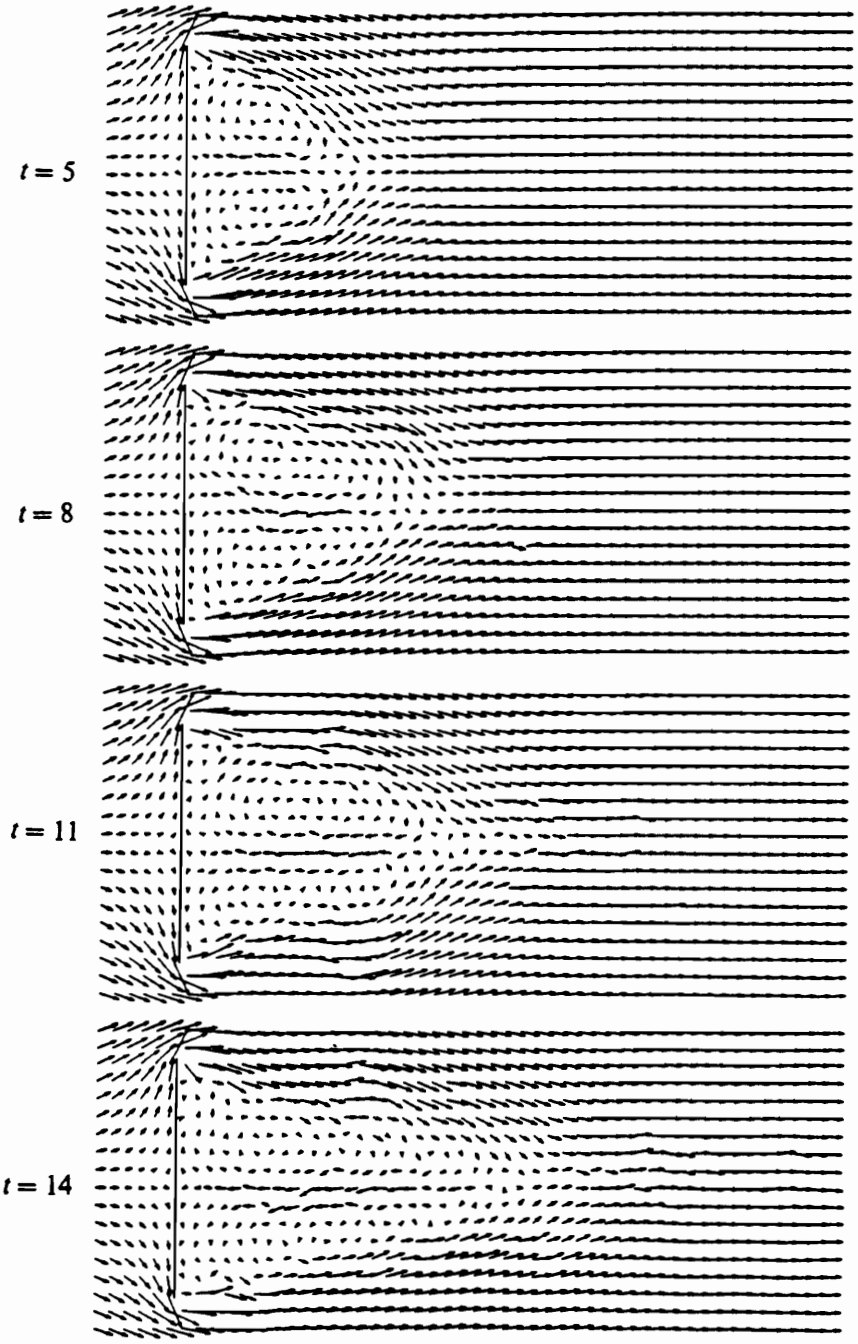

Figure 68. Flow past a flat plate normal to freestream, Re = 50000: Velocity vectors at fixed sampling points.

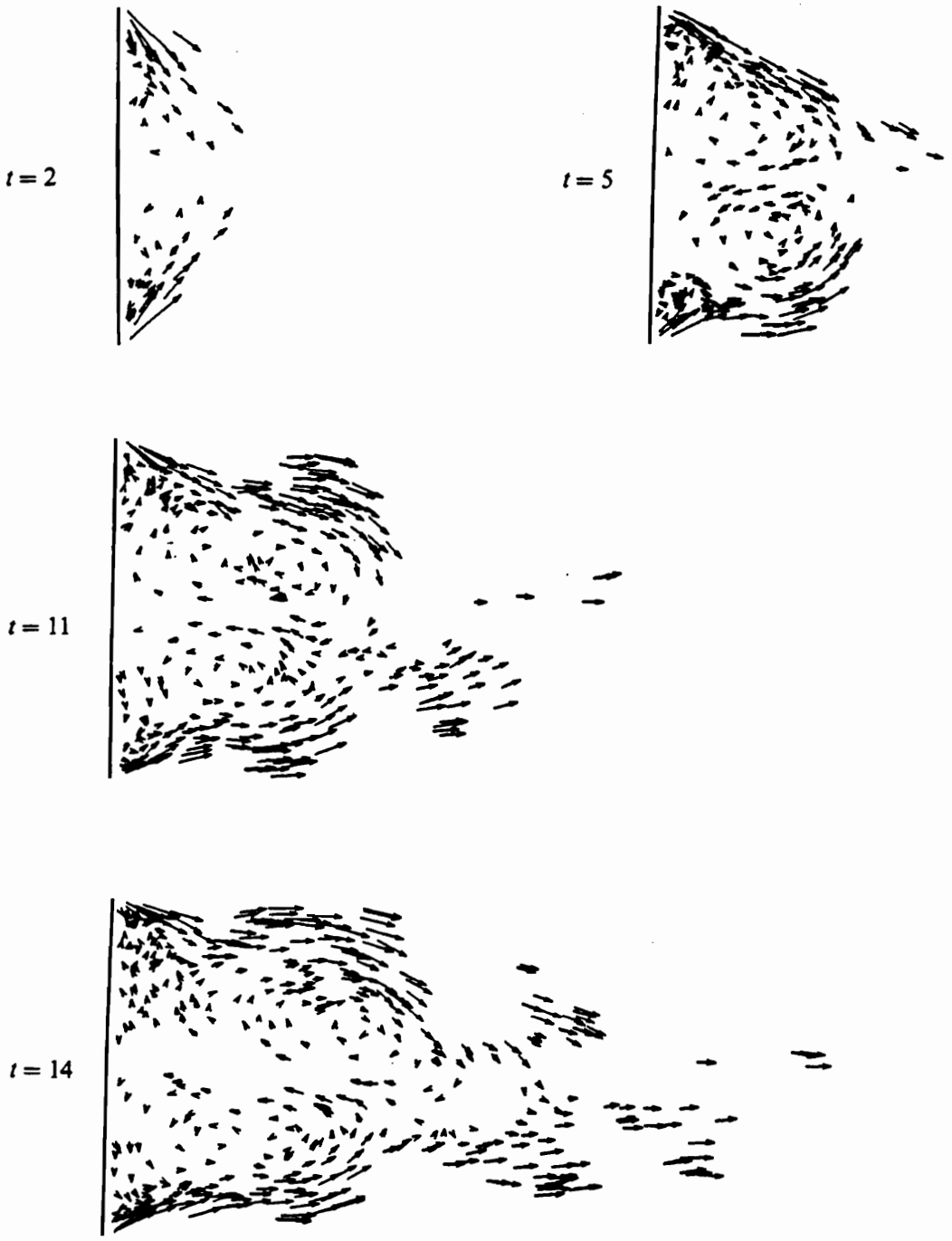

Figure 69. Flow past a flat plate normal to freestream, Re = 50000: Velocity vectors at locations where individual vortices are.

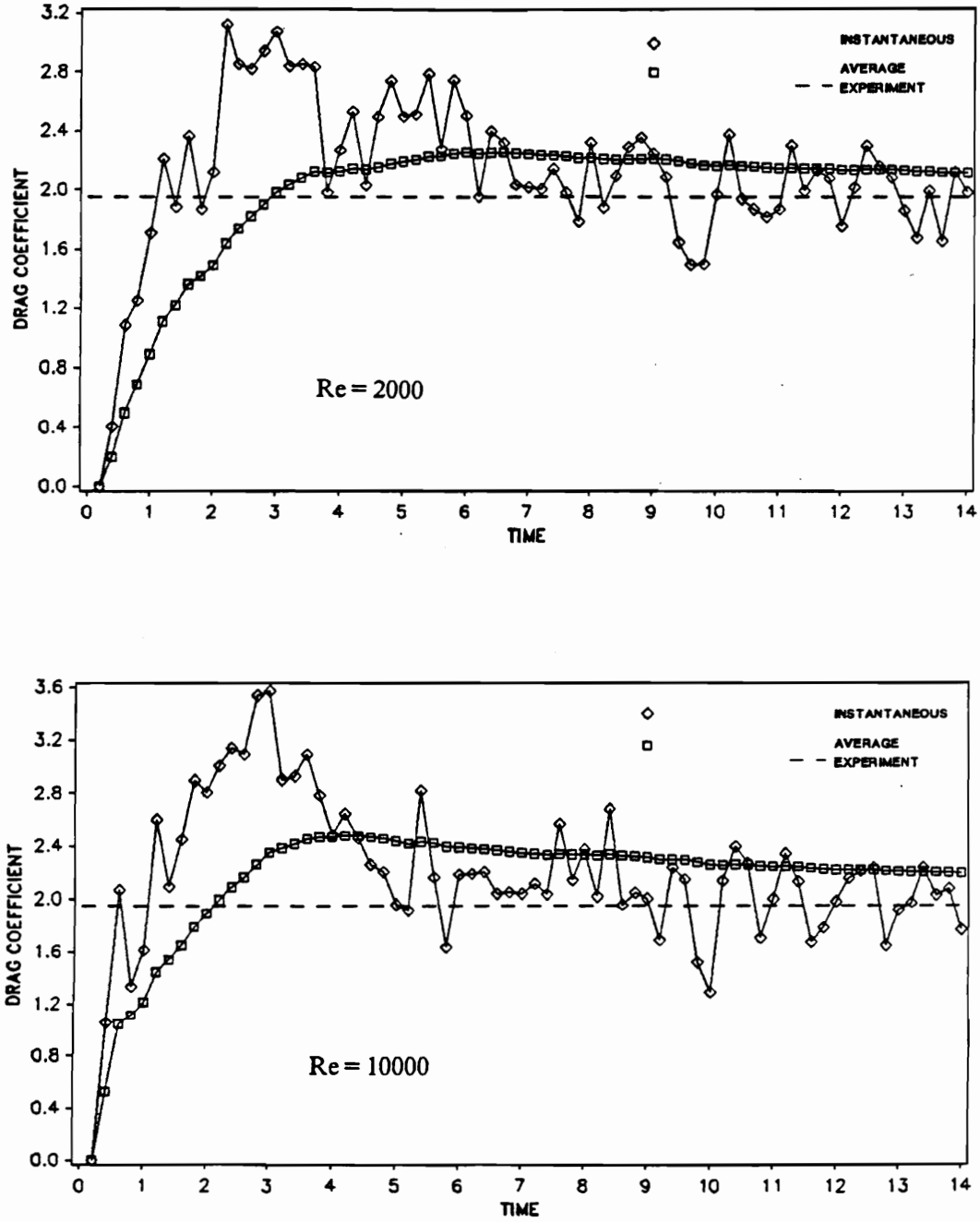

Figure 70a. Computed drag coefficients of a flat plate normal to freestream.: Top figure is for $Re = 2000$, computed C_D is 1.99. Bottom figure is for $Re = 10000$, computed C_D is 2.06.

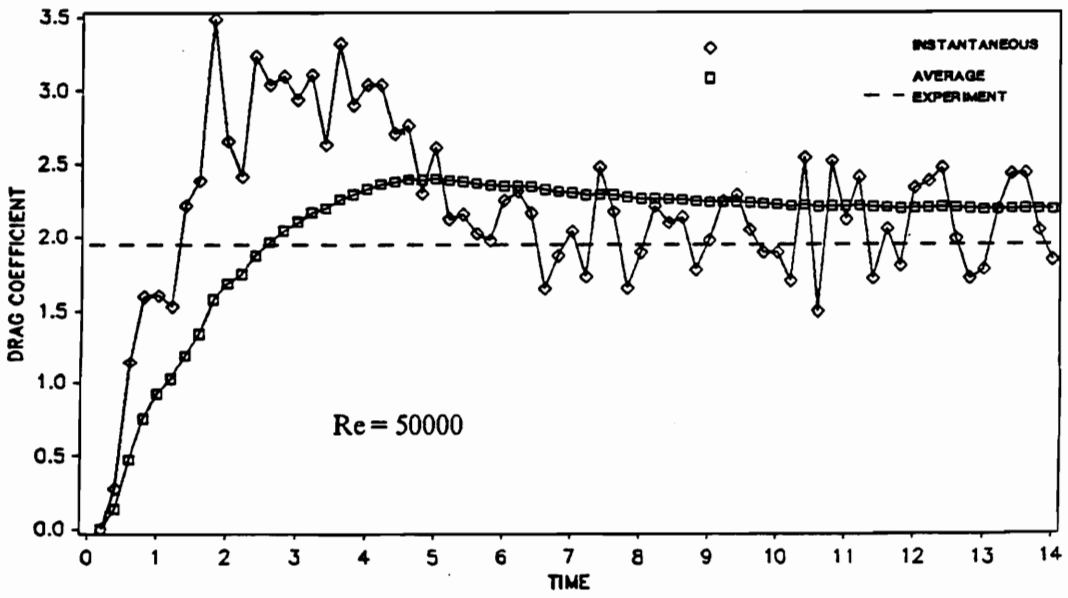

Figure 70b. **Computed drag coefficients of a flat plate normal to freestream.:** $Re = 50000$. Computed C_D is 2.05.

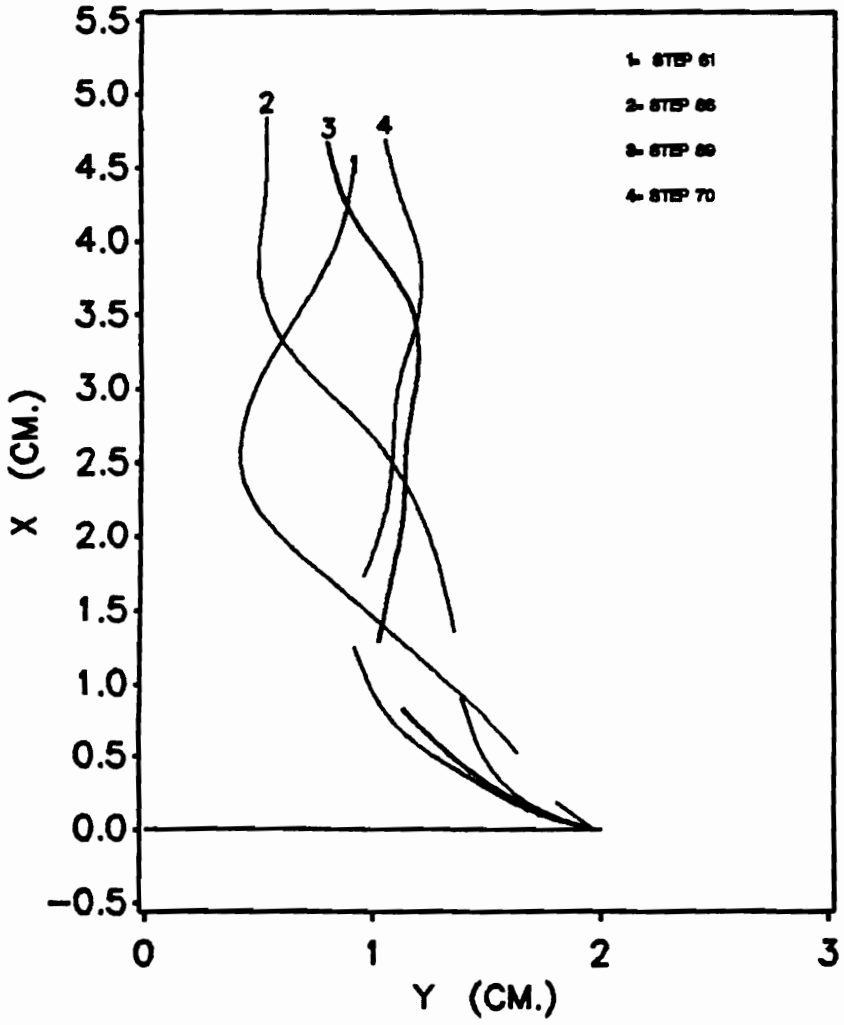

Figure 71. Broken and wrinkled flame sheets near a flat plate

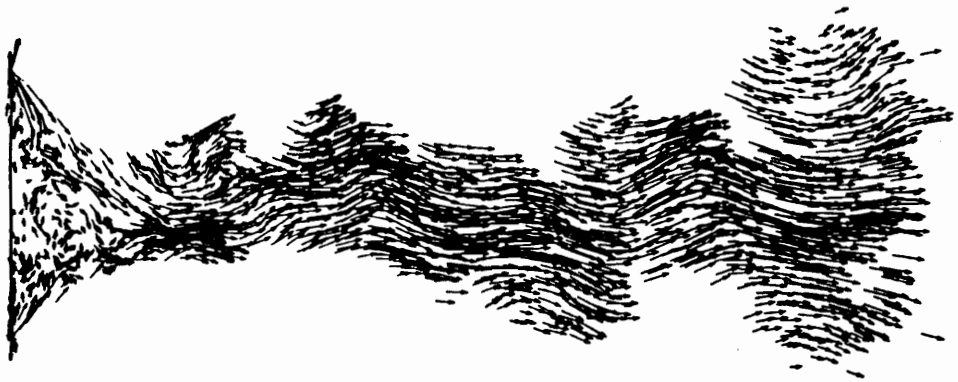

Figure 72. Reacting flow near a flat plate 4 cm high, Re = 12000, step = 50: Modified source model with flame and plate-shed vorticity.

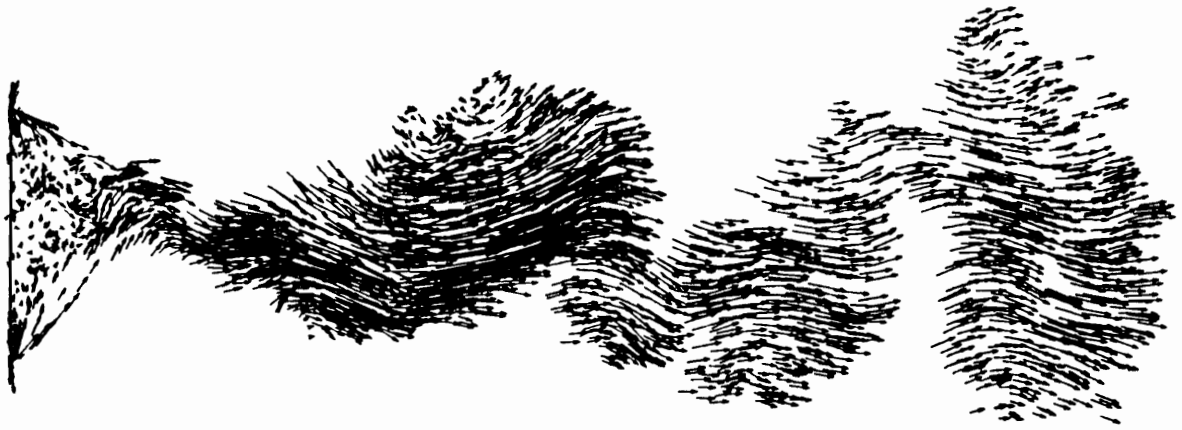

Figure 73. Reacting flow near a flat plate 4 cm high, Re = 12000, step = 60: Modified source model with flame and plate-shed vorticity.

Figure 74. Reacting flow near a flat plate 4 cm high, Re = 12000, step = 70: Modified source model with flame and plate-shed vorticity.

Appendix A. Flow Past a Circular Cylinder

The following presentation is based on a series of work done by Chorin (1973) and Cheer (1983). However, some modification is necessary when applied to the flame-flow interaction problem. The modification will be mentioned at the end of this appendix.

To apply the vortex sheet method to the flow past a circular cylinder, let us take (x, y) as (θ, r) of polar coordinates and (u, v) as (u_θ, u_r). The development of numerical code is tedious but straightforward, however, much care must be exercised in the transformations of coordinate and velocity between the rectangular system (Fig. 3) describing the overall flow and the polar system describing flow near the surface of the cylinder.

The following steps explain how vortex sheets near the solid boundary are generated.

1. Divide the circle into M equal segments, the length of each segment is $h = 2\pi/M$.

2. Choose the numerical shear thickness δ_s to be $O(Re_c^{-1/2})$, where Re_c is the Reynolds number based on the diameter of the cylinder. Add δ_s to the radius of the cylinder and form a larger concentric circle. Then divide this larger circle also into M segments and locate all the mid- points M' of these segments.

3. Calculate the local tangential velocity u_δ at M' using eqs.(2.56). The quantity u_δ is usually not zero and called the slip velocity. To reduce slip velocity to zero on the surface, a number of vortex sheets are generated at M'. Each of these vortex sheets provides with a velocity jump $\Delta u \leq -\xi_{max}$ where ξ_{max} is a given upper limit to the strength of a vortex sheet. Besides being bounded by an upper limit, Δu is also adjusted so that $\frac{-2u_\delta}{\Delta u}$ gives an even number, NS, of vortex sheets.

After their creation, all vortex sheets must move about in the flow. When considering the movement of vortex sheets near the cylinder, local Cartesian system was used to simplify the formulation (Cheer 1983). The errors incurred are $O(10^{-3})$ when normalized with respect to the radius of the cylinder. However, the code we developed has been modified to treat curvature effect to obtain better accuracy at negligible increase in computation cost. In the first presentation of vortex sheet method, Chorin(1978) created an even number of vortex sheets at

every M'. Ghoniem et al. (1982) relaxed this restriction. The above difference is without consequence. The original version created $NS = 2u_\delta/\Delta u$ sheets and let half of these sheets go into the wall during the first time step after creation and those which go into the wall do not participate in any further calculation. Ghoniem et al. created only $NS = u_\delta/\Delta u$ sheets , but they retained all new sheets for the first time step. Therefore the effective number of sheets are the same for the two choices of number of sheets generated at M′.

To move the vortex sheets during a time step, the following rules are observed.

1. All existing vortex sheets except the newly-created ones follow the two branch solution process : first, a convective displacement; then, a random walk in the y direction only. A first-order method is used for the convective part with velocity components given by eqs. (2.56) and (2.59). The random walk is sampled from a Gaussian distribution with zero mean and $(2\Delta t_c/Re_c)^{-1/2}$ standard deviation. Therefore,

$$
\begin{aligned}
{}_{n+1}x_i &= {}_nx_i + {}_nu_i\Delta t_c \\
{}_{n+1}y_i &= {}_ny_i + {}_n\upsilon_i\Delta t_c
\end{aligned}
\qquad (A.1)
$$

   where ${}_nu_i$ is given by (2.56), and ${}_n\upsilon_i$ by (2.59).

2. Since all newly-generated sheets are on the surface of a solid wall, they should have zero convective velocity and their motion comprises only the random

walk in the y direction. If $NS = 2u_\delta/\Delta u$ is chosen, then a scheme must be devised to sample alternately positive and negative random walks so that exactly half of the newly-generated sheets go into the wall. Otherwise, the new vortex sheets are only allowed random walks in the positive y direction.

After the displacement of each vortex sheet is found, one checks to see if any sheet goes outside the numerical layer (Fig. 11c). When this happens, that sheet should be converted into a vortex disk and referred to as a cylinder vortex. The conversion is simple, a sheet (x_i, y_i, ξ_i, h) becomes a disk $(x_i, y_i, \Gamma_i, \sigma_i)$ with $\Gamma_i = \xi_i h$ and $\sigma_i = h/\pi$. Γ_i and σ_i are the circulation and radius of the vortex disk, respectively. When an 'old' vortex sheet goes into the solid wall, this sheet should be reflected off the wall. This 'old' sheet remains a sheet if its final position is within the numerical shear layer (Fig. 11c), otherwise it turns into a disk. In order to simulate separation, a sheet is turned into a disk when its velocity vector deviates appreciably from the local tangent. The criterion found by numerical trials is about 30° for the present problem. Finally, any sheet which has negative tangential velocity, a sign of reverse flow, should also be turned into a vortex disk. The motion of cylinder vortices is solved, again, by the two-branch solution of random vortex method. A second-order Runge-Kutta method is used instead of the first-order method used by Cheer (1983) to solve the convective motion of vortex disks because vortex disks tend to cluster together when simulated by the random vortex method and the better resolution of a second-order method is needed. Due to their proximity to the cylinder, some cylinder vortices may re-

enter the numerical layer. The following rules are used to treat re-entry of vortex disks into the numerical layer (Fig.11c).

1. If a vortex disk has its final position, after convection and random walk, inside the layer, it is turned into a vortex sheet.

2. If a vortex disk goes into the wall deeper than δ_s, it is lost.

3. If a vortex disk goes no deeper than δ_s into the wall, it is reflected. This vortex disk remains a disk if it lands beyond the numerical layer after reflection, and turns into a sheet if it lands inside the layer.

All vortex disks (x_i, y_i) near the cylinder should be moved according to eq. (2.48) under the influence from all other vortex disks at (x_j, y_j) with the changes that U_x and U_y are given by

$$U_x = U_\infty\left(1 - \frac{R^2(x_i^2 - y_i^2)}{(x_i^2 + y_i^2)^2}\right) + \frac{1}{2\pi}\sum \Gamma_j\left[\frac{y_j - y_i}{(\max(\sigma_j, r_{ij}))r_{ij}} - \frac{y'_j - y_i}{(\max(\sigma_j, r'_{ij}))r'_{ij}}\right],$$

$$U_y = -U_\infty\left(\frac{2x_i y_i R^2}{(x_i^2 + y_i^2)^2}\right) + \frac{1}{2\pi}\sum \Gamma_j\left[\frac{x_j - x_i}{(\max(\sigma_j, r_{ij}))r_{ij}} - \frac{x'_j - x_i}{(\max(\sigma_j, r'_{ij}))r'_{ij}}\right]. \quad (A.2)$$

When the above described algorithm is applied to simulate the vorticity production on the surface of a cylinder used as a flame holder, there is the possibility that the flame-generated vortices may enter the numerical shear layer as well as

the cylinder-generated vortices. Upon entering the numerical shear layer, a flame-generated vortex is converted into an odd number of equal-strength vortex sheets under the constraint that the strength of each vortex sheet do not exceed the maximum strength set for the cylinder-generated vortex sheets and the length of the converted sheets is h (i.e., the same length as the cylinder-generated vortex sheets.) Suppose that a flame vortex is converted into three vortex sheets, then the no. 2 sheet is located at the point where the flame vortex ends up within the numerical layer. The no. 1 and the no. 3 sheets are positioned at the opposite ends of the no. 2 sheet, in other words, like three cars parked bumper to bumper. The subsequent motion of sheets converted from flame vortices is treated in the same way as cylinder-generated vortex sheets. When flame-vortex-converted vortex sheets leave the numerical shear layer, they are turned into vortex disks. According to the above scheme, a flame vortex which enters the numerical shear layer may later re-emerge as several smaller and weaker vortex disks. This is accepted on the ground that in the physical world a vortex can not retain its integrity after impinging a solid surface.

Appendix B. Calculation of the Drag Coefficient

The lift and the drag coefficients can be calculated with the following equation

$$L - iD = \rho \frac{\partial}{\partial t} \sum_{1}^{N} \Gamma_j (z_j - \frac{1}{z'_j}) \ , \qquad (B.1)$$

where L is the lift, D is the drag, ρ is the density of fluid, Γ_j is the strength of a vortex located at $z_j(x_j, y_j)$, and z'_j is the complex conjugate of z_j. The derivation of the above formula can be found in Graham (1980). The drag coefficient is then given by

$$C_D = \frac{2D}{\rho U^2_{\infty} A} \ ,$$

where A is the cross-sectional area normal to U_{∞} per unit depth for a 2-D body. In the case of a circular cylinder, A is numerically equal to the diameter of the cylinder and one can write

$$C_D = -\frac{\partial}{\partial t}\sum_{1}^{N}\Gamma_j\left(y_j - \frac{y_j}{x^2_j + y^2_j}\right) .$$

Eq(B.1) applies only to regions where the complex potential is analytic. Therefore a contour near the cylinder must be chosen and only vortex disks located outside the contour are included in the calculation of C_D. In this work the contour is chosen to be 0.1 times the radius of the cylinder.

Vita

Shiung-po Kao was born on January 11, 1952 in Kao Shiung, Taiwan. In June 1977, he graduated at the Catholic Fu-Jen University, Taipei, with a Bachelor of Science degree in Physics. He joined the graduate program at Virginia Polytechnic Institute and State University in Fall 1982 and received a Master of Science degree in Aerospace Engineering in Fall 1984.